

A new crustal fault formed the modern Corinth Rift

David Fernández-Blanco, Gino de Gelder, Robin Lacassin and Rolando Armijo

Tectonique et Mécanique de la Lithosphère, Institut de Physique du Globe de Paris, Sorbonne Paris Cité, Univ Paris
Diderot, CNRS, F-75005 (1 rue Jussieu)

[Abstract](#)

[1 Introduction](#)

- [1.1 How is the rift framed in its large-scale tectonic and geodynamic context?](#)
- [1.2 Did the rift develop continuously or after a disruptive tectonic event?](#)
- [1.3 Is the rift main flank controlled by a low-angle or high-angle fault?](#)
- [1.4 What mechanical model best describes the rift?](#)
- [1.5 Why are geodetic extension rates at odds with long-term extension rates?](#)
- [1.6 Why is the rift markedly asymmetric in its centre and symmetric at rift ends?](#)
- [1.7 Is the bounding fault system propagating along strike?](#)
- [1.8 Is the bounding fault system a series of individual faults or a composite fault?](#)
- [1.9 Key geologic elements in the modern rift and approach](#)

[2. Geologic elements to understand normal fault mechanics](#)

- [2.1 Normal fault mechanics](#)
- [2.2 Geologic elements used as fault mechanics proxies](#)
 - [2.2.1 Stacked swath profiles “2.5-D” topography](#)
 - [2.2.2 Footwall relief](#)
 - [2.2.3 Longitudinal river profiles and tectonic knickpoints](#)
 - [2.2.4 Marine terraces and Gilbert-type deltas](#)
- [2.3 Approach for fault growth reconstruction in time](#)

[3 The modern Corinth Rift and its main geologic elements](#)

- [3.1 Active normal faults](#)
 - [3.1.1 Attitude, rates and ages along the bounding fault system](#)
 - [3.1.2 Other active normal faults](#)
- [3.2 Uplifted Quaternary marine terraces](#)
- [3.3 Modern and \(perched\) Plio-Pleistocene Gilbert Deltas](#)
- [3.4 Plio-Pleistocene \(uplifted\) basin extent](#)
- [3.5 Hanging wall synrift deposits](#)

[4 Bounding fault topobathymetry, river catchments and footwall relief](#)

- [4.1 Topobathymetry](#)
 - [4.1.1 Across the bounding fault](#)
 - [4.1.2 Along the bounding fault](#)
- [4.2 Footwall river profiles and tectonic knickpoints](#)
- [4.3 Footwall relief](#)
 - [4.3.1 West rift](#)
 - [4.3.2 Rift southern shoulder](#)

[5 Fault growth and relief response in the rift southern shoulder](#)

- [5.1 Growth and propagation sequence](#)
 - [5.1.1 West rift](#)
 - [5.1.2 Rift southern shoulder](#)
- [5.2 Vertical motions in time](#)

[6 Discussion: Opening of the modern Corinth Rift in the Aegean domain](#)

- [6.1 Recap: Landscape response to a new rift forming fault](#)
- [6.2 Mechanical models of the modern Corinth Rift and its lithosphere](#)
- [6.3 Two-phase opening of the Corinth Rift](#)
 - [6.3.1 Antecedent distributed extension](#)
 - [6.3.2 Change in extension mechanics](#)
 - [6.3.3 The advent of the modern Corinth Rift](#)
 - [6.3.4 The modern Corinth Rift at present](#)
- [6.4 Two-phase evolution of the Anatolian-Aegean plate](#)

[7 Conclusions](#)

[Acknowledgements](#)

[References](#)

[Supplementary material](#)

[Supplementary material References](#)

A new crustal fault formed the modern Corinth Rift

David Fernández-Blanco, Gino de Gelder, Robin Lacassin and Rolando Armijo

Tectonique et Mécanique de la Lithosphère, Institut de Physique du Globe de Paris, Sorbonne Paris Cité, Univ Paris
Diderot, CNRS, F-75005 (1 rue Jussieu)

Abstract

The modern Corinth Rift is one of the fastest extending regions worldwide and has the highest seismicity in Europe. Most of this strain and seismicity occur in relation with the normal fault system that bounds this continental rift to the south. The rift-bounding fault dips north and accommodates nearly pure N-S extension that results in lithospheric elastic flexure of fault flanks and the marked asymmetry of the modern rift. The exceptional geological and geomorphological archives recording flexure and uplift along the footwall of the rift-bounding fault can be used to derive the time sequence of fault growth at rift margin scale. The growth history and associated uplift patterns of the rift-bounding fault relate in turn to the along and across strike geometry and growth mechanics of the modern Corinth Rift.

Here we derive the growth mechanics of the modern Corinth Rift from an integrative effort at the scale of the entire rift, and the reconstruction of the growth and fast footwall uplift of the rift-bounding fault system, from onset to present. We analysed the topo-bathymetry, relief, geomorphologic markers and river catchments along and across the uplifting rift flank in the light of normal fault mechanics. We evaluate the extent and geometry of the elastic flexure associated with footwall uplift, and derive fault displacement profiles in time using coeval markers of past sea level and present-day footwall relief. We also infer the history of fault linkage assessing footwall relief and tectonic knickpoints of main trunks that drain the footwall orthogonally towards the hanging-wall.

Our neotectonic investigation at rift scale shows that the surficial en-échelon fault segments are kinematically coherent at depth, constituting a fault >80 km in length. This composite master fault grew along-strike from the rift centre linking and integrating individual fault segments that developed co-linearly at younger times, especially at westward locations, like the Aigio Fault Array. Our data further suggest that the recent tectonic activity on such master fault controls the first-order geology and morphology of the modern Corinth Rift. Based on the observed fault elastic flexure, footwall relief wavelength and the high uplift and slip rates, we infer that the rift-bounding fault is steep and affects the entire crust, growing in a strong long-term elastic lithosphere much like a propagating crack. We put forward a two-phase growth model for the Corinth Rift where fast disruptive growth (in ~300 kyr) of the new, highly-localized rift-forming fault opens the modern rift as it propagates along its strike (since <700 ka) superimposed onto the preceding distributed extension (in the previous ~4 My). The strain-localized growth and propagation of this new master fault enlarged the modern rift through time as a highly asymmetric half-graben, along and across strike, and leads the development of the modern Corinth Rift as we know it today. Our model can be framed quite simply in the context of the Aegean-Anatolian plate evolution. Early distributed extension occurred in relation with the growth of the NW tip of an extensional trough led by slab rollback, and the new overwriting fault grew in the frame of the damage-zone stress fields led by the westward propagating tip of the North Anatolian Fault.

1 Introduction

The young, amagmatic and asymmetric continental rift of Corinth is one of the fastest extending regions accessible on land worldwide and one of the most seismically active (e.g., Dan McKenzie, 1978; Collier and Dart, 1991; Papazachos et al., 1992; Armijo et al., 1996; Avallone et al., 2004; Bernard et al., 2006; Leeder et al., 2008; Jolivet et al., 2010; Charalampakis et al., 2014). These features make the Corinth Rift one of the best natural laboratories to study early intracontinental extension and one of the most explored sites in the Earth Sciences. Research in the rift probably started in the fifth century BC, with the philosophical arguments on mythological attributions to karstic features in the mountains south of the Corinth Gulf (Herodotus “History”; e.g., Clendenon, 2009), and continue today, with the preliminary results of the IODP Expedition 381 in the gulf itself (McNeill et al., 2018). Despite such an impressive volume of research, first-order controversies still remain with regards to the rift mechanical and tectono-stratigraphic evolution.

Some of these first-order controversies can be formulated as the following questions: (1) is the rift-bounding fault system segmented in individual ~10-25 km long en-échelon normal faults that outcrop at surface (Gawthorpe et al., 2017b), or are these normal faults linked kinematically as a composite master fault at the scale of the rift (Armijo et al., 1996)?; (2) is the bounding fault system propagating along strike (e.g., Ford et al., 2016)?; (3) why is the rift markedly asymmetric at its center (De Gelder et al., 2018) and symmetric towards rift ends (e.g., McNeill and Collier, 2004)?; (4) why are geodetic extension rates (e.g., Avallone et al., 2004) at odds with finite strain and long-term extension rates (e.g., Bell et al., 2011)?; (5) what mechanical model describes the rift more accurately (Armijo et al., 1996; Rigo et al., 1996; Sorel, 2000; Ford et al., 2016; Gawthorpe et al., 2017b; Fernández-Blanco et al., 2019a)?; (6) is the rift main flank controlled by a low-angle (<30°) detachment fault (e.g., Rigo et al., 1996; Sorel, 2000; Jolivet et al., 2010) or a high-angle (>40°) planar fault (e.g., Armijo et al., 1996; Bell et al., 2017; De Gelder et al., 2018)?; (7) did the rift

develop continuously since 4-5 Ma (e.g., Ford et al., 2016; Gawthorpe et al., 2017b) or largely after a disruptive tectonic event <1 Ma (e.g., Armijo et al., 1996; Fernández-Blanco et al., 2019a)?; (8) how is the rift framed in its large scale tectonic and geodynamic context (cf. Armijo et al., 1996; Jolivet et al., 2010)? We briefly review key facts and previous research proposals addressing these questions, in reverse order, and compile, analyze and discuss relevant geologic and geomorphologic data to provide constraints and insights into the aforementioned controversies.

1.1 How is the rift framed in its large-scale tectonic and geodynamic context?

Since ~30-45 Ma, the progressive rollback of the downgoing African slab and correlative southward trench migration initiated widespread extension in most NW Greece, in the Cyclades and W Turkey (e.g., Le Pichon and Angelier, 1981; Reilinger et al., 2009; Brun and Sokoutis, 2010; Jolivet and Brun, 2010; Jolivet et al., 2013; Brun et al., 2016). In N Greece, however, the aforementioned back-arc extension is overwritten by younger, presently active, steep normal faults, formed in relation to a transtensive stresses caused by the westward propagation of the North Anatolian Fault (NAF) into the North Aegean Through (NAT) (e.g., Armijo et al., 1999; Koukouvelas and Aydin, 2002) (Fig. 1). Age of stress change is unclear but can be broadly bracketed between 430 ka in the southwestmost NAT (Saporades Basin; Ferentinos et al., 2018) and ~4 Ma at the NAT front (Olympos-Ossa-Pelion Range; Lacassin et al., 2007).

The intracontinental rift of Corinth is located near the Hellenic subduction, and in-between the aforementioned Aegean back-arc extensional throughs and NAF-related transtensional systems (Fig. 1). The Corinth Rift lays (i) between ~150 and ~250 km NE of the Hellenic subduction trench; (ii) to the NW of the western termination of one of the south-arched extensional throughs of the Aegean back-arc system (e.g., Jolivet et al., 2010, 2013; Brun et al., 2016); and, (iii) to the SW of a set of NW-SE-trending extensional systems formed by transtension in relation with the NAF (Armijo et al., 1996; Koukouvelas and Aydin, 2002; Lacassin et al., 2007; Kiliyas et al., 2013). The main models

of rift development suggest a causal relationship, not apparent in the upper crust, between these tectonic and geodynamic elements and the modern Corinth Rift. These models relate the Corinth Rift with: (i) flat-slab subduction and retreat of the Hellenic slab (Leeder et al., 2003) or variably buoyant subducting lithosphere (Royden and Papanikolaou, 2011), (ii) a crustal-scale detachment of the Aegean back-arc (Jolivet et al., 2010) and (iii) the damage zone of the NAF propagating tip (Armijo et al., 1996). The distinction between potential tectonic and geodynamic drivers is partially hindered by the absence of a generalized model of rift mechanics. Here, we discuss the potential tectonic and geodynamic causes behind the formation of the modern Corinth Rift after deriving its growth mechanics by means of (i) an integration of new and available geologic and geomorphologic evidence at the rift scale, and (ii) a detailed morphotectonic analysis to reconstruct the growth of the modern fault system bounding the modern rift to the south since its onset.

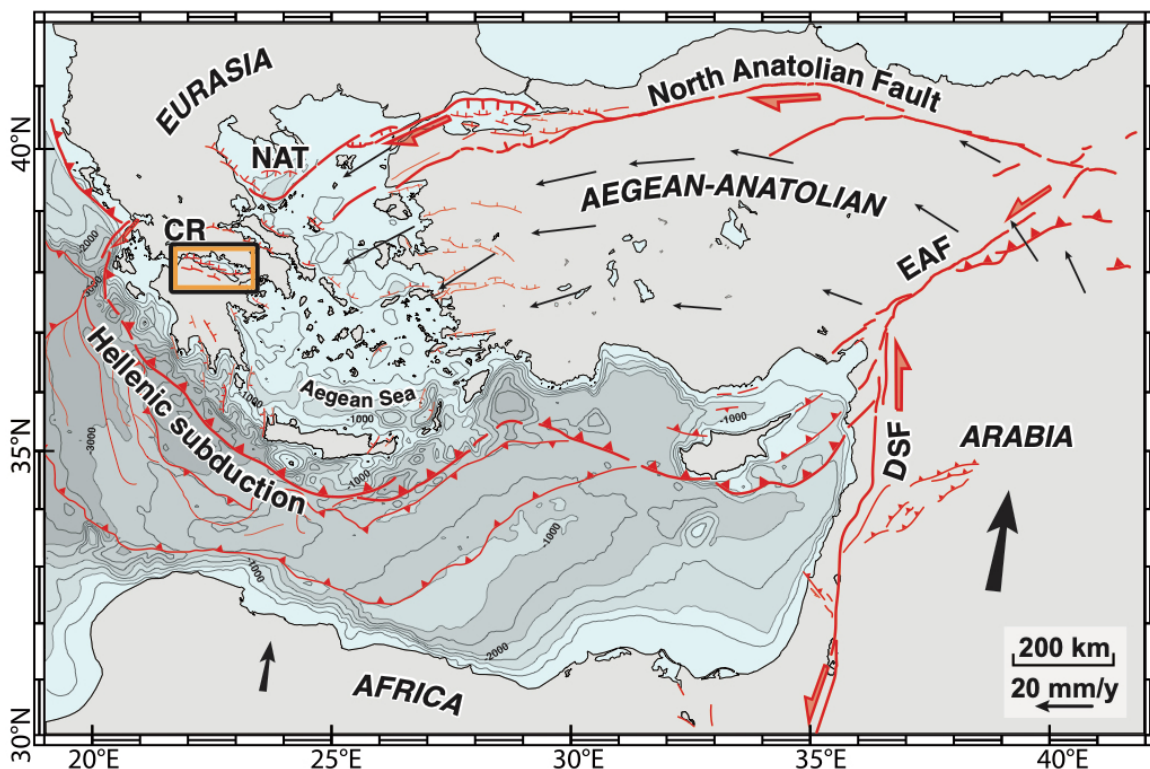


Fig. 1. Active tectonic faults, seismicity and GPS velocities of the W Turkey-Greece region. The map shows the main tectonic units, plate boundaries and active faults in the region, and the location of the Corinth Rift (CR). The bathymetry is modified from Huguen et al. (2004). The GPS vectors, with a fixed Eurasian Plate, are simplified from Le Pichon and Kreemer (2010). The map of active faults comes from Armijo et al. (1999) and Flerit et al. (2004) for the Aegean and North Anatolian areas, and Kreemer & Chamot-Rooke (2004) for the Mediterranean Ridge area. Line thickness and arrow size represent amount of slip to a first-order. NAF and EAF are the North and East Anatolian faults.

1.2 Did the rift develop continuously or after a disruptive tectonic event?

General consensus exists that early distributed extension (e.g., Seger and Alexander, 2009; Gawthorpe et al., 2017b) and basinward fault migration (e.g., Gawthorpe et al., 1994; Goldsworthy and Jackson, 2001) occurred before the marked present-day strain localization that characterizes the modern Corinth Rift (e.g., Armijo et al., 1996; Hubert et al., 1996). The onset of distributed extension in a 20–30 km-wide area south of the present rift is poorly constrained to 4–5 Ma (e.g., Doutsos and Piper, 1990; Ford et al., 2016), and led to continental and shallow water deposition in a protected setting (e.g., Gawthorpe et al., 2017a). In the southern flank of the modern rift, these deposits have been uplifted in extensional footwalls that are sequentially younger northward, thus recording basinward migration of normal faults and block tilting (e.g., Gawthorpe et al., 1994; Goldsworthy and Jackson, 2001; Ford et al., 2012). More recently (~1 Ma or less), the onset of activity of the present rift-bounding fault (Fig. 2) and the resulting dramatic increase in subsidence marked a sharp sedimentation shift both onland (e.g., Ori, 1989) and in the offshore (e.g., Sachpazi et al., 2003) and resulted in a basin-wide angular unconformity (e.g., Nixon et al., 2016).

Discrepancies around age, disruptive nature and overall tectonic relevance of the current rift-bounding fault(s) motivates the proposition of different models for rift evolution. Despite the singularities of each model, in this review we simply differentiate “continuous” and “disruptive” rift models. Continuous rift models, with or without an intervening low-angle fault, frame the faulting event within a continuous sequence of fault-block tilting in two-to-four undisrupted rift phases, i.e. the “Great Breaching” event within R2 at 2.2 to 1.8 Ma (Gawthorpe et al., 2017b) or Phase 3 onset at 0.7 ± 0.2 Ma (Ford et al., 2016). Continuous rift models suggest self-organization of normal faults and progressive strain localization since rift onset (e.g., Jolivet et al., 2010; Leeder et al., 2012; Ford et al., 2016; Nixon et al., 2016; Gawthorpe et al., 2017b). Contrarily, disruptive rift models characterize the faulting event as discontinuing and overwriting comparatively minor antecedent extension, i.e. a new rift-forming fault that leads to the rift fast increase in tectonic rates and the first-order switch

in rift tectonostratigraphy since <1 Ma (Ori, 1989; Armijo et al., 1996). Disruptive rift models suggest that a strongly-localized strain since fault onset (De Gelder et al., 2018) controls modern Corinth Rift geometry and its most defining features (e.g., Armijo et al., 1996). To assess rift evolution, we infer the degree of strain localization in the rift-bounding fault evaluating geometrical relationships and spatiotemporal variations in geologic and geomorphologic features with respect to the modern rift-bounding fault(s) at the scale of the entire rift. This allow us to propose a rift evolution model that acknowledges our new findings and integrates those by previous studies.

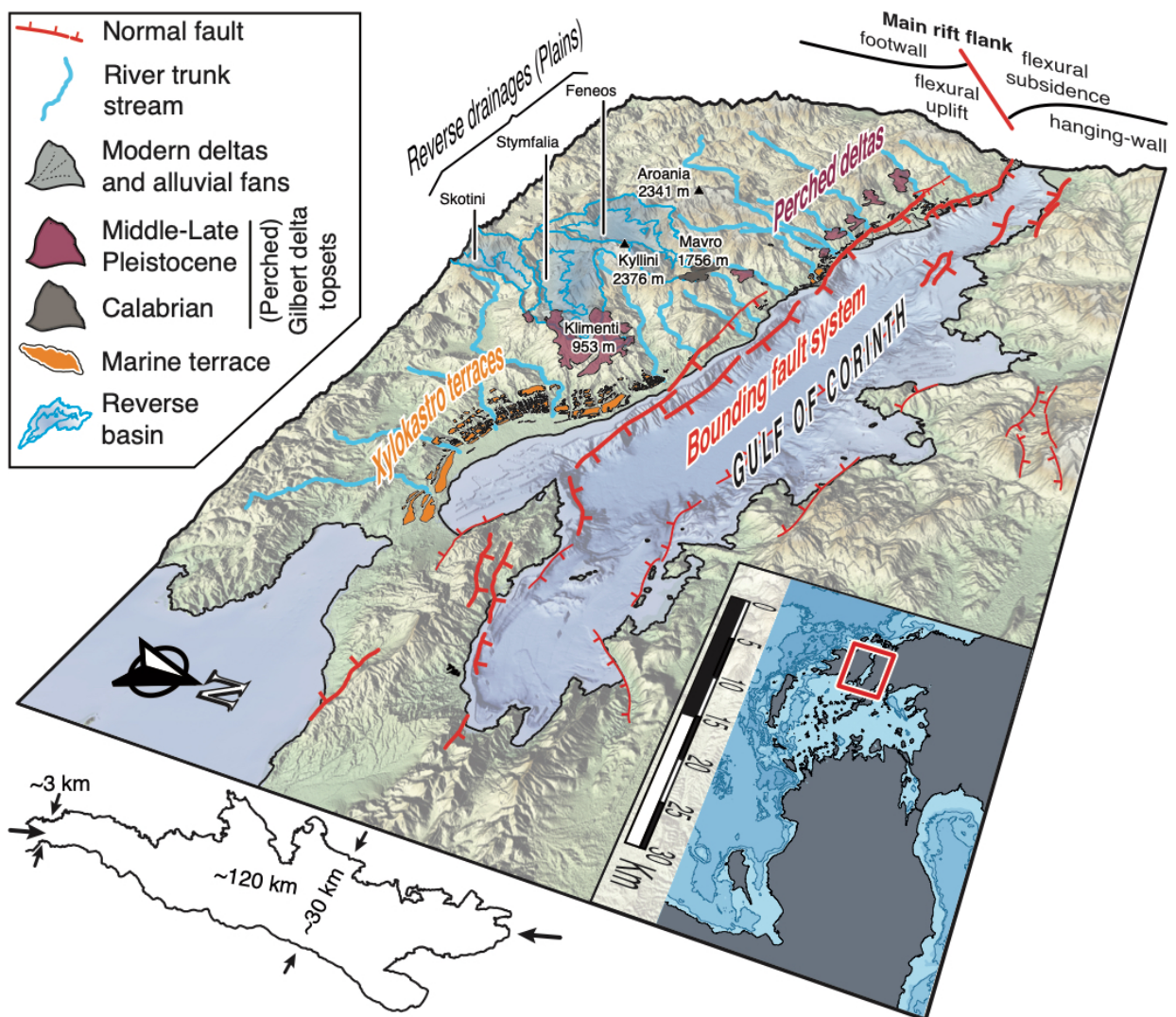


Fig. 2. 3D view of the Corinth Rift with representation of the main morphotectonic elements of the southern shoulder.

1.3 Is the rift main flank controlled by a low-angle or high-angle fault?

Present-day extension in the Corinth Rift is largely accommodated by the normal fault system that bounds the rift to the south (Fig. 2) with planar, high-angle fault planes dipping north that rupture the surface seismically during the Holocene (e.g., Hubert, 1996; Rigo et al., 1996; Stewart and Vita-Finzi, 1996). South of the present-rift bounding faults, narrow tilted blocks with little footwall relief are bounded by mostly-inactive faults dipping $\sim 45^{\circ}$ - 60° north at the surface (Rohais et al., 2007; Bell et al., 2008; Ford et al., 2012). Individual normal faults have planar attitudes and remain steep at least until ~ 3 km depth (e.g., Taylor et al., 2011; Nixon et al., 2016) but fault geometries and dips at depth, with low- and high-angle faults being suggested (see Bell et al., 2017 for an overview), as well as fault down-dip dimensions are uncertain. Some research proposes that surficial planar faults sole into a low-angle ($<30^{\circ}$) detachment at shallow depths (Sorel, 2000) or near the base of the seismogenic layer (Rietbrock et al., 1996; Rigo et al., 1996; Jolivet et al., 2010). Alternatively, the rift flank may be controlled by a single, high-angle (40° - 60°) planar fault reaching at least the base of the seismogenic layer (Bell et al., 2017; De Gelder et al., 2018) or affecting the crust as a whole (Fernández-Blanco et al., 2019a). To infer fault geometry and mechanics at depth, we characterize the wavelength and amplitude of lithospheric elastic flexure associated with the rift bounding fault system across and along rift axis, by means of topobathymetric data, relief, the morphology of river trunks and catchments, and uplifted morphotectonic markers.

1.4 What mechanical model best describes the rift?

Aforementioned proposals for rift models and fault geometries imply mechanical differences with relevant rheological implications for the strength of the lithosphere beneath the Corinth Rift (see two end members in Fig. 3). Continuous low-angle detachment models assume combined shear (Barbier et al., 1986) in the Corinth Rift transiting eastwards to simple shear rifting (Wernicke, 1981) in the central Aegean. Continuous high-angle fault models infer pure shear rifting (McKenzie,

1978a) south of the present Corinth Rift evolving to a flexural cantilever model (Kusznir et al., 1991) in its rift-bounding fault. Disruptive models infer a flexural cantilever rift that overwrites prior extension (whether pure or simple shear) at younger times, implying that the modern rift is temporal structure sustained by protracted seismicity (King et al., 1988).

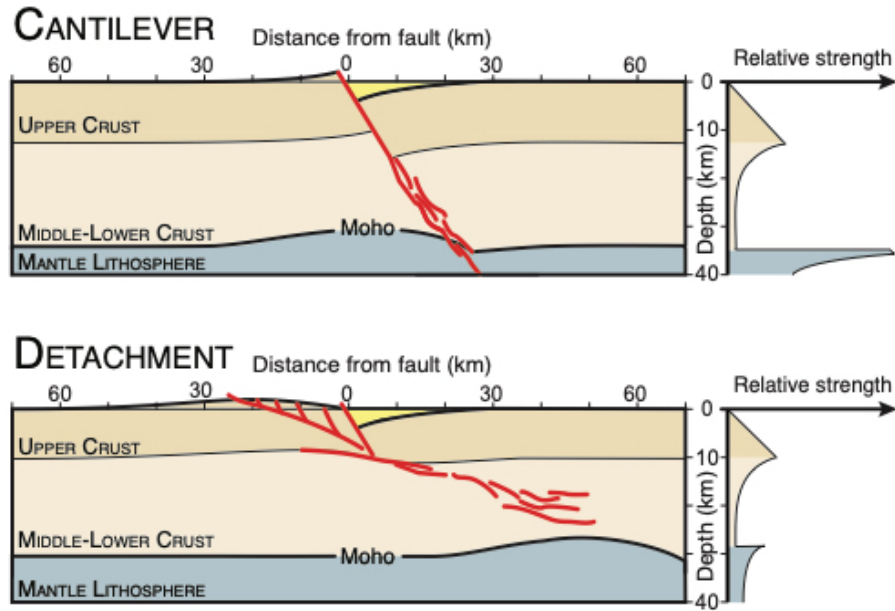


Fig. 3. End-member models proposed for the Corinth Rift and representative strength profiles. In the upper section is the flexural-cantilever rift model (Kusznir et al., 1991) proposed by Armijo et al. (1996), and in the lower section is the core complex-detachment rift model (Buck, 1991) proposed by Jolivet et al. (2010). Their representative strength profiles are shown on to the right of each model.

Mechanical models and the associated behaviour of the lithosphere can be discriminated analysing the bounding fault footwall flexure (King and Ellis, 1990; Buck, 1991, 1993; Resor and Pollard, 2012; De Gelder et al., 2018). In the SE flank of the modern rift, strain markers depicting fault flexure can be produced coseismically by 40° - 60° upper crustal normal faults and maintained through a relatively strong upper portion of the lower crust, and postseismic viscous relaxation occurring mostly in the basal lower crust or upper mantle (De Gelder et al., 2018). This rheology, constrained across rift strike in a 2D transect, may define the behaviour of continental lithosphere responding to localised deformation on 10^3 - 10^4 yr timescales (De Gelder et al., 2018). Geometry

and wavelength of geologic and geomorphologic elements should provide clues on the potential continuation of this rheology along rift strike. To discriminate among rift mechanical models, we compare (i) rift extent and geometry as well as the location, distribution and geometry of its main geologic and geomorphologic elements with (ii) the rift-bounding fault extent, elastic flexure, and footwall uplift rates. We also assess the rift-bounding fault down-dip length and depth extent deriving its surface length and using normal fault aspect ratios and fault dips from the literature.

1.5 Why are geodetic extension rates at odds with long-term extension rates?

The Corinth Rift has remarkably high seismicity and tectonic rates, even in relation to other sites along the Aegean, which is one of the most active extensional continental regions worldwide (e.g., McKenzie, 1978; Armijo et al., 1996; McNeill et al., 2005; Jolivet et al., 2013). Rates of extension in the Corinth Rift are comparable to mature, fully-developed plate tectonic diverging boundaries (cf., Briole et al., 2000; Müller et al., 2008; Tetreault and Buitert, 2018) with GPS velocities increasing westward from $\sim 11 \text{ mm}\times\text{yr}^{-1}$ to $\sim 16 \text{ mm}\times\text{yr}^{-1}$ (e.g., Avallone et al., 2004). However, modern extension rates have increased by up to more than one order of magnitude since extension started (e.g., Ford et al., 2012) and geodetic data is at variance with finite strain and long-term average extension rates (e.g., Bell et al., 2011). The rift shows a greater amount of long-term extension eastwards, where it is significantly broader, has the largest depocenters and its maximum basement subsidence (e.g., Bell et al., 2011). To understand the discrepancy between present and past extension rates, we reconstruct the development of structural relief in the rift margin in the context of the modern rift-bounding fault growth and propose how it relates with rift opening in time.

1.6 Why is the rift markedly asymmetric in its centre and symmetric at rift ends?

The modern Corinth Rift presents a large degree of asymmetry, across and along rift axis (Fig. 2). Across rift axis, the modern rift-bounding fault system sets a markedly asymmetric half-graben for $\sim 60 \text{ km}$ along strike in the rift center (Fernández-Blanco et al., 2019a). Fault flexure along the

bounding faults result in coupled footwall uplift to the south (uplift rates up to $\sim 1,7 \pm 0.1 \text{ mm} \times \text{yr}^{-1}$ near the Xylokastro Fault) (Armijo et al., 1996; De Gelder et al., 2018) that controls the landscape (Fernández-Blanco et al., 2019b), and hanging-wall subsidence to the north (rates of $\sim 3,6 \text{ mm} \times \text{yr}^{-1}$ in the gulf center) (Moretti et al., 2004) that sets sedimentation in the gulf and the northern coast (Bell et al., 2009; Elias et al., 2009). Vertical motions in relation with localized strain in the bounding fault system led to a $\sim 5 \text{ km}$ high-amplitude tectonic relief in the centre of the rift (e.g., Armijo et al., 1996; De Gelder et al., 2018) that highly contrast with the preceding low-amplitude relief (e.g., Ori, 1989).

Westwards along axis, the rift changes from a wide, markedly asymmetrical half-graben to a symmetrical and narrow graben as the gulf width changes from $\sim 30 \text{ km}$ to $\sim 3 \text{ km}$ and its seafloor depth decreases from $\sim 850 \text{ m}$ to $\sim 200 \text{ m}$ (Fig. 2). By contrast, modern deltaic systems are significantly more developed in the west than in the centre of the rift (e.g., Seger and Alexander, 2009). Similarly, the extent of now-exposed marine Plio-Pleistocene rocks reduces to half in the west (e.g., Ori, 1989), whereas syn-tectonic sedimentary wedges of the rift-bounding fault decrease in thickness (e.g., Nixon et al., 2016). In the same direction, overall fault orientations change from $N105^\circ E$ to $N90^\circ E$ (Fig. 2) and mean topography reduces by $\sim 400 \text{ m}$. The morphology of the rift towards the east is more complex, as the rift-bounding faults change their orientation to $N45-55^\circ E$ and the orientation of other faults is more variable (Fig. 2). The east rift seems more symmetric (e.g., Sakellariou et al., 1998, 2007) than at its centre. To understand changes in rift geometry, we assess the activity of presently active faults in the rift-bounding fault system since their onset, as well as their footwall uplift rates, and compare their along-strike variations against the finite geometry and wavelength of topobathymetric data in different rift sectors.

1.7 Is the bounding fault system propagating along strike?

Fault propagation westwards is inferred by sedimentological evidence for the central and west rift (Ford et al., 2016; Gawthorpe et al., 2017b), and the coalescence of smaller, antecedent depocenters into a joint depocenter growing since ~240 ka in the west rift (Nixon et al., 2016). More indirect lines of evidence point to equivalent along-strike propagation of the bounding fault system at the whole rift scale. For example, the onset of activity in the oldest bounding faults of the rift center (Armijo et al., 1996; Gawthorpe et al., 2017a; Fernández-Blanco et al., 2019a) is not directly correlatable with microseismicity clusters and Mw5+ earthquakes recording recent seismicity in active faults at rift ends (Jackson et al., 1982; Ambraseys and Jackson, 1990; Hubert et al., 1996; Hatzfeld et al., 2000; Bernard et al., 2006; Godano et al., 2014; Duverger et al., 2015). This suggest more protracted fault activity and thus a better-expressed fault hierarchy in the rift center, that we test producing a hierarchical map of active faults and evaluating their kinematic relation with regards to the modern rift-bounding fault(s). We also assess the potential linkage of individual fault strands in time, and thus whether the rift-bounding fault(s) grew and propagated along strike by comparing individual fault along-strike lengths at surface and the geometry of their fault footwall relief. Coupling this with evidence with footwall river tectonic knickpoints allow us to propose a sequence of along-strike fault growth.

1.8 Is the bounding fault system a series of individual faults or a composite fault?

The rift-bounding normal fault system setting the south coast of the gulf is formed by en-échelon faults ~10-25 km-long, with ~130 km cumulative length (Fig. 2). Markers uplifting in the footwalls of individual faults have been extensively studied, often to derive slip or uplift rates (e.g., Collier et al., 1992; Armijo et al., 1996; Stewart, 1996; Stewart and Vita-Finzi, 1996; Koukouvelas et al., 2001; Stefatos et al., 2002; Houghton et al., 2003; Leeder et al., 2003; McNeill and Collier, 2004; Pantosti et al., 2004; Pavlides et al., 2004; Verriós et al., 2004; Palyvos et al., 2005, 2007, 2008; Turner et al.,

2010; Karymbalis et al., 2016b; De Gelder et al., 2018). Slip rates inferred are consistently high along the entire rift margin, with minima ranging from 4 mm×yr⁻¹ (McNeill and Collier, 2004) to 7 mm×yr⁻¹ (Armijo et al., 1996), which points to a potential kinematic link among fault segments that has never been assessed at the rift scale. Here, we address this question by studying the footwall relief geometry of the rift-bounding fault(s) at rift scale, as well as its correlation with individual fault segments and uplifted, correlatable markers of paleo-sea level, that we also use as proxies for fault displacement profiles in time.

1.9 Key geologic elements in the modern rift and approach

Morphologic and stratigraphic markers record exceptionally well the growth of the modern Corinth Rift bounding fault(s). The current faults bounding the rift developed in a protected environment (e.g., Gawthorpe et al., 2017a), and at coeval times (600-700 ka) and thereafter, bathymetric seals at the rift ends controlled water passage between the open sea and the gulf (Roberts et al., 2009). This singular setting led to rhythmical switches in sedimentation; lacustrine in sea-level lowstands and marine in sea-level highstands (Heezen et al., 1966; Collier, 1990). This results in age-correlatable sequences of wave-cut marine terraces onshore (e.g., Armijo et al., 1996; McNeill and Collier, 2004) (Fig. 2) and lacustrine-marine alternations offshore (Sachpazi et al., 2003; Nixon et al., 2016) that together record the growth of the rift-bounding fault at intervals set by ~120 ky glacial-interglacial cycles (~120 ky; De Gelder et al., 2018). Onshore-offshore strain markers delineate the elastic flexure of the lithosphere and an uplift/subsidence ratio of 1:1.2-2.4 (De Gelder et al., 2018) in the SE rift margin that agrees well with ratios in the SW rift margin (McNeill et al., 2005). Comparable strain markers uplifted in the rift flank, its topobathymetry and other geomorphic elements (Fig. 2) holding similarly relevant constraints are hitherto unexplored collectively at the rift margin scale.

We constrain the growth of the bounding fault(s) and the uplift history of the rift southern shoulder to evaluate the rift mechanical models and infer implications for the recent evolution of

the Aegean. We have reassessed, (re)mapped and integrated geologic and morphotectonic data into a new map of the Corinth Rift. We use our compilation map, and analyses of relief along and across the rift axis to characterize the morphology of the rift and its relation with first-order geologic features. We derive the kinematic evolution, along-strike sequence of growth, and vertical rate of growth of the present rift-bounding fault system, and thus the growth of relief in the rift southern shoulder in time. For this, we analyse correlated time-strain markers and tectonic knickpoints at rift scale using normal fault mechanics. Our integration and novel approaches allow us to infer the wavelength and amplitude of the mechanical, elastic flexure of the lithosphere that is associated with the master fault and correlates with the along-strike extent of the rift. We then derive uplift rates in the master fault footwall and infer its fault down-dip length and geometry. We conclude that the master fault is highly localised and controls the evolution of the modern Corinth Rift. We use these constraints to build a geological model of fault growth and propagation at rift scale and the concomitant opening of the modern Corinth Rift. We compare our model with previous models proposed for the rift and discuss its implications in the context of the evolution of the lithosphere and plate boundary conditions of the Aegean.

2. Geologic elements to understand normal fault mechanics

2.1 Normal fault mechanics

Research deduced a fault scaling relationship between maximum fault displacement (D_{max}) and fault length (L) from empirical and theoretical observations (Cailleux, 1958; Walsh and Watterson, 1988; Cowie and Scholz, 1992a, 1992b; Dawers et al., 1993; Schlische et al., 1996):

$$D_{max} = \zeta \cdot L^n ,$$

ζ being a proportionality constant with a mean value of 3×10^{-2} , and $n \sim 1$ when derived as the best

fit regression through datasets of large fault populations spanning seven orders of magnitude (e.g., Scholz, 2002), i.e. the maximum fault displacement (D_{max}) is 3% of fault length (L). Also, systematic quantifications of fault length-to-height ratios performed in individual normal faults defined fault aspect ratios ranging between 0.5 to 8.4, with >2.5 and <4 as the most common values for merged or interacting faults that are restricted vertically by the free surface (e.g., Nicol et al., 1996).

Fault scaling relationships and fault aspect ratios, taken together, are fundamental means to estimate fault dimensions and extent at depth. Barring complicating factors, a hypothetical normal fault with an at-surface trace of 10 km should have a maximum displacement of ~ 300 m and reach a down-dip dimension ranging between ~ 1.25 and 20 km, with most common values ranging between ~ 3 and 4 km. Estimated down-dip lengths probably exceed these values, as faults are commonly wider along their strike below the subsurface. Fault down-dip dimension can be coupled with its dip to estimate fault extent at depth.

Normal faults growing self-similarly by tip propagation have distinct individual displacement profiles with displacement maximum at the centre of the fault total length and displacement minima at its ends (e.g., Dawers et al., 1993; Manighetti et al., 2005). Elliptical to triangular fault displacement profiles are common, although mechanical restrictions like adjacent faults and/or original location of the fault nucleation point results in other shapes (e.g., Manighetti et al., 2001, 2005). The displacement profile of single normal faults is similarly modified during fault growth by deviation of the local stress fields at its tips as it interacts mechanically with adjacent faults (e.g., Willemsse, 1997; Gupta and Scholz, 2000). This intrinsic characteristic of normal fault displacement profiles help evaluate whether fault segments adjacent at the surface are connected at depth.

Whereas unconnected faults that are initiating mechanical interaction may have a displacement profile with more than one maxima and reduced aspect ratios, fault segments

mechanically linked at depth show a single displacement profile for their summed fault lengths and normal aspect ratios (e.g., Anders and Schlische, 1994; Dawers and Anders, 1995; Gupta and Scholz, 2000; Manighetti et al., 2001, 2005). Fault segments that grew independently and later linked may show fault displacement profiles with short wavelengths within an overarching, composite displacement profile of large wavelength (e.g., Cowie and Roberts, 2001; Whittaker and Walker, 2015). Between initial mechanical interaction and full linkage of individual fault segments, short-lived increased aspect ratios and transient “under-recovered” displacement profiles occur as lateral tip propagation and fault lengthening is limited while faster-than-normal displacement takes place at the linkage zone, in order to reach a new “recovered” single-fault profile (e.g., Cartwright et al., 1995).

2.2 Geologic elements used as fault mechanics proxies

In the following, we differentiate two rift sectors on the basis of the strike of the rift-bounding fault system (Fig. 4): “easternmost” rift (faults trending NE-SW to ENE-WSW, in the Perachora peninsula and offshore north of it) from “southern shoulder” (WNW-ESE to E-W strikes, W of the Perachora peninsula). We further identify three footwall sectors in the rift southern shoulder, where we perform most of our analyses, using the position and distance of the coast and main morphological elements from the active fault system; “east” (east of Kiato), “central” (from Kiato to Akrata) and “west” (from Akrata to Psathopyrgos) (Fig. 4). For the later, we differentiated as needed between “E west” sector, related to the Eliki Fault Array (Eliki FA) and “westernmost” sector, related to faults farther west. Hereon, we distinguish individual faults (F) from fault arrays (FA).

The activity and slip of active normal faults control the geometry and maximum elevation of mountain fronts uplifting on their footwalls, especially in semiarid regions (Wallace, 1978; Armijo et al., 1986, 1991). Fault activity and slip also control the evolution of extensional footwall relief, fluvial catchment areas and their outlet spacing (Densmore et al., 2004). Here we use geomorphic

proxies to constrain the growth of the bounding fault system since its onset: topographic stacked swath profiles, footwall relief, and analyses of river profiles and knickpoints, paleoshoreline angles of marine terraces and topset-foreset contacts of Gilbert-type deltas (Fig. 5).

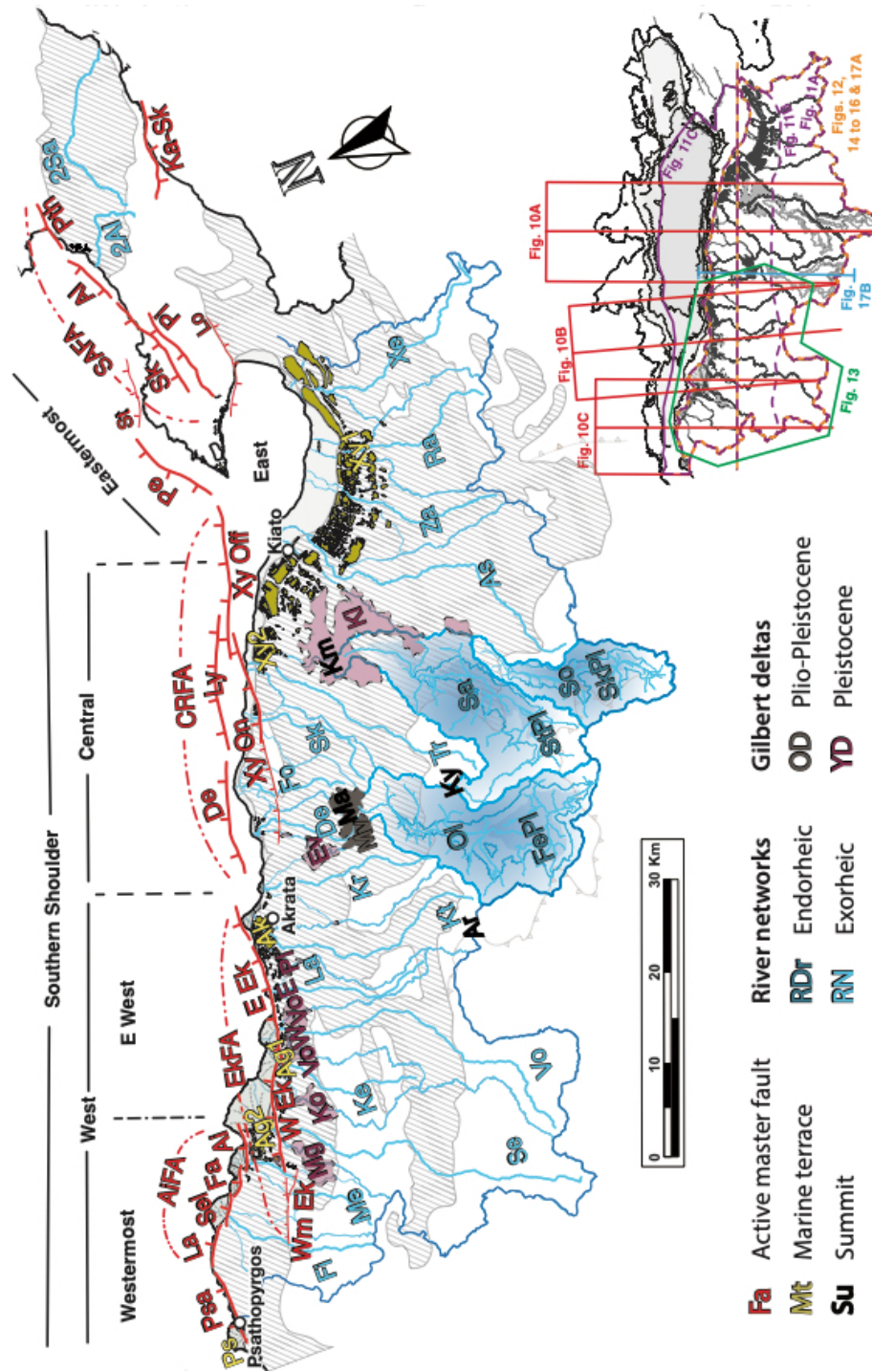


Fig. 4. Index map, showing the main elements of the Corinth Rift considered in this review. The lower right inset shows the extent of the DEM for across-axis (red) and along-axis (purple) stacked swath profiles and their projection lines, as well as the location of other figures of the western rift (green), the full rift (orange), and cross sections (in blue). Abbreviation of the main elements, from east to west. *Main active faults:* Psatha (Pth); Kakia-Skala (Ka-Sk); Alepochori (Al) and Skinos (Sk); Strava (St); Pisias (Pi); Perachora (Pe); Loutraki (Lo); Central Rift Fault Array (CRFA) [composed of Xylokaastro Onshore (Xy On), Xylokaastro Offshore (Xy Off), Lykoporia (Ly) and Derveni (De)]; Eliki Fault Array (EkFA) [with the East Eliki (E Ek) and West Eliki (W Ek)]; and the Aigio Fault Array (AiFA) [inclusive of Aigio (Ai), Fasouleika (Fa), Selianitika (Sel), Lambiri (La) and Psathopyrgos (Psa)]. *Marine terraces location:* Xylokaastro (Xy1 & Xy2), Akrata (Ak), Aigio (Ag1 & Ag2), and Psathopyrgos (Ps). *Pleistocene perched Gilbert deltas:* Klimenti (Kl), Evrostini (Ev), Platanos (Pl), Vouraikos East (VoE) and West (VoW), Kolokotronis (Ko) and Meganitis (Mg). *Late Pliocene (perched) Gilbert delta:* Mavro (Mv). *Main drainage systems:* Xerias (Xe), Raizanis (Ra), Zapantis (Za), Asopos (As), Trikalitikos (Tr), Fonissa (Fo), Skoupeiko (Sk), Derveni (De), Krios (Kr), Krathis (Kt), Ladopotamos (La), Vouraikos (Vo), Kerinitis (Ke), Selinous (Se), Meganitis (Me) and Finikas (Ph). *Internally drained basins and their plains:* Soutini (So) and Skotini Plain (SkPl); Safenetos (Sa) and the Stymfalia Plain (StPl); and Olvios (Ol) and the Feneos plain (FePl). *Main summits:* Klimenti (Km) and Mavro (Ma) at the front and Kyllini (Ky) and Aroania (Ar) at the back.

2.2.1 Stacked swath profiles “2.5-D” topography

Topography-based morphotectonic evidence provides a first-order understanding of the degree and time-scale of activity of contributing structures in settings where tectonic forcing outpaces climatic and erosive factors (e.g., Armijo et al., 1986; Klinger et al., 2000; Densmore et al., 2004). Stacked swath profiles now allow for topographic assessment at the scale of large, orogen-scale objects (Armijo et al., 2015).

A stacked swath profile contains a significant number of consecutive parallel swath profiles derived from topographic data, commonly Digital Elevation Models (DEMs), plot together as hairlines orthogonally to their strike. By stacking swath profiles, the resulting profile highlights a “2.5D” view of topographic coherence in depth, allowing the distinction of large-scale structural and morphological features that are continuous over large scales. Armijo et al. (2015) originally used stacked swath profiles to illustrate the major morphological features of the Central Andes coastal margin, an exercise either difficult or entirely impossible with other means. Hereunder, we use stacked swath profiles of average topography at the scale of the whole Corinth Rift to describe the variation of topography and its interrelation with morphological elements. Stacked swath profiles shown here are produced as a pile of parallel swath profiles of dynamically defined width. Swath width is the result of dividing DEM width along the projection line by chosen number of swaths. For

all stacked swath profiles in this paper, the extent of the main fault footwall is set by the drainage of catchments discharging into the rift and the three largest reverse catchments.

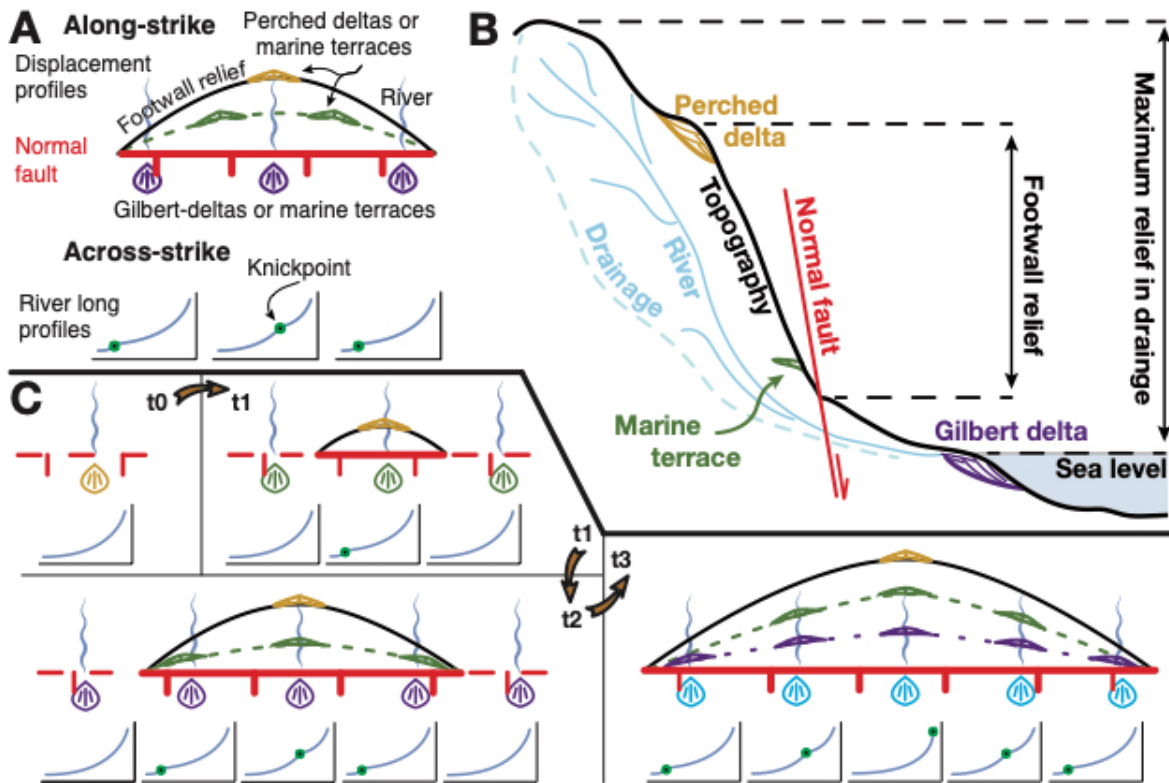


Fig. 5. (A) Schematic representations of elements in extensional footwalls in relation with their active faults in an along-strike view and footwall rivers and their tectonic knickpoints in across-strike view. **(B)** Elements of an extensional footwall and their relation with the proxies of relief used in this study. **(C)** Self-similar growth of a normal fault, as shown by geomorphic features in its footwall, in four time-steps: (t0) steady-state of a river network - Gilbert delta system; (t1) initiation of normal fault activity and footwall flexural uplift propels formation of a tectonic knickpoint and uplifts former Gilbert deltas; (t2) lateral growth of the normal fault leads to inclusion of rivers in its footwall, and the formation of new tectonic knickpoints and uplift of new Gilbert-deltas; (t3) lateral self-growth and perpetuation of t2. Similar constraints by Gilbert-deltas on fault displacement profile (albeit more accurate) can be inferred using marine terraces. Other inferences on fault displacement profiles can be obtained from footwall relief and total topography. Assuming that geomorphic features formed at each time-step are not eroded and can be dated, their location and height provide key constraints on the fault growth and displacement profile in time.

2.2.2 Footwall relief

The mountain front relief uplifting in extensional footwalls results from long-term uplift rate, and thus slip rate on its bounding fault. Range front relief results from cumulative fault displacement and can be used to infer the dimensions of the active fault and its history of growth and linkage

(e.g., Dawers and Anders, 1995; Gupta and Scholz, 2000). If erosion is effective and fault tip propagation and slip rate are coupled, the footwall relief maxima occurs at a uniform distance from their active fault trace (Densmore et al., 2005, 2007). Proxies for range front relief are therefore useful to assess the activity of range-bounding normal faults (Fig. 5B). We use an equivalent to range front relief, footwall relief, which approximates to the height of the first major slope break in the extensional footwall, measured vertically from the trace of their active normal faults (e.g., Whittaker and Walker, 2015), and can be used as a proxy to upper-limit fault displacement profile (Fig. 5).

We calculate the along-strike distribution of footwall relief in the Corinth Rift southern flank deriving the position of the first topographic break of slope in footwall topography (Fig. 5B) (see Whittaker and Walker, 2015). We defined a polygon of ~21 km measured inland orthogonally to the strike of each fault segment (Fig. 4) that covers the area of the topographic break of slope (sited <20km, often ~15km). We use a ~20m-wide topographic swath every 20 m perpendicular to the fault trace (~5000 in total), and project the footwall relief along fault strike, taken as N105°E.

We minimized errors related with the DEMs, but other uncertainties were not avoidable. We graphically attach an estimated uncertainty derived from two factors: confidence in accurate mapping of the fault and discrepancy between fault strike and chosen direction of projection (Figs. 4B & 5). The discrepancy between projection plane, representing the average fault strike, and the real fault strike is neglectable in the western rift, and increases for the central rift, where we estimate a maximum associated uncertainty of ± 50 m in the vertical that is not explicitly shown in the figures. A second uncertainty exist in the calculus of the footwall relief derived from potential inaccuracies in the position of the fault trace, which are minimal in the west rift, and increase eastwards where the fault lays underwater (Fig. 4). We estimate a maximum uncertainty of ± 250 m in the vertical for the central rift due to this effect, in combination with the unconstrained behavior

of the footwall relief sector that grows underwater. Farther east than Kiato town, the departure of the bounding fault basinward away from the coast (Fig. 4) results in uncertainties that are difficult to estimate, and we performed no calculus. With this exception, we are confident that the tectonic signal significantly overpasses the uncertainties at the scale of interest.

2.2.3 Longitudinal river profiles and tectonic knickpoints

Research attests that rock uplift rate or erosion rate are functionally related to river channel steepness, when normalized by upstream contributing drainage area (e.g., Snyder et al., 2000; DiBiase et al., 2010). This suggests that the relative rate of uplift or erosion can be approximated to river channel steepness, a relationship that can be described theoretically by quasi-physical stream power incision model (e.g., Howard, 1994). The detachment-limited stream power incision model describes river bed elevation change in time (dz/dt) as a function of upstream drainage area (\propto discharge) (Whipple and Tucker, 1999; Tucker and Whipple, 2002) and local channel slope. Combined with mass conservation it takes the form of

$$dz/dt = U \cdot E = U \cdot K \cdot A^m \cdot S^n .$$

Assuming that rock-uplift (U) and erosion rate (E) are equal leads to a local channel slope (S) defined by

$$S = (U/K)^{1/n} \cdot A^{-(m/n)},$$

A being the drainage area upstream, K a dimensional coefficient that encloses incision, substrate, climate and hydrology of erosion (e.g., Whipple, 2004), and m and n positive constants dependent on channel geometry, basin hydrology, and erosion processes (Howard, 1994; Whipple and Tucker, 1999; Whipple, 2004).

In detachment-limited rivers, local convexities or knickpoints provide first-order clues on the growth of normal fault systems. For example, a knickpoint will migrate upstream as a kinematic

wave (Rosenbloom and Anderson, 1994) after a increase in uplift rate due to an increase fault slip. While migrating upstream, knickpoints bound steeper downstream river reaches adjusted or adjusting to the new uplift conditions from flatter upstream river reaches unaware of the uplift rate change (Fig. 5A) (e.g., Whipple and Tucker, 1999; Snyder et al., 2000).

Fluvial geomorphology and normal faults scaling laws allow evaluation of the growth of extensional fault systems and their linkage in time, and inferences of tectonic and fault throw rates (e.g., Boulton and Whittaker, 2009; Whittaker and Boulton, 2012; Whittaker and Walker, 2015; Kent et al., 2016; Gallen and Wegmann, 2017). Whereas knickpoint retreat rates (map view) are fundamentally controlled by drainage area and bedrock erodibility (e.g., Wobus et al., 2006; Berlin and Anderson, 2007), knickpoint vertical propagation rates (profile view) are directly proportional to tectonic change amplitude (e.g., Whittaker et al., 2008). Hence, tectonic knickpoints migrate upwards predictably and have heights (measured from the active fault) that scale with the fault vertical displacement and footwall relief (e.g., Kent et al., 2016). A given set of tectonic knickpoints found in river drainages of extensional footwalls may thus be related to three fault-related events: fault initiation, fault linkage or fault slip rate increase (Whittaker and Walker, 2015; Gallen and Wegmann, 2017).

Here, we reproduce river profile geometry using Topotoolbox 2.0 (Schwanghart and Scherler, 2014), and perform knickpoint analysis with the χ -profiler package (Gallen and Wegmann, 2017). We analyse knickpoints in river trunks to assess their tectonic origin, which we corroborate examining knickpoints at similar heights in nearby tributary streams. We build our own coding routines to reproduce analytical procedures of tectonic knickpoint height against footwall relief projected along fault strike (as in Whittaker and Walker, 2015).

2.2.4 Marine terraces and Gilbert-type deltas

Correlatable marine terraces and/or Gilbert-type deltas can be used as strain markers and allow

reconstructions of former coastal landscapes. Marine terrace shoreline angles, at the intersection between the terrace and its inland-bounding cliff, best characterize sea level position during terrace formation, typically in sea level highstands (Lajoie, 1986; Anderson et al., 1999; Scott and Pinter, 2003). Similarly, Gilbert-type delta topset-foreset contacts set approximately at sea level (Gilbert, 1890) as proximal topsets extend the alluvial plain subaerially, and distal foresets prograde basinwards underwater. Sets of coeval morphotectonic markers, i.e. marine terraces of the same sea-level highstand or Gilbert deltas deposited at similar age may form sequentially along uplifting coasts and lead to inland uplifted sets that down-step coastwards into younger sets (Figs. 4C & 5). Land relative upwards motion between the formation of two sets of morphotectonic markers can be retrieved from the height difference between them, taking into account past sea-level positions. If coastal uplift occurs in extensional footwalls, the land upwards motion relative to the sea level is a proxy for fault displacement, and sets of coeval morphotectonic markers can be approximated to fault displacement profiles in time (Fig. 5C). Relative along-strike fault uplift rates can be derived when the age of such coeval morphotectonic sets is known.

Here, we project coeval morphotectonic markers of the southern flank towards the strike of the bounding fault(s) (Fig. 5). For the paleoshoreline angles of marine terraces, we follow Railsback et al. (2015) nomenclature for sea level highstands, and Masson-Delmotte et al. (2010) for highstand ages, i.e. MIS 5e (~124 ka), MIS 7e (~240 ka) and MIS 9e (~326 ka). Paleoshoreline angles belong to time-correlated and/or dated marine terraces with maximum heights at six locations close to the bounding fault(s) (e.g., Houghton et al., 2003; De Martini et al., 2004; McNeill and Collier, 2004; De Gelder et al., 2018) (Fig. 4), and the ages of Gilbert-type deltas come from Ford et al. (2016).

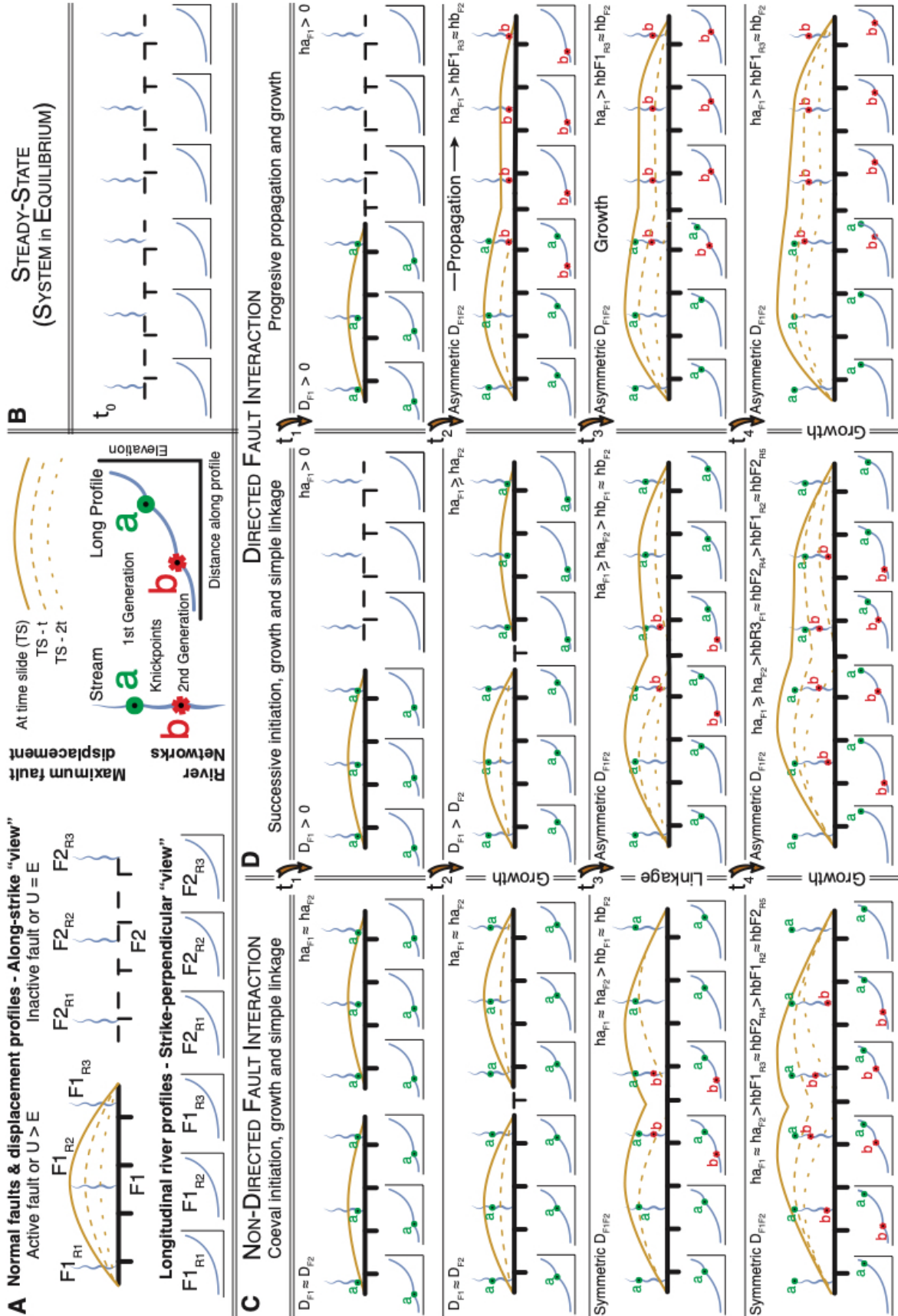
2.3 Approach for fault growth reconstruction in time

We propose a conceptual framework to reconstruct the growth and propagation history of active normal faults (Fig. 6). This framework uses the first-order morphological expression of topography,

relief, river catchments and morphotectonic markers in extensional footwalls (Figs. 4 & 5; sections 2.1 & 2.2), and is predicated on the response to fault linkage expected in fault displacement profiles and tectonic knickpoints of extensional footwall river profiles (e.g., Anders and Schlische, 1994; Dawers and Anders, 1995; Gupta and Scholz, 2000; Cowie and Roberts, 2001; Manighetti et al., 2001, 2005; Attal et al., 2008; Whittaker et al., 2008; Whittaker and Boulton, 2012; Whittaker and Walker, 2015; Gallen and Wegmann, 2017). This framework builds on these studies to discriminate, barring complicating factors, the relative time of activity of individual fault segments and their linkage mode; simple, directed or propagated (Fig. 6).

Co-linear normal faults that initiated activity concurrently and later interacted by simple (non-directed) linkage (Fig. 6C) present symmetrical fault displacement profiles at any time of their evolutionary history, both as individual and as composite faults. These normal faults show two sets of genetically-linked tectonic knickpoints. The oldest set of tectonic knickpoints develops at the moment of individual fault initiation and lays at higher elevations roughly similar in all river networks. The youngest set of knickpoints forms by fault linkage and lays at lower elevations, with knickpoint heights relatively higher for footwall river profiles in the area of fault linkage (Fig. 6C).

Fig. 6. Diagrams for fault displacement and tectonic knickpoint height of footwall rivers associated with different modes of initiation, growth and linkage or propagation between adjacent normal faults. **(A)** Main features of the diagrams in the rest of the figure. Top-left: normal faults in an along-strike view, their displacement profiles in time, as expressed in top-right, and a simple representation of six footwall rivers, whose longitudinal river profiles are represented in the lower-left. Lower-right: legend for the main components of the longitudinal river profiles. **(B)** Initial state, $t = 0$, for all cases, representing steady-state equilibrium. **(C)** Non-directed fault interactions, showing coeval growth and link. **(D)** Directed fault interactions, with normal faults that initiate with a preferential direction (rightwards), either by growth and linkage (left column) or by propagation (right column). In all cases, only the second generation of knickpoints developed in the linkage zones are near the tips of the faults (and shows a convex outward propagation mode). In all cases, F is for fault, D for fault displacement profile, R is for river, a and b are tectonic knickpoint sets, and h is elevation; thus, D_{F1F2} is a composite displacement profile including both faults, and $ha_{F1} > hb_{F1R3} \approx hb_{F2}$ means that the set a of tectonic knickpoints in fault 1 is at higher elevations than the set b of tectonic knickpoints in the third river of fault 1, which is at similar elevations than set b in fault 2.



Although co-linear normal faults initiating activity at different times may develop similarly asymmetric end displacement profiles (e.g., Manighetti et al., 2001, 2005), we envisage knickpoint arrays that are characteristic depending on whether faults are initially unconnected and link successively or new fault segments initiate by propagation. In the case of successive initiation (Fig. 6, panel D left), fault displacement profiles are symmetrical until the moment of linkage, and have a composite asymmetrical displacement profile from linkage until displacement profile “recovery” to single fault shape. The displacement maxima of the older fault segment sets at a higher position than the displacement maxima in the younger fault segment. Three families of knickpoints occur (Fig. 6D left); (i) an oldest set at the relative highest elevations exists solely in the oldest fault; (ii) another set appears at mid elevations solely in the fault with latest onset of activity; (iii) one more set of knickpoints occurs at the relative lowest elevations along the strike of the composite fault, with knickpoints that lay higher at its linkage zone and are absent at its tips.

In the propagation case (Fig. 6, panel D right), the displacement profile is only symmetrical in the oldest fault segment at times before propagation. As long as new propagation takes place at a faster pace than displacement profile “recovery” to single composite fault form, the displacement profile remains elongated and relatively flat, with its lowest displacement maxima in the sense of propagation (Fig. 6D right). Knickpoint families are expected to occur at the moment of initiation of each fault segment, occupying relatively lower positions in the sense of propagation and effectively marking the extent of propagation at any given time.

3 The modern Corinth Rift and its main geologic elements

We compiled, reassessed and (re)mapped active tectonic, tectonomorphic and geologic information from 30+ papers and published maps into a new map at the scale of the rift (Fig. 7). We provide in the supplementary material a detailed account on the data used, data manipulation and data source, as well as shapefiles and KML files (topobathymetric DEM, 5-level hierarchy active faults, marine

terraces, Gilbert-delta topsets, and river streams and their catchments) (Suppl. Mat A & C to G).

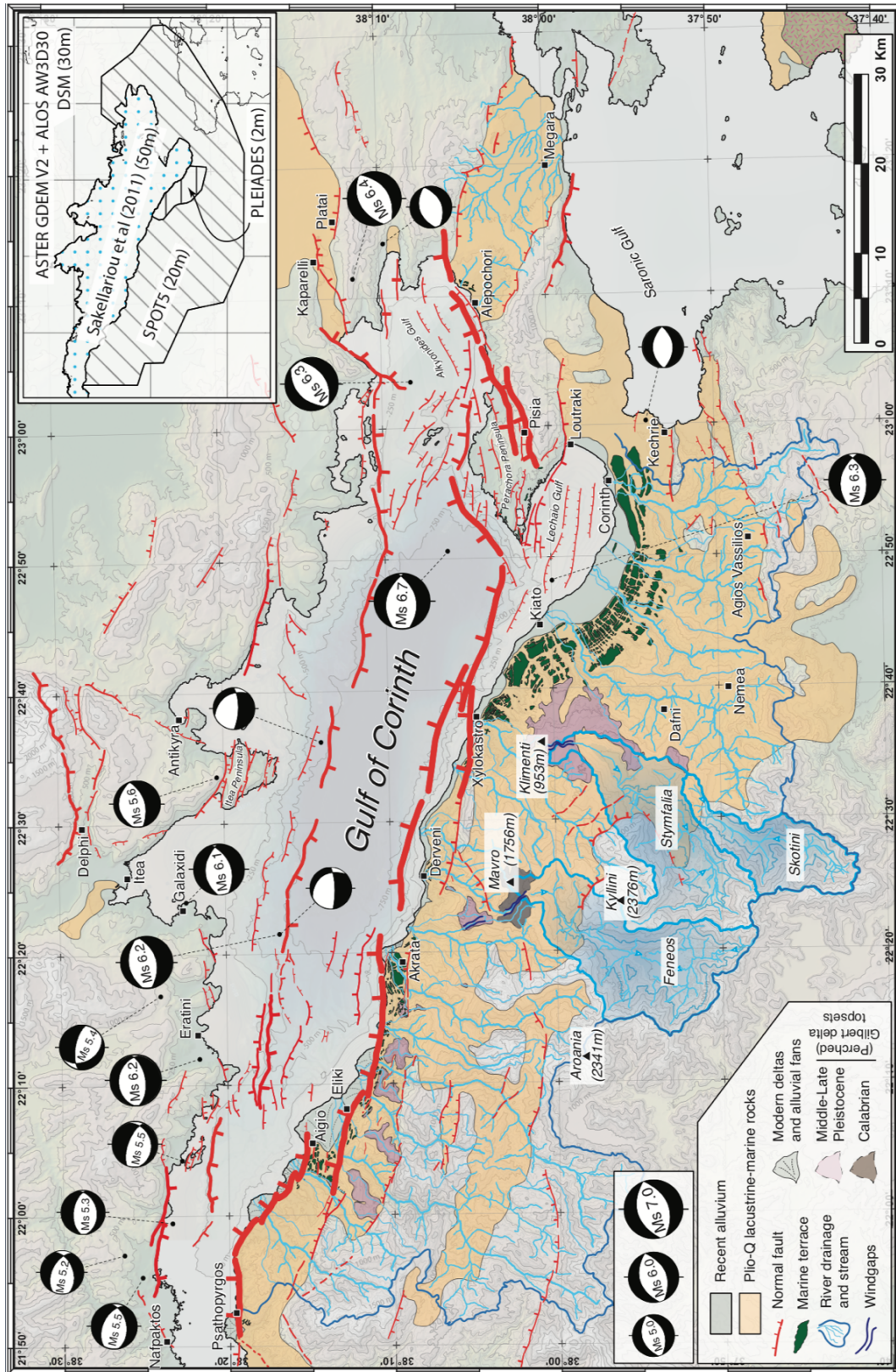


Fig. 7. Tectonomorphologic and active tectonics map of the Gulf of Corinth. Based on a compilation, reassessment and remapping from 40+ contributions, and own mapping (see Suppl. Mat. A). Inlet shows the different DEMs used for the topobathymetry.

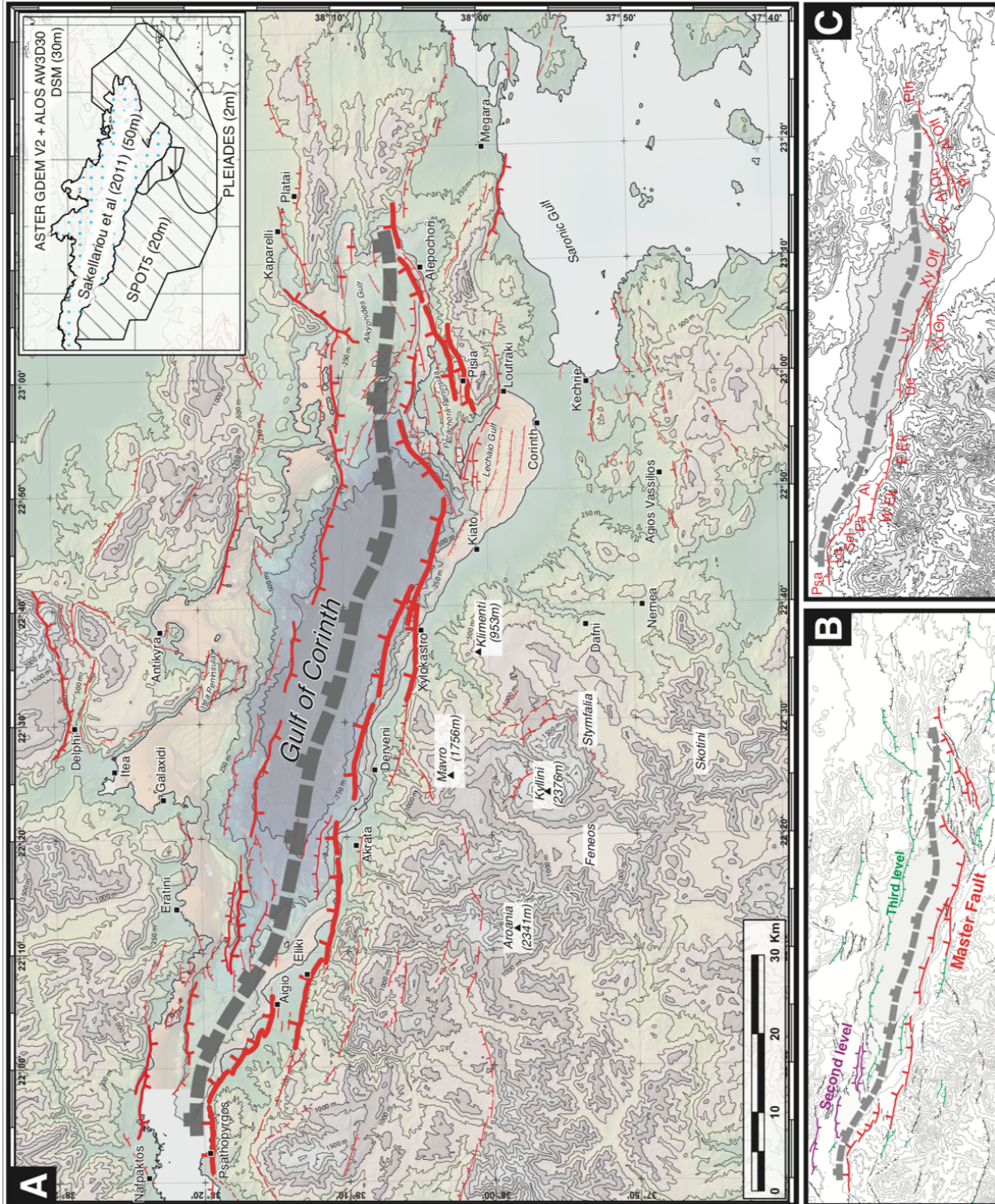
3.1 Active normal faults

The present-day relief and geometry of the Gulf of Corinth is governed by the overall E-W normal faults dipping north bounding the rift to the south (e.g., Doutsos and Piper, 1990; Nixon et al., 2016) (Fig. 8). North of the bounding fault system, parallel faults dipping south and conjugate faults are kinematically linked to and passively accommodating motion along the master fault system (e.g., Stefatos et al., 2002), and are hereon referred to as antithetic, conjugate or secondary fault systems. Faults in the westernmost rift northern margin are probably an exception (e.g., Beckers et al., 2015). This hierarchical attitude of the Corinth Rift faults results in an overall N-S to NNE-SSW extension direction (e.g., Vita-Finzi and King, 1985; Hatzfeld et al., 2000).

3.1.1 Attitude, rates and ages along the bounding fault system

The Corinth Rift main active fault system (Fig. 8C) trends NE-SW to ENE-WSW in the easternmost rift, and WNW-ESE to E-W in the central and west rift, dipping NW and N respectively. These active normal faults cut the Hellenic nappes at a high angle, as well as a former set of normal faults with WNW-ESE trends that bounded (now exposed) Plio-Pleistocene basins (e.g., Collier et al., 1992; Armijo et al., 1996). This inference is readable in the easternmost rift (e.g., Leeder et al., 1991; Gawthorpe et al., 1994) where ESE-striking extensional faults bounding former depocenters are cross-cut by the younger fault system. A similar observation is not clear for the central and west rift, and both antecedent and presently active fault systems are sub-parallel to each other.

Fig. 8. Map of Corinth Rift active faults. **(A)** Corinth Rift topobathymetry and the map of active faults. The topobathymetry is derived from a merged DEM, and the active faults map comes from own mapping and reassessment of fault maps from other contributions (see section 3.1). **(B)** Highlight of the three highest levels of our fault hierarchy. **(C)** Master fault (acronyms as in Fig. 3). In grey for all panels, a representation of an hypothetical composite master fault at seismogenic layer basal depths (~10 km) with similar high-angle north dips and planar attitudes than at-surface faults bounding the rift at present.



In the Corinth Rift south margin, variable along-strike uplift rate due to upward footwall elastic flexure ranges from $\sim 0.2\text{-}0.3 \text{ mm}\times\text{yr}^{-1}$ to potentially up to $1.5\text{-}2 \text{ mm}\times\text{yr}^{-1}$ (e.g., Collier et al., 1992; Armijo et al., 1996; Stewart and Vita-Finzi, 1996; Leeder et al., 2003; McNeill and Collier,

2004; Pavlides et al., 2004; Turner et al., 2010; Karymbalis et al., 2016b; De Gelder et al., 2018). A regional uplift signal, estimated between 0 and $0.3 \text{ mm}\times\text{yr}^{-1}$ (e.g., Armijo et al., 1996; Turner et al., 2010) is markedly overpassed by the master fault footwall uplift everywhere except in the east rift. Footwall catchments show that uplift rate and slip rate are maximum in the centre of the rift, minimum in the east rift and intermediate yet high in the west rift (Fernández-Blanco et al., 2019a).

In the central rift, the Offshore and Onshore Xylokastro F ($\sim 31\text{-}35 \text{ km}$ at-surface length), the Lykoporia F ($\sim 15 \text{ km}$) and the Derveni F ($\sim 13 \text{ km}$) trend WNW-ESE and dip N, and compound the Central Rift FA (Figs. 4, 7 & 8). Except for the Onshore Xylokastro F, the Central Rift FA runs off but close to the shore and has the largest fault offset observed in the rift (e.g., De Gelder et al., 2018). Fault-scaling relationships (e.g., Dawers et al., 1993) and deltas uplifted in its footwall (De Gelder et al., 2018) suggest that the Central Rift FA is either the oldest fault segment leading the latest phase of extension or it has the fastest uplift rate. The Xylokastro F has estimated uplift rates of $\sim 1.3\text{-}1.7 \text{ mm}\times\text{yr}^{-1}$ and slip rates of $4.5\text{-}9 \text{ mm}\times\text{yr}^{-1}$ for the last 326-410 ka, and linear extrapolation of uplift rates derived from marine terraces to either the Mavro or the Klimenti deltas suggest an age of fault activity onset of $\sim 1 \text{ Ma}$ or slightly older, respectively (Armijo et al., 1996; De Gelder et al., 2018). We favour an age of $\sim 1 \text{ Ma}$ over other estimates, such as stratigraphic correlations suggest the fault is $\sim 2 \text{ Ma}$ (Gawthorpe et al., 2017b), given the uncertainty involved in assigning chronostratigraphic significance to systems tracts in settings with marked spatial variations in vertical motions (Gawthorpe et al., 2017a). We further bracket the onset of fault activity between $\sim 1 \text{ Ma}$ and the $\sim 620 \text{ ka}$ age assigned to the depocenter of the Central Rift FA (Nixon et al., 2016). The main fault system changes its strike in the east rift, increasing in distance eastwards from the coast while decreasing in displacement and footwall topography (Figs. 4, 7 & 8). Here, the proposed rock uplift rates of $\sim 0.4 \text{ mm}\times\text{yr}^{-1}$, obtained near the coast at $\sim 15 \text{ km}$ of the main fault system, are close to those estimated for the regional uplift (Karymbalis et al., 2016b).

In the west rift, the Eliki FA (~29-32 km), compounded of East Eliki F (~17 km) and West Eliki F (~12-15 km), has an overall E-W strike and N dip (Figs. 4, 7 & 8). Estimated rates of footwall uplift for East Eliki F are ~1-2 mm×yr⁻¹ for Holocene times (Stewart, 1996; Stewart and Vita-Finzi, 1996) and ~1-1.5 mm×yr⁻¹ for Late Pleistocene, with estimated slip rates of 4-7 mm×yr⁻¹ (McNeill and Collier, 2004). In the westernmost rift, the Aigio F (~6 km), Fasouleika F (~4.5 km), Selianitika F (~4 km) and Lambiri F (~5.5 km) are part of the north dipping Neos Erineos Fault zone that strikes WNW-ESE to NW-SE and that we refer to as the Aigio FA, for simplicity (Figs. 4 & 8). Unlike elsewhere in the southern flank, footwall topography trends are here not parallel to the bounding fault system. Late Holocene geomorphic and biological indicators in the Aigio FA suggest average uplift rates of 1.6-1.9 mm×yr⁻¹ and slip rates of 1.9-2.7 mm×yr⁻¹ are proposed (Palyvos et al., 2005, 2008). Whereas both Eliki FA and Aigio FA have been linked to several large earthquakes in historical times (e.g., Pantosti et al., 2004), Psathopyrgos F has not ruptured in >300 years (Karymbalis et al., 2016a, 2016b). Farther west, the Psathopyrgos F (~8 km) has lower estimated rates of uplift of 0.7-0.8 mm×yr⁻¹ (Houghton et al., 2003).

3.1.2 Other active normal faults

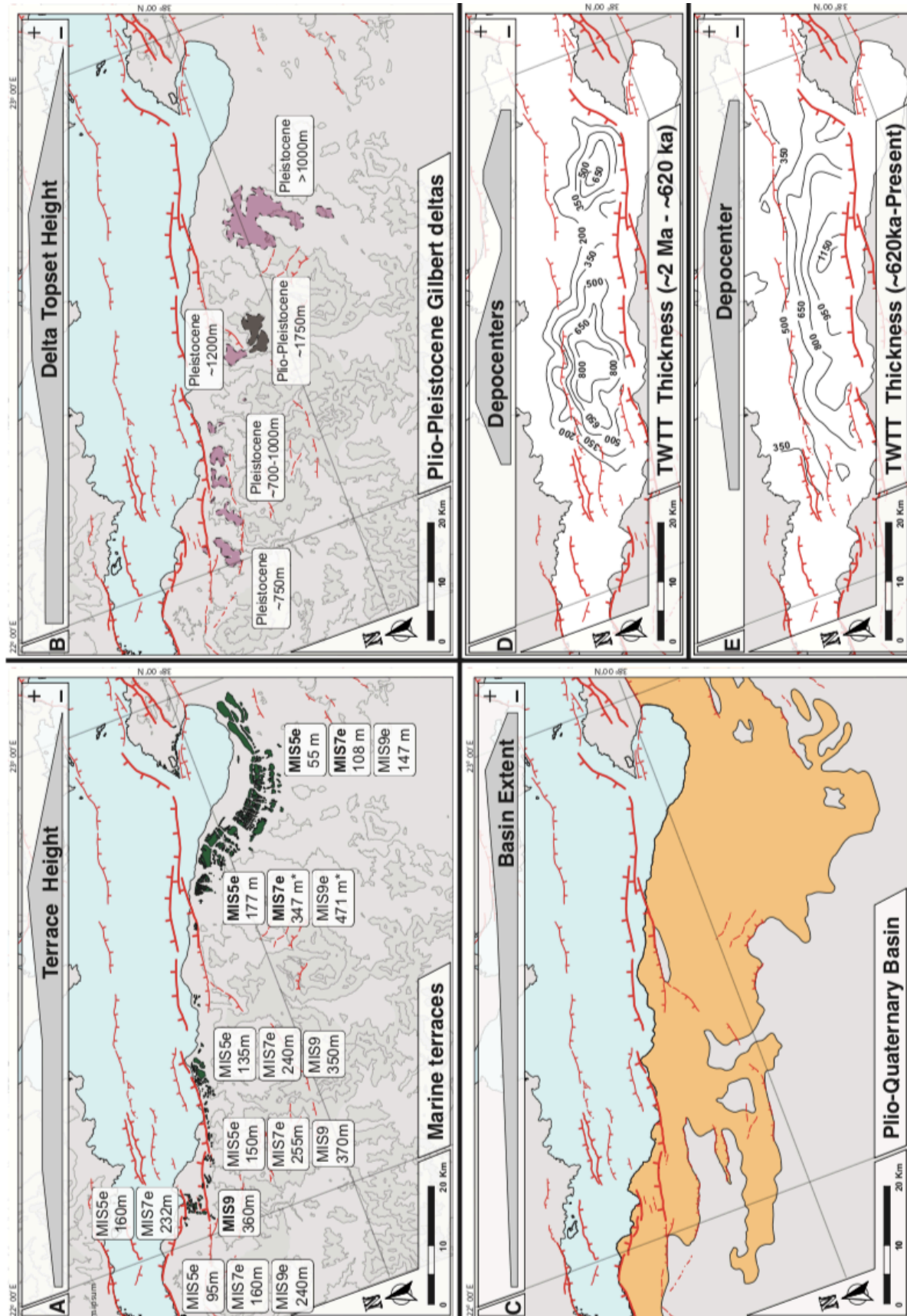
Smaller active faults are either synthetic or antithetic faults trending roughly parallel to the main fault system along most of the rift, or conjugate faults in the rift eastern and western terminus (Figs. 7 & 8). Among these faults, the system with largest offsets locates north of the bathymetric low and is composed of E-W trending faults with south dips. This fault set produces small reliefs and has no associated pattern of onshore uplift and offshore subsidence (e.g., Stefatos et al., 2002). In fact, the irregular northern coastline of the gulf (Fig. 7) is dominated by subsidence (Bell et al., 2009; Elias et al., 2009). With the exception of faults in the westernmost rift, these south-dipping faults develop minor syntectonic sedimentary wedges when compared with the bounding fault system (e.g., Nixon et al., 2016). The kinematics of bounding faults propel the activity of these faults, i.e. they act as an antithetic fault system (e.g., Stefatos et al., 2002).

The conjugate fault sets at the tips of the Corinth Rift are dissimilar to each other (Fig. 8A,-B). At the westernmost rift, E-W-trending faults with lengths of >10 km dip steeply south and have displacements and syntectonic wedges comparable to faults in the southern shoulder (e.g., Nixon et al., 2016), setting the location of part of the coastline (Fig. 8). Strain is more distributed at the easternmost rift and Perachora Peninsula, where numerous smaller faults accommodate partial motions (Fig. 8A). Fault trends range from E-W to NE-SW and NW-SE, potentially in relation to the strike of the bounding fault system, which controls their kinematics. Normal faults to the north of the rift, in the area of Itea, Antikyra and Delphi are peculiar since they trend at high angles with respect to the bounding fault system.

3.2 Uplifted Quaternary marine terraces

Sequences of uplifted marine terraces correlated to sea level highstands up to ~400 ka outcrop near the coast all along the rift-bounding fault footwall, from Alepochori to Psathopyrgos (Figs. 4, 7 & 9A). The best-developed marine terrace sequence outcrops in a ~6-8 km wide strip trending NW-SE, parallel to the gulf southern coast west of Corinth for ~40 km (Fig. 9A). This wave-cut marine terrace flight, carved into Plio-Pleistocene marls, is correlated to sea level highstands up to ~400 ka. It has large lateral variations NW-wards as distance to the master fault decreases from ~20 km to ~3 km; i.e. it increases in number of levels, from few-low lying levels in Kechrie to ~14 levels in the Onshore Xylokaastro F footwall, and in elevation by a factor of 3-4, reaching as high as ~400 m (Armijo et al., 1996; De Gelder et al., 2018) (Figs. 4, 7 & 9A). The MIS 5e terrace at ~177 m is the highest of its age for the whole gulf (Fig. 9A).

Fig. 9. Variations along the Corinth Rift axis, in map views highlighting different geologic elements. The main trend of each corresponding feature is shown schematically on top of each panel. **(A)** The presence of known marine terraces, their estimated ages and elevations at six locations - bold highstands are dated levels, and the asterisks indicate elevations extrapolated in space to match the distance to the master fault of the MIS 5e terrace. **(B)** The presence and location of mapped topsets of Gilbert deltas, their age and rough elevations. **(C)** Illustrative representations of main characteristics of river longitudinal profiles and plainviews per rift sector defined by this contribution; west (left), center (center) and east (right) rift, exaggerated 4 times in the vertical. **(D)** the extent of the Plio-Quaternary basin exposed onland. **(E)** and **(F)** are isochore maps showing two-ways travel times true vertical thickness for two seismic units, representing ~1.5-2 Ma to 620 ka, and 620 ka to Present, simplified from Nixon et al. (2016).



In the west rift, marine terraces formed by wave erosion far from the outlets of major rivers, and depositional marine terraces developed at these locations over prograding delta fans (e.g., Hemelsdaël and Ford, 2016) (Figs. 4, 7 & 9A). Up to ten levels of relatively well-developed marine terraces with laterally consistent elevations of up to ~350 m lay along the coastline in the footwalls of the West and East Eliki and Aigio faults (McNeill and Collier, 2004) (Figs. 4, 7 & 9A). The Eliki F footwall terraces show a relevant sequence in Akrata that dims westwards. They outcrop typically within 5 km of the Eliki FA trace and their elevation varies westward from 135 to 150 m for MIS 5e level and from 240 to 255 m for the MIS 7e terrace (McNeill and Collier, 2004; for their preferred ~1.1 mm×yr⁻¹ uplift rate) (Fig. 9A). Marine terraces laying between the Aigio F footwall and the hanging wall of the western sector of West Eliki F are at 160 m for MIS 5e, and 232 m for MIS 7e. Although a MIS 9 level at 360 m has been dated in the western sector of West Eliki F footwall, it is not confidently correlated laterally (De Martini et al., 2004). At the westernmost rift, seven narrow terrace levels reaching a maximum elevation of ~250 m are carved into the Plio-Pleistocene rocks of the Ps footwall, outcropping within 2 km of Ps trace, at ~90 m elevation (for MIS 5e) and ~160 m (for MIS 7e) (Houghton et al., 2003) (Figs. 4, 7 & 9A).

3.3 Modern and (perched) Plio-Pleistocene Gilbert Deltas

Two families of coarse-grained Gilbert-type deltas with similar facies associations and geometries are differently distributed along the Corinth Rift southern flank (e.g., Seger and Alexander, 2009) (Figs. 4, 7 & 9B). While Plio-Pleistocene deltas outcrop with varying angular unconformity atop of uplifted Plio-Pleistocene syn-rift and Hellenic basement rocks (e.g., Ori, 1989; Gawthorpe et al., 2017a), Holocene deltas lay in a narrow rim along the coast (Figs. 4 & 7). In the east rift, a large low laying plain passes seawards to a wide coastal platform in the absence of deltas (Figs. 4, 7 & 9B). In the rift center, prominent Plio-Pleistocene deltas display thick foresets packages (>700 m) at up to ~1750 m elevation and down-step in stranded offlapping sequences that become younger towards

the under-developed Modern deltas in the gulf shore (e.g., Rohais et al., 2007; Seger and Alexander, 2009). In the west rift, less-developed Plio-Pleistocene deltas crop out along a relatively continuous strip behind well-developed Modern deltas, which coalesce in a broad coastal delta plain (e.g., Ford et al., 2009, 2016) (Fig. 7). The swift in locus of growth of large deltaic systems from the rift center in the Plio-Pleistocene to the west in the Holocene may relate with changes in master fault activity and differential footwall uplift or changes in sediment supply.

3.4 Plio-Pleistocene (uplifted) basin extent

The extent of the exposed Plio-Pleistocene basin decreases westward along the rift southern flank strike, from an extensive area of ~35 km to a couple of strips of <10 km each (Fig. 9C). In the east rift, the Plio-Pleistocene rocks cover a large area of low relief (Figs. 7 & 9C). Towards the central rift, the uplifted syn-rift deposits are reduced to an extent of ~20 km. Similarly, the modern progradational planimetric coastal area loses extent until it is very limited or not existent between the towns of Kiato and Derveni (Karymbalis et al., 2016a, 2016b) (Fig. 7). However, in the west rift, the extent of the Plio-Pleistocene rocks presently outcropping onland is reduced in comparison to areas farther east, and outcrop in elongated WNW-ESE areas that alternate with basement rocks (Fig. 9C). Further west, the extent of the Pliocene marine basin is reduced to a stripe of several kilometers, i.e., smaller than anywhere else in the southern margin of the Corinth Rift (Fig. 9C).

3.5 Hanging wall synrift deposits

The rift basin is markedly asymmetrical and dominated by the north dipping master fault system (e.g., Brooks and Ferentinos, 1984; Stefatos et al., 2002; Taylor et al., 2011), except at the basin ends, where antithetic faults are relevant (Fig. 8) (e.g., Hubert et al., 1996; Benedetti et al., 2003; McNeill et al., 2005; Bell et al., 2008). In the west, the transition from asymmetric to roughly symmetric locates around the area where East Eliki F enters onland (e.g., Nixon et al., 2016), and a

less asymmetric structure is recognized in the eastern end of the rift basin (Sakellariou et al., 2007).

A rift-scale unconformity with an estimated age of ~620 ka, bounds two units with distinct seismic character that mark a change in setting from lacustrine to mixed marine/lacustrine; a unit with non-coherent reflectors below the unconformity, and a unit with rhythmical alternations of low-/high-amplitude reflectors above it (Sachpazi et al., 2003; Lykousis et al., 2007; Sakellariou et al., 2007; Bell et al., 2008, 2009; Taylor et al., 2011; McNeill et al., 2018). Synrift depocenters traced for both units (Fig. 9 in Nixon et al., 2016) mark a swift from a complex rift zone with distributed depocenters (Fig. 9D) to a markedly asymmetrical rift (Fig. 9E). This switch towards the present asymmetric rift may have taken place by establishment of the north dipping faults by ~620 ka and their later linkage by ~340 ka (Nixon et al., 2016). The upper unit is laterally continuous along the rift, with two exceptions; a second unconformity (~340 ka) exists in the west, and only the upper part of the sequence can be traced in the Alkyonides Gulf (e.g., Bell et al., 2008, 2009).

4 Bounding fault topobathymetry, river catchments and footwall relief

4.1 Topobathymetry

We use stacked swaths to characterize the morphology of the Corinth Rift in relation to its current bounding fault system (Figs. 10 & 11). Each of the three stacked swath profiles showing the morphology across the central and west rift (Fig. 10) runs from the southern shoulder drainage divide to the northern margin coast. These stacked swaths look westwards perpendicular to the strike of particular fault segments (Fig. 4 for reference), i.e. Central Rift FA, Eliki FA, and Aigio FA (A, B & C in Fig. 10). Each of the three stacked swath profiles providing a view along the rift southern shoulder (Fig. 11) extends from Loutraki to Psathopyrgos looking towards the fault front roughly to the SSW (Fig. 4 for reference). The stacked swath profiles cover the topography of the entire drainage divide, that ~21 km of the bounding fault (see section 2.2.1 & 2.2.2), and the

bathymetry until further north than the deepest basin floor (A, B and C in Fig. 11).

4.1.1 Across the bounding fault

Topographic variations in the rift central sector are the largest for both the maximum and minimum topographic envelopes (red and blue in Fig. 10A). The central rift has the highest mean elevations, the highest summit (Killini, 2376 m) and the exposure of the former basin at the highest location (Mavro, 1756 m). In the south, flat-laying and gently south-dipping endorheic basins (Feneos, Stymfalia y Skotini plains; Figs. 4 & 7) remain overall at similar mean elevations for horizontal distances of ~40 km. In this area, maximum and minimum topography show similar mean elevations (of ~1650 m and of ~650 m, respectively) for similar horizontal distances (Fig. 10A). The northward decreasing relief contains Gilbert delta topsets at ~1100-1200 m (Evrostini) and ~900-1000 m (Klimenti) (Figs. 4 & 7) and reaches in 10-15 km bathymetric depths in excess of -800 m, as close as 2 km from the shore (Fig. 10A). This represents a relief change of ~2.5 km in <15 km in the horizontal, or >3 km in <25 km, measured from the rift highest topography to its lowest bathymetry, i.e. a slope of ~9.5° or ~7°, respectively. Northwards, the flat basin floor lays at approx. -850 m for ~10 km and the gulf is the widest at sea level. The envelope of maximum relief in the northern shoulder rises from -750 m to ~1000 m in a rounded convex-up shape (Fig. 10A).

Topographic variations in the west rift are relevant in short horizontal distances, as marked by the maximum and minimum topography envelopes (Fig. 10B). The west rift contains the second highest summit (Aroania, 2341 m) and a northward decreasing topography with Gilbert delta topsets of Mid-Late Pleistocene age <5 km from the master fault at ~700-1000 m. Rivers with flat upstream reaches and steep lower reaches set the minimum topography and feed large modern Gilbert-type deltas (Fig. 10B). A flat wide bathymetry at -750 m in the east changes westward to a narrower rugged bathymetry at shallower depths (approx. -375 m), a change that occurs in both basin margins, not only in relation to deltas. The maximum topography envelope in the northern

shoulder has a concave-up profile not paralleled by the minimum topography envelope (Fig. 10B).

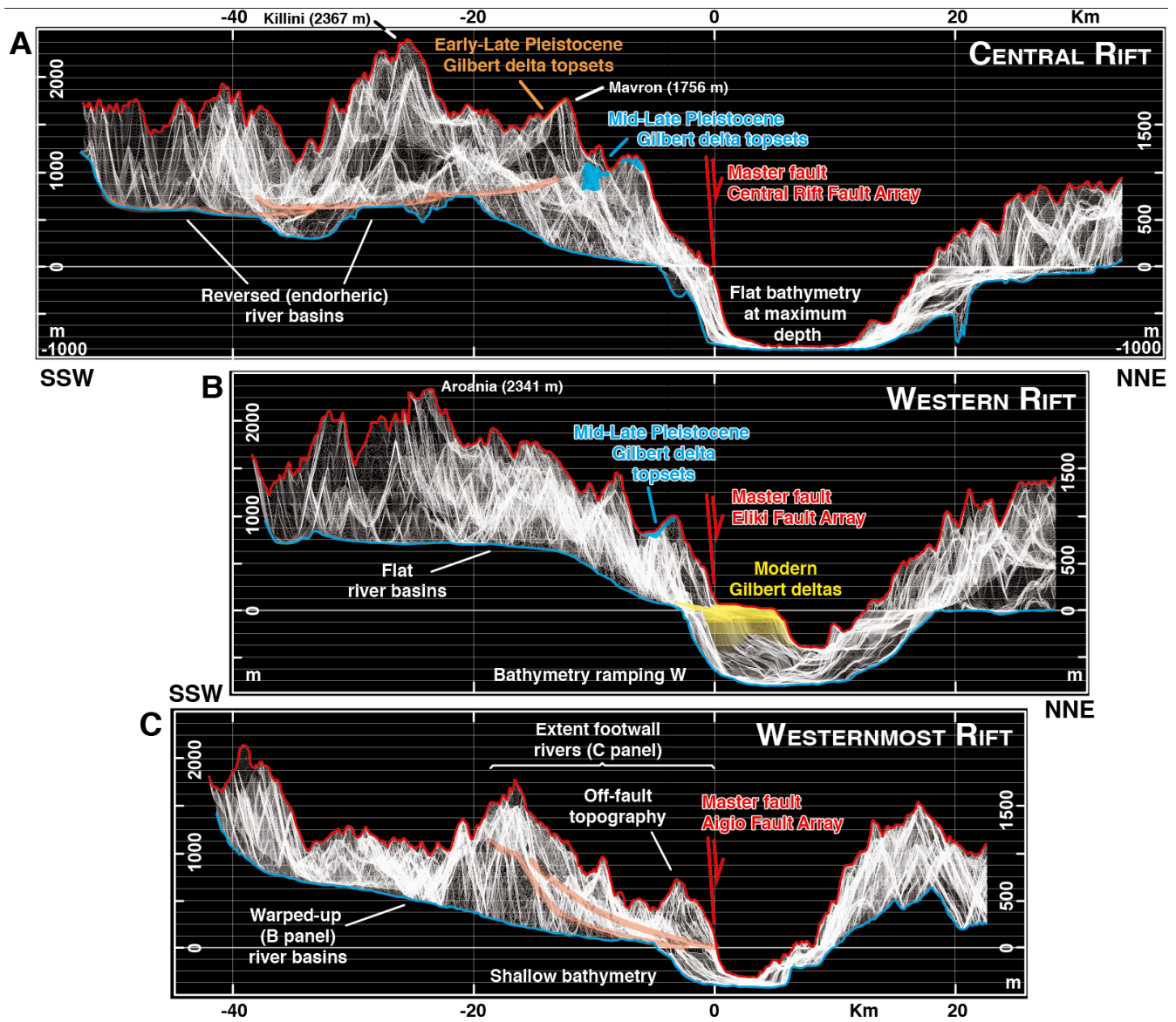


Fig. 10. Topobathymetry across the southern shoulder of the Corinth Rift in three “views” perpendicular to the current rift-bounding fault. Each ~26 km wide swath is composed of 400 swath profiles, stacked over a projection line perpendicular to the average strike of the main fault in each sector (see below). The width of each individual swath is calculated dynamically and of ~75 m. Relief is exaggerated ~8 times. Distance along each wide swath is measured from the master fault (positive northwards). **(A)** Topobathymetry associated with the Central Rift FA in a view looking towards N295°E. **(B)** Topobathymetry associated with the Eiki FA as seen looking in a N290°E direction. **(C)** Topobathymetry associated with the Aigio FA in a view looking towards N290°E. In all views the upper envelope (red line) and the lower envelope (blue line) represent the maximum and minimum topobathymetry, respectively. Each individual sector of the master fault is shown with a 55° north dip in red. Other associated features are shown: rivers and endorheic basins (dim red); topsets of Gilbert deltas in light brown (Late Pliocene - Early Pleistocene), blue (Mid-Late Pleistocene); and yellow for modern Gilbert Deltas.

The westernmost rift has the lowest variations in topography (Fig. 10C). It has two differentiated areas in its southern shoulder, each bounded south by a maximum in topography. In the area close to the master fault, a steep maximum relief envelope decays monotonically from the footwall river headwaters, except for a topographic high in its westernmost end (“off-fault topography” in Fig. 10C). The area farther away from the master fault has a minimum topography envelope in relation to longer rivers. The rift is here the narrowest and shallowest, with a width of ~8 km at sea level and a basin floor laying between -250 m and -350 m (Fig. 10C). The maximum and the minimum topographic envelopes in the northern margin have a sharp triangular shape increase with its maximum ~15 km north of the coast.

4.2.2 Along the bounding fault

Maximum drainage topography has variable along-strike average elevations of ~750 m in the east, ~2000 m in the center and ~1600 m in the west (Fig. 11A). The maximum relief within ~21 km of the rift-bounding fault (Fig. 11B) similarly varies along-strike at heights ~70-80 % of those in the maximum drainage topography (Fig. 11A). Both profiles significantly increase in elevation between the east and central rift while only the maximum drainage topography decreases markedly west of Aroania summit (~2341 m) (Figs. 7, 8 & 11). Bathymetric depths show a sharp transition in the east, from depths of ~150 m to >800 m. Similar bathymetric depths are maintained westwards for ~40 km, and then decrease gently to <250 m in ~40 km (Fig. 11C).

River drainages and triangular facets stand out in the stack swaths of southern margin of the Corinth Rift (Fig. 11). River drainages (dimmed red lines; Fig. 11A) show significant differences along the main rift shoulder strike. Low laying drainages in the east exist at elevations below ~300 m. Flat concave-up drainages in the center lay at elevations between ~700 m and ~800 m in relation to the endorheic plains. Catchments farther west have similar morphologies decaying in elevation to ~600 m and tilting lightly to the east (Fig. 11A). Well-developed triangular facets in the

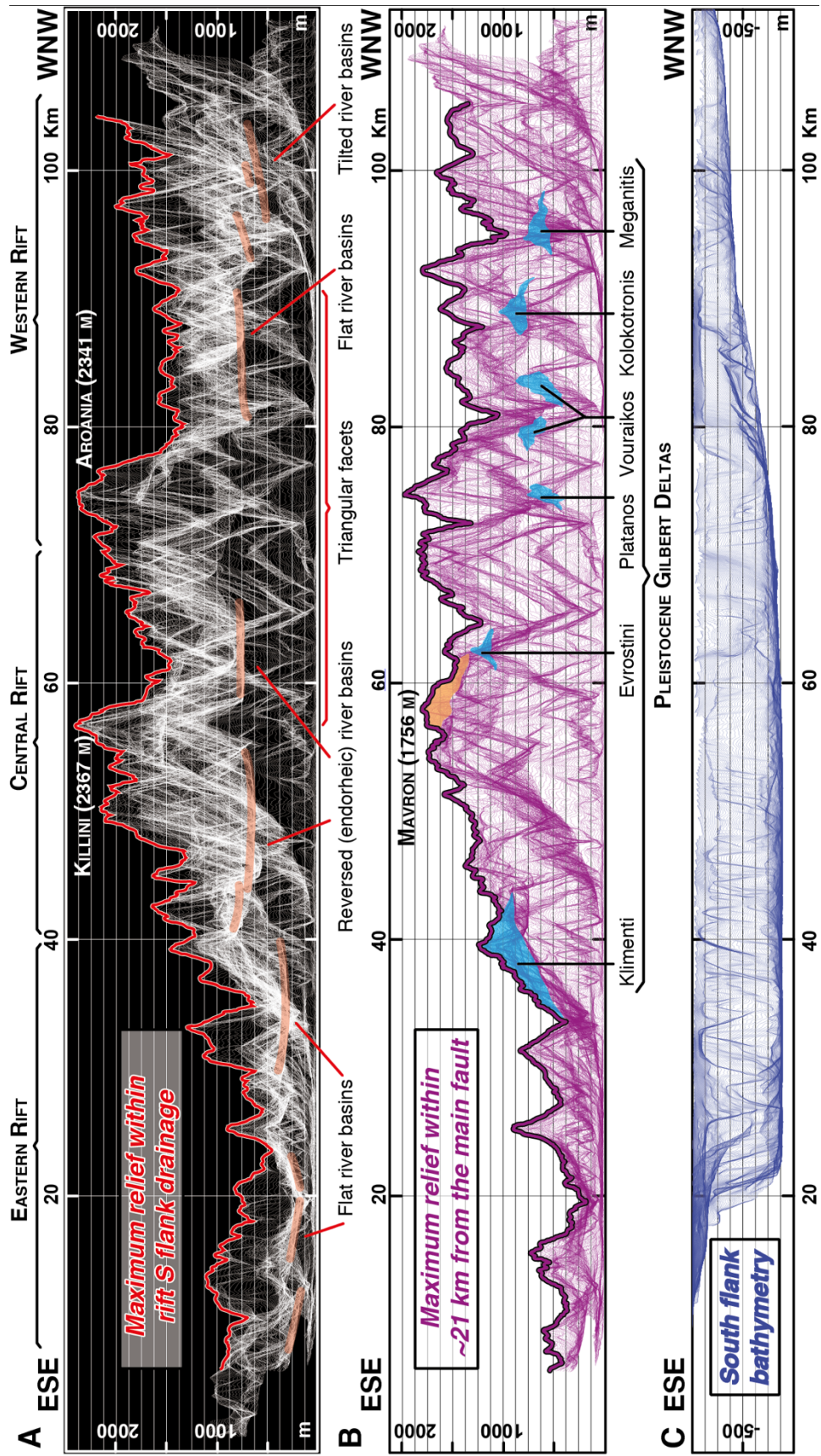


Fig. 11. Stacked swath profiles of topography and bathymetry along the southern flank of the Corinth Rift in a view parallel to the master fault. The “view” is looking SSW, with a projection line N105°E, defined to represent the average strike of the master fault. Plotted profiles are exaggerated ~8 times. Relief in A and B panels is defined by 500 stacked swath profiles of estimated width ~90 m, on a 20m-resolution DEM. **(A)** Maximum relief within the rift flank drainage is obtained clipping the DEM to the extent of the river networks draining the southern coast of the Gulf of Corinth, including the endorheic river basins; and **(B)** Maximum relief within ~21 km from the fault is obtained clipping the DEM at ~21 km from the main fault and aims to approximate to the relief related to the bounding fault system. In these panels, no bathymetric data is used and there is no correction on the basis of master fault position, i.e. plotted relief is a good approximation to footwall relief only in the area where the fault is at or near sea level (from Akrata eastwards for ~7 km, Fig. 6). The envelope of highest elevations of onshore topography is also used in Fig. 10. River basins are marked in red in panel A, and the topsets of Gilbert delta are marked in blue (Mid-Late Pleistocene) and light brown (Calabrian) in panel B). **(C)** Bathymetry from north of the lower bathymetry axis to the south coast of the gulf, as seen by 500 stacked swaths profiles in a 50-m resolution bathymetry.

center and west rift occur in four hierarchical levels and often have a perched Gilbert deltas laying at their triangular facets “tips” (Fig. 11B). The oldest Gilbert delta of the rift, Mavro (Figs. 4 & 7) outcrops at the highest fault-related relief (~1756 m) in relation to the highest set of triangular facets, with triangle tips at ~1600-1750 m (purple line; Fig. 11B). Gilbert delta topsets of younger age, Klimenti and Evrostini outcrop to the sides of Mavro at heights coincident with the second highest tips of the triangular facets (at ~1000-1200 m). Gilbert deltas to the west (Platanos, Vouraikos, Kolokotronis and Meganitis) (Figs. 4 & 7) lay on top of triangular facets with tips at ~850-950 m (Fig. 11B). A fourth set of triangular facets, with tips at ~500 m elevation, is seen only in the center of the margin (Fig. 11B). Aforementioned first-order variations along the rift axis may result from changes in rift maturity derived from a bounding fault that is decreasing in slip rates and/or younger westwards, which may relate with location and extent of the rift geologic features.

4.2 Footwall river profiles and tectonic knickpoints

We analyse the river profile geometry of the 16 largest river catchments draining the southern shoulder of the rift, and picked tectonic knickpoints in their trunks (see section 2.2.4, Fig. 12 & Table 1). River longitudinal profiles of footwall catchments vary consistently along the southern rift shoulder strike as a function of distance from, and slip rate along, the master fault system (Fernández-Blanco et al., 2019b). As a first approximation, these departures are readable by

comparison to theoretical smooth graded profiles with uniform erodibility and rock uplift (dashed orange in Fig. 12A).

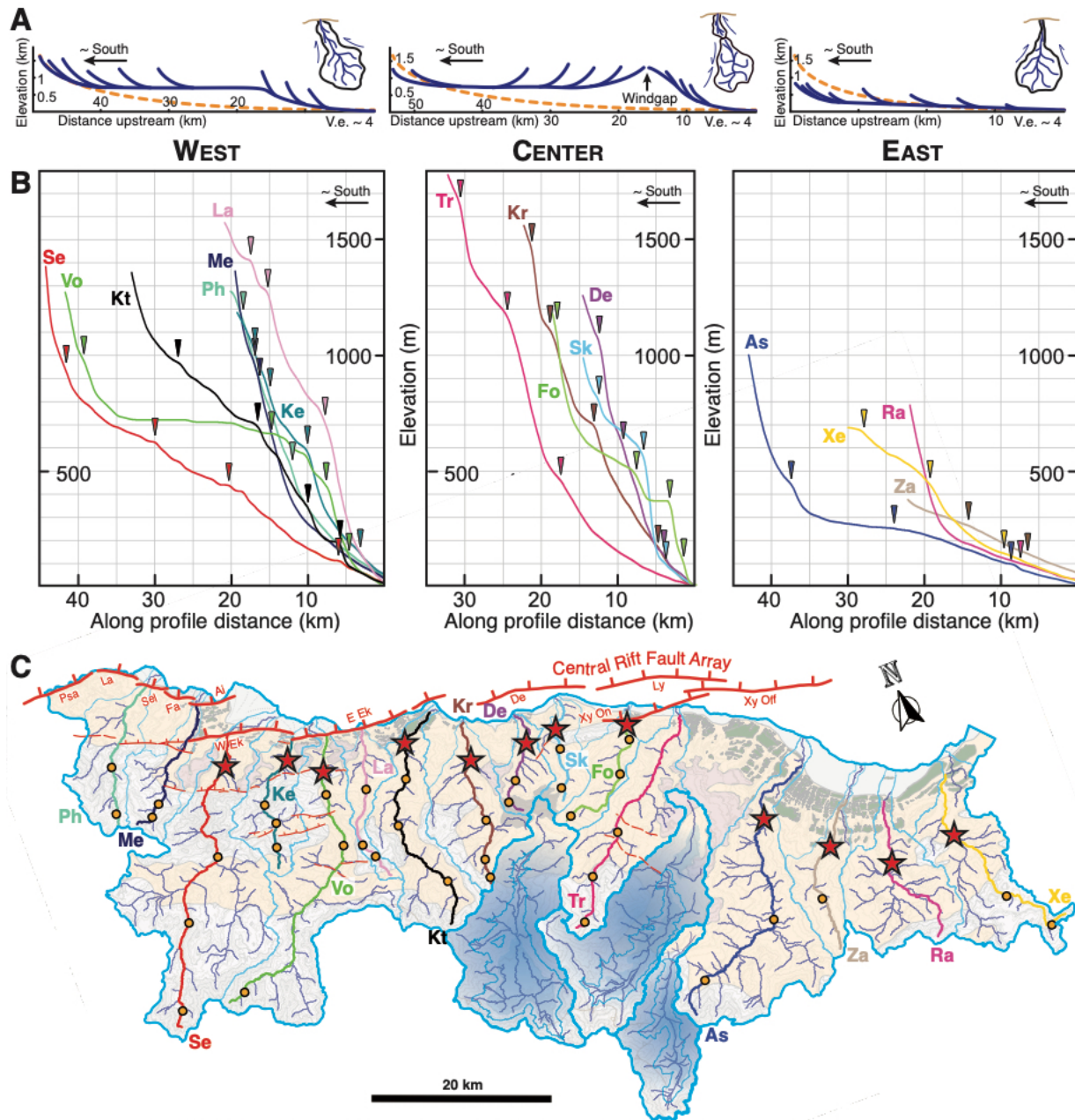


Fig. 12. Sixteen largest river catchments in the southern shoulder of the Corinth Rift and tectonic knickpoints of their trunks. **(A)** Main tectonic knickpoints of the trunks of the sixteen largest river catchments of the southern shoulder of the Corinth Rift in longitudinal profile view, grouped per rift sector. East: (Xe) Xerias, (Ra) Raizanis, (Za) Zapantis and (As) Asopos; Center: (Tr) Trikalitikos, (Fo) Fonissa, (Sk) Skoupeiko, (De) Dervenios and (Kr) Krios; West: (Kt) Krathis, (La) Ladopotamos, (Vo) Vouraikos, (Ke) Kerinitis, (Se) Selinous, (Me) Meganitis and (Fi) Finikas. **(B)** Location of tectonic knickpoints in map view. For this analysis we also used slope-area and χ plots (see supplementary in Fernández-Blanco et al., 2018). The stars mark the lower set of tectonic knickpoints seen in most river trunks at low elevations.

In the east rift, river longitudinal profiles are flat (<300 m elevation in upstream distances of >15 km) and show broad up-convexities (Fig. 12A, right). In the east rift, all trunks show a knickpoint laying at low elevations (100-200 m) (Fig. 12B & Table 1), and a variable number of knickpoints with heights that seem to lay at three elevations (two at ~275 m, two at ~450 m and one at ~700 m).

In the central rift, the shortest and steepest longitudinal profiles (>1 km elevation in <15 km) flow towards the gulf at the front of wind-gaps bounding large endorheic plains related to reversed river catchments. Central rift exorheic and endorheic catchments, taken together, show the largest divergence from theoretical profiles in steady-state (Fig. 12A, center). In the central rift, each river has either three or four tectonic knickpoints, and there are three families at different heights (Fig. 12B & Table 1). Again, a set of knickpoints lay at elevations of 100-200 m for all but Trikalitikos R, which is the largest network. The other two sets of tectonic knickpoints lay between ~1100 m and ~1200 m (Trikalitikos, Fonissa, Dervenios, Krios), and at ~1500 m and ~1700 m for the two river networks that reach that elevation (Trikalitikos, Krios) (Fig. 12B, Table 1). In between these knickpoints, their height is more distributed, but another set can be seen gaining elevation from east (500 m at Trikaitikos R) to west (700 m at Krios R) (Fig. 12B). Fonissa R has another tectonic knickpoint at ~375 m and Skoupeiko R at ~825 m.

In the west rift, rivers alternate long (≥ 35 km) and short (<15 km) longitudinal profiles except for the westernmost footwall river catchments. Short rivers catchments compare with the steep profiles of the central rift. Long rivers have morphologies with up-convexities departing from an inferred steady state profile geometry (Fig. 12A, left) and declining in steepness westwards (see Fernandez-Blanco et al, 2019b for details). In the west rift, we differentiate two areas. Rivers transecting the Eliki FA have four tectonic knickpoints, except Ladopotamos R, with three (Fig. 12B, Table 1). With the exception of the latter, one set of knickpoints lies again at elevations between

100 m and 200 m. Tectonic knickpoints of the other three families lay at lower elevations for the longer trunks (Krathis, Vouraikos, Selenous) and at higher elevations for the shorter trunks (Ladopotamos, Kerinitis). Footwall rivers associated with the Aigio FA (Meganitis, Finikas) present two knickpoints each and none correspond to the low elevation knickpoints observed elsewhere in the southern rift flank (Fig 12B, Table 1). Contrarily, the uppermost set of tectonic knickpoints in both rivers is at a similar position than the set of tectonic knickpoints at highest elevations in all trunks eastwards.

Most trunks show four tectonic knickpoints that ought to result from tectonic perturbations that occurred during the growth of the bounding fault of the southern shoulder of the Corinth Rift (see section 2.2.3). At last of those perturbations affected the entire fault system, perhaps with the exception of the westernmost rift (Aigio FA).

4.3 Footwall relief

We calculated the envelope of footwall relief projecting 20-m resolution DEM data perpendicularly towards the bounding fault along its strike (see section 2.2.2). For the west rift, where the trace of the bounding faults can be mapped with confidence and errors are minimal, we calculated three trends in footwall relief, corresponding to the three different strikes of their respective fault arrays (Fig. 13; East Eliki in red, N275°E; West Eliki in blue, N285°E; Aigio in green, N300°E). We then used N285°E to calculate the footwall relief over the entire southern shoulder (Fig. 14).

4.3.1 West rift

The Eliki FA footwall relief shows a broad (~7 km) maximum at ~1900 m in the east, and decays towards the west to a minimum value of ~600 m. Between both ends, there are three local maxima (at ~1900m, ~1500 m and ~1000 m) and four local minima in footwall relief that seem to correlate with the extent of different fault sectors (Figs. 4, 7 & 13), i.e., local maxima roughly coincide with

the center of East Eliki (undifferentiated from the East Offshore Eliki), West Eliki and Westernmost Eliki faults, respectively, and local minima sets between each of these faults segments (Fig. 13). Local minima sets at specific horizontal distances below each local maxima, i.e. ~400 m eastwards and ~800 m westwards, suggesting a constant decline in footwall relief to the west (Fig. 13). However, minima in the eastern and western tips of Westmost Eliki F are an exception, laying both at similar elevations (~600 m below their local maximum).

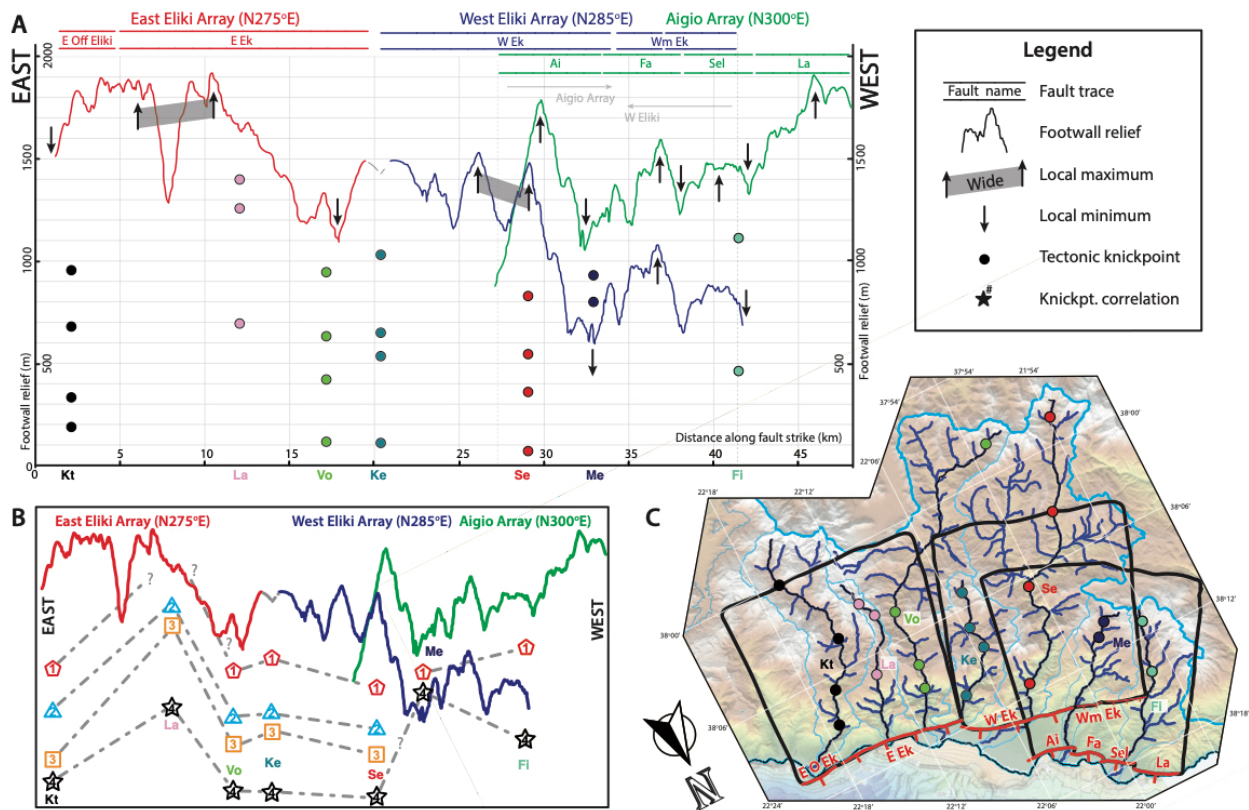


Fig. 13. (A) Footwall relief associated with the Eliki FA and Aigio FA, and heights of the tectonic knickpoints of river trunks intersecting them. The strike of each fault array was simplified for their whole length as N275°E for East Eliki F, N285°E for West Eliki F and N300°E for Aigio FA. Both footwall relief and knickpoint heights are measured vertically in relation to their active faults. Footwall relief is shown in different colours for each correlatable fault array. Tectonic knickpoint heights of Krathis (Kt), Ladopotamos (La), Vouraikos (Vo), Kerinitis (Ke), Selinous (Se), Meganitis (Me) and Finikas (Ph) rivers are projected perpendicularly to the strike of Eliki FA and Aigio FA at the point where the river crosses the fault. To avoid duplicity in the overlapping area between West Eliki Array and Aigio FA, tectonic knickpoints are plotted only as “seen” by the Aigio FA. **(B)** Tectonic knickpoints lateral correlation as per analogous tectonic perturbation in the main fault. **(C)** Map view, shown with north pointing down. Thick black boxes in the footwall of each fault segment mark the extent of the DEM areas used for the projection of the topographic swaths. Tectonic knickpoints, with coloring in agreement with panel (A), belong to the trunks (in black) of the river networks (in blue) that run through the active faults (in red).

| River | # | KP # | X coord | Y coord | Abs. Elevat. (m) | Smooth Abs. Elvt. (m) | Elevat. from fault (m) | Drainage area (km ²) | Distance fault (m) | Distance divide (m) | Chi |
|--------------|----|------|---------|---------|------------------|-----------------------|------------------------|----------------------------------|--------------------|---------------------|-----------|
| Xerias | 1 | 1 | 666526 | 4191780 | 138 | 140 | Underwater | 110.2144 | 8543 | 23678 | 1.924745 |
| Xerias | 1 | 2 | 669726 | 4183420 | 460 | 465 | Underwater | 26.7408 | 19860 | 12361 | 6.268060 |
| Xerias | 1 | 3 | 673346 | 4178620 | 664 | 665 | Underwater | 2.7896 | 28123 | 4098 | 11.672004 |
| Raizanis | 2 | 1 | 658866 | 4191600 | 113 | 114 | Underwater | 115.8364 | 7680 | 16283 | 1.728496 |
| Zapantis | 3 | 1 | 653046 | 4195520 | 143 | 144 | Underwater | 54.6592 | 12156 | 17621 | 3.718770 |
| Zapantis | 3 | 2 | 650286 | 4190380 | 267 | 265 | Underwater | 19.214 | 14495 | 9658 | 5.167287 |
| Assopos | 4 | 1 | 647446 | 4200840 | 124 | 122 | Underwater | 246.9484 | 9839 | 35027 | 1.616133 |
| Assopos | 4 | 2 | 644386 | 4190120 | 266 | 265 | Underwater | 162.4516 | 24165 | 20701 | 4.221977 |
| Assopos | 4 | 3 | 634766 | 4186440 | 464 | 454 | Underwater | 15.4148 | 37689 | 7177 | 8.628353 |
| Trikalitikos | 5 | 1 | 631426 | 4205420 | 480 | 478 | Underwater | 66.6064 | 17937 | 16608 | 4.265542 |
| Trikalitikos | 5 | 2 | 627066 | 4201740 | 1180 | 1175 | Underwater | 25.022 | 24769 | 9776 | 6.856264 |
| Trikalitikos | 5 | 3 | 624446 | 4197280 | 1644 | 1641 | Underwater | 4.428 | 30843 | 3703 | 10.932628 |
| Fonissa | 6 | 1 | 636386 | 4216360 | 122 | 113 | Underwater | 50.3056 | 1700 | 19260 | 0.573023 |
| Fonissa | 6 | 2 | 636286 | 4214680 | 381 | 368 | Underwater | 46.5236 | 3554 | 17406 | 1.217854 |
| Fonissa | 6 | 3 | 633966 | 4211420 | 515 | 514 | Underwater | 26.3052 | 8510 | 12450 | 3.253888 |
| Fonissa | 6 | 4 | 627146 | 4208960 | 1101 | 1084 | Underwater | 1.7648 | 18240 | 2720 | 10.176852 |
| Skoupeiko | 7 | 1 | 628725 | 4218520 | 121 | 121 | Underwater | 34.6452 | 5956 | 12975 | 2.221048 |
| Skoupeiko | 7 | 2 | 628666 | 4216420 | 575 | 576 | Underwater | 25.2004 | 7047 | 10264 | 2.857482 |
| Skoupeiko | 7 | 3 | 627266 | 4212280 | 832 | 810 | Underwater | 8.0304 | 12808 | 4503 | 6.169165 |
| Devrenios | 8 | 1 | 625506 | 4218500 | 162 | 148 | Underwater | 35.224 | 4250 | 12744 | 1.637598 |
| Devrenios | 8 | 2 | 622726 | 4214860 | 623 | 613 | Underwater | 7.5708 | 9593 | 7401 | 4.289638 |
| Devrenios | 8 | 3 | 621186 | 4212840 | 1066 | 1054 | Underwater | 4.0536 | 12694 | 4299 | 7.122171 |
| Krios | 9 | 1 | 618606 | 4218760 | 195 | 185 | Underwater | 93.7536 | 5021 | 19608 | 1.220103 |
| Krios | 9 | 2 | 618086 | 4211840 | 714 | 707 | Underwater | 47.8124 | 13471 | 11158 | 3.759270 |
| Krios | 9 | 3 | 616446 | 4207780 | 1120 | 1116 | Underwater | 7.2472 | 19170 | 5459 | 6.981231 |
| Krios | 9 | 4 | 616286 | 4205700 | 1473 | 1463 | Underwater | 1.4496 | 21600 | 3029 | 10.100120 |
| Kratis | 10 | 1 | 612526 | 4222760 | 199 | 174 | 184 | 133.5284 | 5525 | 28997 | 1.194022 |
| Kratis | 10 | 2 | 611286 | 4219320 | 351 | 345 | 336 | 120.7608 | 9875 | 24648 | 2.180448 |
| Kratis | 10 | 3 | 608666 | 4214720 | 695 | 694 | 680 | 84.5236 | 16452 | 18071 | 3.842688 |
| Kratis | 10 | 4 | 611666 | 4206960 | 970 | 970 | 955 | 24.9636 | 26851 | 7672 | 7.331195 |
| Ladopotamos | 11 | 1 | 606706 | 4219800 | 708 | 706 | 693 | 19.0396 | 7607 | 15012 | 3.244866 |
| Ladopotamos | 11 | 2 | 604166 | 4214100 | 1274 | 1264 | 1259 | 8.4976 | 15110 | 7509 | 8.007839 |
| Ladopotamos | 11 | 3 | 605066 | 4212400 | 1411 | 1405 | 1396 | 5.676 | 17350 | 5269 | 9.856060 |
| Vouraikos | 12 | 1 | 602826 | 4223300 | 138 | 149 | 108 | 213.2052 | 4499 | 38531 | 0.773081 |
| Vouraikos | 12 | 2 | 602306 | 4220820 | 447 | 442 | 417 | 206.7072 | 7480 | 35550 | 1.307397 |
| Vouraikos | 12 | 3 | 602126 | 4214800 | 661 | 661 | 631 | 181.276 | 14559 | 28471 | 2.629612 |
| Vouraikos | 12 | 4 | 585986 | 4203300 | 975 | 968 | 945 | 7.2736 | 39183 | 3847 | 11.039972 |
| Kerinitis | 13 | 1 | 599366 | 4225820 | 161 | 158 | 111 | 69.9096 | 2785 | 17674 | 0.788818 |
| Kerinitis | 13 | 2 | 595446 | 4222140 | 581 | 585 | 531 | 46.256 | 9971 | 10835 | 3.080262 |
| Kerinitis | 13 | 3 | 595786 | 4219680 | 693 | 695 | 643 | 14.564 | 12564 | 7895 | 4.278960 |
| Kerinitis | 13 | 4 | 594986 | 4217560 | 914 | 911 | 864 | 8.9888 | 15241 | 5217 | 6.099830 |
| Sellinous | 14 | 1 | 592866 | 4227640 | 146 | 145 | 66 | 295.148 | 5892 | 40143 | 0.884287 |
| Sellinous | 14 | 2 | 588486 | 4218540 | 439 | 438 | 359 | 242.3104 | 19731 | 26304 | 3.107405 |
| Sellinous | 14 | 3 | 582866 | 4212760 | 622 | 621 | 542 | 51.9428 | 29859 | 16176 | 5.767960 |
| Sellinous | 14 | 4 | 578746 | 4203780 | 908 | 907 | 828 | 10.0236 | 41463 | 4572 | 10.910468 |
| Meganitis | 15 | 1 | 584247 | 4226074 | 853 | 848 | 803 | 8.1643 | 18527 | 5662 | 7.073409 |
| Meganitis | 15 | 2 | 583166 | 4225300 | 970 | 955 | 930 | 6.116 | 16733 | 4516 | 7.361968 |
| Phoenix | 16 | 1 | 580866 | 4232120 | 511 | 508 | 461 | 31.8224 | 11964 | 10382 | 3.927337 |
| Phoenix | 16 | 2 | 579506 | 4227040 | 1162 | 1153 | 1112 | 5.0552 | 18342 | 4005 | 8.081930 |

Table 1. Data associated with the tectonic kickpoints identified in the trunks of the 16 river networks analysed in this study.

The overall trend of Aigio FA footwall relief has a minimum at ~900 m in the east, and a maximum at ~1900 m in the west. The extent of the four single fault segments coincide with distinctive individual footwall relief “up-pointing triangles” (with a minimum at each tip and a maximum at their center) (Figs. 4, 7 & 13). The overall trend is clear in the minima observed, laying roughly every ~7 km, and whose heights are ~900 m (to the east of Aigio F), ~1100 m (between Aigio and Fasouleika faults), ~1200 m (between Fasouleika and Selianitika) and ~1300 m (between Selianitika and Lambrini). The trend observed in the maxima is more complex, with the east Aigio F showing a maximum of ~1800 m, only ~100 m lower than the displacement maxima at the center of Lambrini F, in the west (Fig. 13). In between, footwall relief rises west more gently than the observed overall trend in mean topography (~200 m height difference in ~10 km along strike in an overall trend of ~700 m in ~20 km) (Fig. 13).

The footwall relief patterns of both Eliki FA and Aigio FA can be attributed to individual growth of fault segments and subsequent link into a larger fault systems (see details in sections 2.2.2 & 5.1.1). The east rising trend in footwall relief in the Eliki FA suggest that it behaves as the western termination of a larger fault and the plateau in footwall relief plateau in the area of overlap between Eliki and Aigio fault arrays points to recent linkage between both fault systems.

4.3.2 Rift southern shoulder

Footwall relief has a wavelength that correlates with the rift southern shoulder, with a maximum in vertical displacement around its center and minima at both ends, although its trend cannot be accurately resolved the eastern sector (see section 2.2.2). Several sets of up-pointing triangles contained in successively larger triangles exhibit similar morphologies in footwall relief at smaller scales, within the parabolic trend at rift-margin scale. Most first-order triangular morphologies can be tracked with confidence to their respective faults, with maximum around the centre of each fault segment and two minima at its tips (cf. Fig. 14A & 14B). For example, the individual up-pointing

triangle that marks the footwall relief maximum at margin scale is above, and has similar lateral extent than, the Derveni F trace, overlapping with the West Onshore Xylokastro F trace (Fig. 14). The maximum in footwall relief is ~12 km in wavelength and in turn compounded by three individual up-pointing triangles. The parabolic geometry of the footwall relief indicates that the active fault system behaves as a single fault at depth, and the different hierarchies of up-pointing triangles suggest that the fault grew by along strike linkage of smaller faults (sections 2.2.2 & 5.1.2).

5 Fault growth and relief response in the rift southern shoulder

We built from our data, premises of normal fault mechanics, and other constraints in the frame of our proposed theoretical framework (Fig. 6) to explore the evolution of the rift-forming fault, and that of the southern flank and Corinth Rift itself.

5.1 Growth and propagation sequence

We plot tectonic knickpoints of footwall catchment trunks together with footwall relief to explore their mutual relation and their relationship with the bounding fault (Figs. 13 & 14). We project, orthogonal to fault strike at the point where the river crosses the fault, the height of tectonic knickpoints, measured vertically from the fault they cross. Tectonic knickpoints belong not only to the 16 largest river trunks draining the gulf but also to the two largest trunks of Olvios and Safenetos (Fig. 14 & Table 1). We tentatively correlate tectonic knickpoints across fault strike. We base our correlation on cross-causality, not cross-coevality, i.e. the same number represents an equivalent (interpreted) type of tectonic perturbation in the bounding fault (fault initiation, fault linkage, fault slip rate increase), and not a similar time of occurrence. This correlation, aiming at reconstructing the main tectonic perturbations of the master fault since its formation, oughts to account for the few relevant considerations detailed below.

Reverse drainages in the central rift were footwall river networks that drained north and eventually disconnected from their original outlet, probably <1 Ma. Tectonic knickpoints in the (now) endorheic river basins record tectonic perturbations in the main fault until the moment of inversion, and are thus relevant to understand the growth and evolution of the bounding fault(s). These tectonic knickpoints probably archive a longer “recording period” than other drainages (see Fernández-Blanco et al., 2019b). The two knickpoints in both reversed basins are at similar elevations of ~1200 m and ~1400 m but the windgaps related to the disconnection of these basins are carved in topsets of Gilbert-type deltas of different ages and at different elevations. The highest windgap is at ~1300 m in the Late Pliocene-Early Pleistocene Mavro Delta, and the lowest windgap is at ~850 m, carved in rocks of the Klimenti Delta, with an approximate age of Middle-Upper Pleistocene (e.g., Ford et al., 2016).

5.1.1 West rift

We recognised four groups of tectonic knickpoints in the west rift, that show marked differences between Eliki FA and Aigio FA (groups 1 to 4 in Fig. 13B). In the Eliki FA, the sets of tectonic knickpoints at highest positions (groups 1, 2 & 3 in Fig. 13B) correlate with footwall relief, laying at higher and lower elevations in footwall relief maxima and minima, respectively. This leads to triangular patterns (grey dashed lines in Fig. 13B) for these three sets that roughly mimic footwall relief trends. The correlation is less clear for tectonic knickpoints at lower and western positions, and absent for the lower set of tectonic knickpoints (group 4 in Fig. 13B). This lower knickpoint set shows instead an apparent trend towards lower elevations at westward positions (Fig. 13 & Table 1). The highest tectonic knickpoints in the river trunks transecting the Aigio FA rivers (group 1 of Meganitis and Finikas in Fig. 13B) seem to be related to those at the highest positions in eastward trunks, as observed from their close location to the drainage divide for each river (Table 1). The relative high elevation of the tectonic knickpoint set at low elevations in Meganitis and Finikas trunks may indicate that they developed in relation to recent fault linkage (see theoretical

framework, section 2.2.3, and Fig. 6), and we have tentatively correlate them with the set at ~100-200 m farther east (group 4 in Fig. 13B).

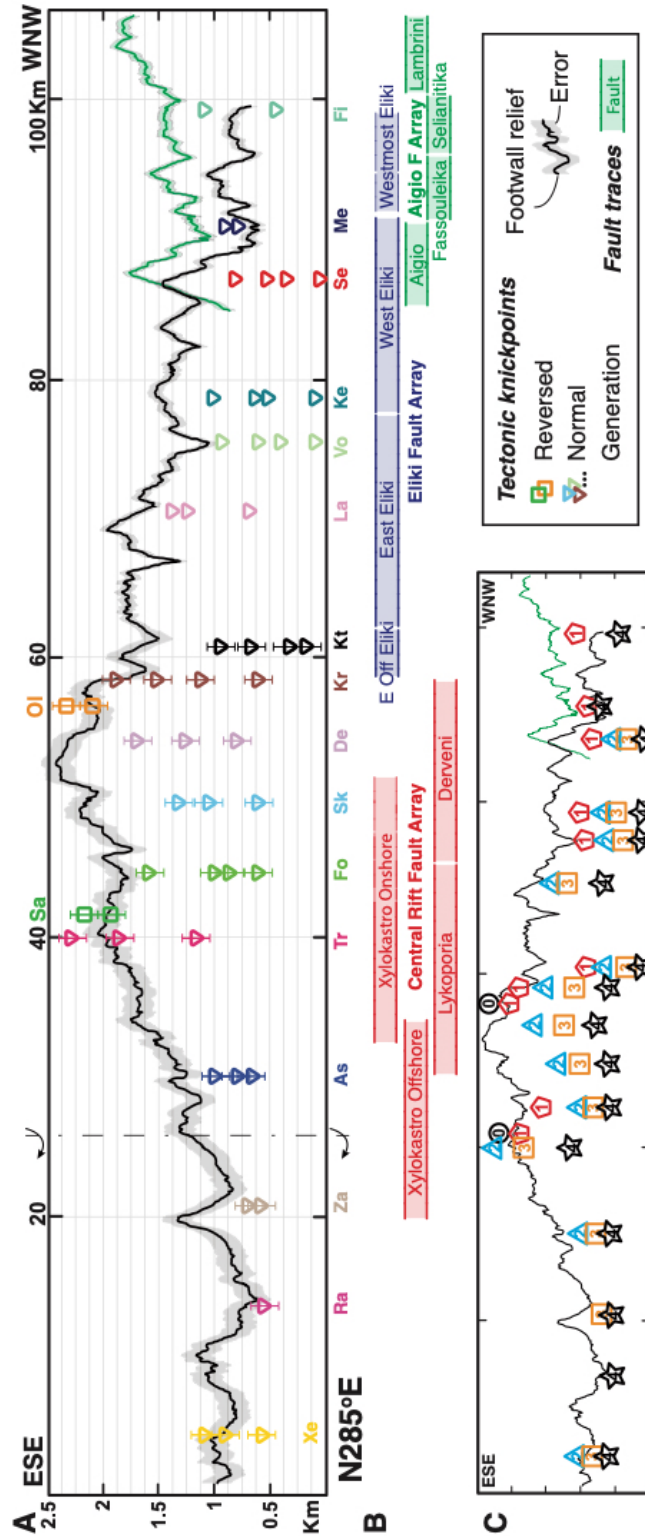


Fig. 14. Projection along master fault strike (N105°E) of footwall relief, and tectonic knickpoints of footwall river trunks with regards to the location of main fault segments. **(A)** Footwall relief of the master fault, and heights of main tectonic knickpoints of footwall river trunks, measured from the main fault. Footwall relief as in Fig. 10. Tectonic knickpoints of footwall rivers draining the gulf are plotted as triangles (see Table 1). Squares represent tectonic knickpoints seen for the trunks of the reversed rivers of (Sa) Safenetos (green) and (Ol) Olvios (orange). River networks are, from east to west: (Xe) Xerias, (Ra) Raizanis, (Za) Zapantis, (As) Asopos, (Tr) Trikalitikos, (Fo) Fonissa, (Sk) Skoupeiko, (De) Dervenios, (Kr) Krios, (Kt) Krathis, (La) Ladopotamos, (Vo) Vouraikos, (Ke) Kerinitis, (Se) Selinous, (Me) Meganitis and (Ph) Finikas. Tectonic knickpoints are projected perpendicularly to the master fault overall strike (N105°E) in two different manners. If the master fault is onshore, i.e. mapped with confidence, the intersection between river trunk and master fault sets the horizontal position of the projected knickpoint, while its height is measured vertically from the fault trace (as in Fig. 10). If the master fault is offshore and its trace is more uncertain, we derive horizontal position of the projected knickpoint as the average point of the projected lateral extent of its footwall catchment. Its vertical position is the tectonic knickpoint height measured vertically from the master fault trace, but we attached an estimative error equivalent to that used for the footwall relief. Further west than the vertical dashed line, elevations for both footwall relief and tectonic knickpoints are taken with respect to sea level, and raised to remain coherent with the easternmost end of the footwall relief in the central sector, and using the same errors. Errors are shown as an envelope for the footwall relief, and as bars for the heights of the knickpoints. Tectonic knickpoints in the reversed catchments are shown with the same error than rivers in the central area. Error bars for the eastern rivers (left of the dashed line) are maintained equal to those in the central sector. Error bars for the western rivers are smaller than the symbols. **(B)** Approximate location and extent of the main fault segments in the direction of projection. **(C)** Interpretation of the sequence of events associated with the tectonic knickpoints.

Our interpretation implies that both footwall relief and tectonic knickpoints are genetically linked, with perhaps the exception of the westernmost two river catchments (Fig. 13). Group 1 lays at highest positions (closest to the drainage divide) in all drainages and can be assumed to correlate with the initiation of tectonic activity at each individual fault segment. We interpret Group 2 as the result of hard linkage of such individual fault segments into the Eliki FA, with no connection farther west. We suggest that Group 3 formed by the effective connection of the main fault at the rift scale, i.e. by linkage of the master fault central sector with the Eliki FA. The lowest set of tectonic knickpoints that exist in all rivers (Group 4) formed at the moment of westward inclusion of the Aigio FA (section 2.2.3; Figs. 6 & 13).

We defend that this sequence is the most plausible geologically. Correlatable sets of tectonic knickpoints will develop in composite faults from their linkage onwards (“b” knickpoints in bottom two rows in Fig. 6), except at its tips or if the tectonic signal has not yet reached those rivers. Therefore, tectonic knickpoint sets on different faults can only be correlatable if linkage is already effective. For the west rift, the simplest scenario assumes that the tectonic knickpoints laying at lower elevations in the west rivers (Group 4 in Meganitis & Finikas, Figs. 13A,-B) formed coevally

and hence both correlate with just one set of tectonic knickpoints farther east. If the tectonic knickpoints laying at lower elevations in the west rivers would have formed coevally with older groups, other knickpoint sets, developed at later times, should have existed at lower elevations. On the contrary, our proposed tectonic disturbances for groups 2 and 3 respect the absence of tectonic knickpoints in the Aigio FA footwall rivers, laying farther west than our inferred fault tip at that time. Since linkage should be either the last or the second to last tectonic perturbation event in the sequence, on the basis of Fig. 13 only, the last two events could have taken place coevally or in a different order.

5.1.2 Rift southern shoulder

In the center of the rift, footwall rivers below the highest footwall relief (Trikalitikos to Krios rivers in Fig. 14A) have their tectonic knickpoints at the highest elevations and either 3 or 4 sets of tectonic knickpoints. Here, four out of the five knickpoints with the highest elevations of the entire southern rift flank are in the endorheic river basins of Olvios and Safenetos (Table 1). Westwards, as mentioned above, all footwall rivers have 4 tectonic knickpoints (Krathis to Selinous) laying at lower elevations, with the exception of Ladopotamos R (Fig. 14A), while only two tectonic knickpoints exist in the two westernmost footwall rivers (Meganitis and Finikas; Fig. 14). Analysis in the east was not performed, as it is prone to large errors in relation with the increasing distance between river outlets and the fault trace, and the fault location underwater. Overall, tectonic knickpoint heights measured vertically from the bounding fault system show overall triangular patterns that correlate with footwall relief at full rift-margin scale, with the exception of the lowest set in the westernmost two drainages (Figs. 13, 14 & Table 1). This implies that tectonic knickpoints and the active fault are genetically related (Whittaker and Walker, 2015).

Our interpretation points to initiation in relation to activity of individual fault segments, subsequent linkage and growth at full-rift scale (section 2.2.3, Fig. 6). We recognized five groups of

tectonic knickpoints in the central rift (groups 0 to 4, Fig. 14C). Group 0 implies an extra tectonic perturbation that is not seen elsewhere in the rift shoulder, that we suggest relate to the formation of individual fault segments in the rift center. The knickpoints of the lowest set in the endorheic drainages (Group 1) lay at heights that coincide with the footwall topography (Fig. 14A,-C), at elevations ~100 m lower than the windgap in Mavro area, where footwall relief is maximum, and at elevations of ~350 m higher than the windgap in the Klimenti area, where footwall relief is at lower heights. Therefore, we propose that Group 1 knickpoints belong to the second tectonic perturbation in a two-stage linkage process in the center of the rift.

This inference agrees well with other observations in the rivers in the central rift (from Trikalitikos to Krios; Figs. 12 & 14A), where two river trunks (Fonissa and Krios) have an extra, fourth knickpoint at the highest location, closer to the drainage divide than any other river in the rift (Table 1). This is, drainage reversal initiated earlier or was more pronounced in the present central rift, capturing one or two sets of tectonic knickpoints from (now) beheaded rivers. This is consistent with a fault slip rate increase that was more pronounced or older in the central rift, that we frame as fault linkage between two of the larger fault segments of the Central Rift FA, probably the Derveni-Lykoporia or the Onshore Xylokaastro F. We consider that the upper set of tectonic knickpoints seen in Fonissa and Krios is also related to this increase in fault uplift rate, and hence correlated as Group 1 in Fig. 14C.

We suggest that Group 2, i.e. the upper set of tectonic knickpoints seen in rivers of the central rift (Skoupeiko, Dervenios) and the third highest of Fonissa (Fig. 14A), results from the effective linkage of the Central Rift FA, which eventually disconnected the former river. Under this scenario, this second increase in uplift rate would be related as well with the uppermost set of tectonic knickpoints in Trikalitikos, and either prior or perhaps coeval with the third highest set of knickpoints (Group 3) in the river networks in the west. Connection with the Eliki FA, farther east is

proposed as the engine behind Group 3, seen almost everywhere along the rift, and supported by the relative higher elevation seen for this set in the Ladopotamos (Fig. 14A). Finally, Group 4 laying at the lowest heights show the common behaviour of the whole rift-fault system and seems to include the river basins in the westmost sector of the rift.

Regardless of the exact time sequence of events, we understand that the elevated position of the lowest tectonic knickpoint of the Meganitis (Fig. 14) reflects the fast vertical upstream propagation of the erosional wave (knickpoint area) expected for a linkage area (see for example Gallen and Wegmann, 2017) due to increased throw/uplift rates (e.g., Whittaker and Boulton, 2012). Our interpretation, taken together with the footwall relief plateau existing in the overlapping area of the Eliki FA and Aigio FA, suggests an “under-recovered” fault displacement profile and thus, a young linkage age (see our theoretical framework, section 2.2.3; Fig. 6, panel D). Moreover, the presence of solely two sets of tectonic knickpoints in the westernmost rivers, in comparison to the four sets found in rivers further east (with similar or larger drainage areas and reaching similar or larger maximum heights) supports that the aforementioned linkage took place by propagation (Fig. 6, panel D right)

5.2 Vertical motions in time

We attempt a reconstruction of the geometry of elastic flexure along the bounding fault strike (Fig. 17) using flexurally uplifted sets of coeval morphotectonic markers that formed at sea level (see section 2.3; Fig. 6). To such purpose, we calculate the height difference between sets as a proxy to relative vertical footwall motion occurring in the time lapse between their sequential formation. We project morphotectonic features towards the strike of the bounding fault (N105°E) (Figs. 9A,-B & 15, Table 2) and plot them together with footwall relief (see section 2.2.4 and 2.3). Locations Xy1 and Xy2 are exceptional since paleoshoreline angles of the same sea level highstands lay at considerably lower elevation away from the main fault (e.g., Armijo et al., 1996). This leads to Xy1

laying at lower elevations and significantly farther from the main fault system than any other plotted location (Figs. 7 & 15, Table 2). At Xy2, we used the MIS 5e level closest to the main fault and obtained the elevations of MIS 7e and MIS 9e that lay above it if we use best-fitting quadratic curves of extrapolated shoreline angles further away from the fault (as in de Gelder et al., 2018). Red circles are MIS 9e level at Xy1, Xy2 and Ps, and an undifferentiated MIS 9 in the other locations (Fig. 15).

Time constraints are based on the sea level highstands MIS 5e (124 ka), MIS 7e (240 ka), MIS 9e (326 ka) for the marine terraces paleoshoreline angles. Ages assigned for the foreset-topset contacts of Gilbert deltas are uncertain as they lack absolute dating (e.g., Gawthorpe et al., 2017b) and are based on disputed correlations (Rohais and Moretti, 2017 cf. Ford et al., 2016). For foreset-topset contacts of Pleistocene Gilbert deltas, we used a ~700 ka age proposed in Ford et al. (2016) for the abandonment by footwall uplift of the Middle Group deltas. We include in this group the Kolokotronis and Klimenti deltas, of potentially different age, to avoid effects in relation to the location of deltas with respect to the master fault (see Gawthorpe et al., 2017a). The age of the Mavro Gilbert delta is also disputed. We set the age of abandonment of the foreset-topset contact of Mavro to ~1 Ma (as in Armijo et al., 1996), although a significantly wider age bracket (1-2 Ma) is plausible. See details leading to this choice on section 3.1.1.

We infer protracted self-similar fault growth in the master fault since its genesis (Figs. 15 to 17A). Sets of contemporaneous marine terrace paleo-shorelines and Gilbert delta topset-foreset contacts have along-strike trends similar to those of footwall relief (Fig. 15), i.e. each set of correlatable morphotectonic markers has minimum heights in Xy1, maximum between Xy2 and Ak and intermediate heights between Ak and Ps. Correlatable morphotectonic markers thus point to self-similar vertical growth in the master fault since its onset with its nucleation point around the rift center (Section 2.3; Figs. 5 & 6).

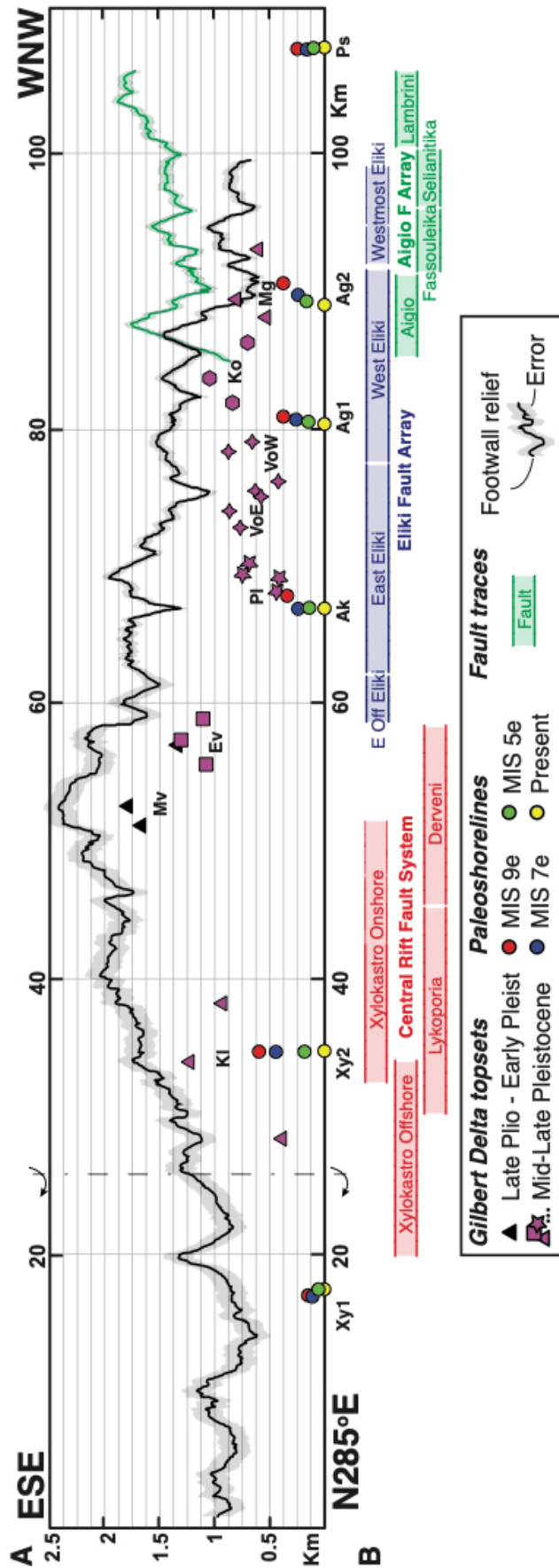


Fig. 15. Projection along master fault strike (N105°E) of major morphotectonic features with known or correlated age with regards to the location of main fault segments. **(A)** Major morphotectonic elements of the master fault footwall and footwall relief. Filled circles represent the location of paleoshoreline angles of the MIS 5e (green), MIS 7e (blue) and MIS 9e (red) highstands of flights of marine terraces grouped by location. From E to W; Xy1 and Xy2, for Xylokaastro area (paleoshoreline angles at low and maximum heights); Ak, for Akrata area; Aigio area, with Ag1 (paleoshoreline angles at the footwall of the Eiliki FA) and Ag2 (with MIS 5e and MIS 7e at its hanging wall and MIS 9 at its footwall); and Ps for Psathopyrgos (based on Armijo et al., (1996); De Martini et al., (2004); Houghton et al., (2003); McNeill & Collier, (2004)). Circles with yellow fill are the present day shoreline angles simplified as modern sea level (at 0 m), and are used only as a reference for the reconstructions in Figs. 15 & 16. Distinct filled geometric symbols represent the projection of the highest, lowest, eastmost and westmost location of the topsets of each Gilbert delta, as mapped in Fig. 7. Gilbert-delta topsets of Pleistocene age are in purple, while black triangles represent the topsets of the Late Pliocene - Early Pleistocene Mavro Gilbert delta. Gilbert deltas are label from E to W as Kl (Klimenti), Mv (Mavro), Ev (Evrostini), Pl (Platanos), VoE and VoW (Vouraikos, east and west), Ko (Kolokotronis) and Mg (Meganitis). In all cases, symbols are larger than associated errors. Footwall relief is defined as in Fig. 10. **(B)** Approximate location and extent of the main projection fault segments in the direction of projection.

| Object | Site | Source | X coord | Y coord | Level | Age (ka) | Elevat. (m) | Ze (m) | AbsUpliftRate |
|--|------|--------|---------|---------|--------|----------|-------------|--------|---------------|
| Paleoshoreline angle - Marine terraces | Xy1 | Own | 657252 | 4199244 | MIS 5e | 124 | 55.32 | 1.03 | 0.45 |
| | Xy1 | Own | 657449 | 4197907 | MIS 7e | 240 | 108.35 | 0.46 | 0.45 |
| | Xy1 | Own | 657276 | 4197519 | MIS 9e | 326 | 146.86 | 2.88 | 0.45 |
| | Xy2 | Own | 643328 | 4213762 | MIS 5e | 124 | 177.23 | 0.47 | 1.43 |
| | Xy2 | Own | n.a | n.a | MIS 7e | 240 | 347 | 5 | 1.45 |
| | Xy2 | Own | n.a | n.a | MIS 9e | 326 | 471 | 5 | 1.44 |
| | Ak | McNe | 613223 | 4225224 | MIS 5e | 124 | 135 | 5 | 1.09 |
| | Ak | McNe | 613014 | 4224383 | MIS 7e | 240 | 240 | 5 | 1.00 |
| | Ak | McNe | 611975 | 4223875 | MIS 9 | 326 | 350 | 5 | 1.07 |
| | Ag1 | McNe | 600178 | 4228598 | MIS 5e | 124 | 150 | 5 | 1.21 |
| | Ag1 | McNe | 599843 | 4228011 | MIS 7e | 240 | 255 | 5 | 1.06 |
| | Ag1 | McNe | 599575 | 4227668 | MIS 9 | 326 | 370 | 5 | 1.13 |
| | Ag2 | DeMa | 592506 | 4233848 | MIS 5e | 124 | 160 | 5 | 1.29 |
| | Ag2 | DeMa | 591685 | 4232525 | MIS 7e | 240 | 232 | 5 | 0.97 |
| | Ag2 | DeMa | 590492 | 4231081 | MIS 9 | 326 | 360 | 5 | 1.10 |
| | Ps | Houg | 575679 | 4241583 | MIS 5e | 124 | 95 | 5 | 0.77 |
| Ps | Houg | 575625 | 4241270 | MIS 7e | 240 | 160 | 5 | 0.67 | |
| Ps | Houg | 575545 | 4241047 | MIS 9e | 326 | 240 | 5 | 0.74 | |
| Gilbert delta topsets-foreset contacts | Ki | Own | 640560 | 4200259 | - | 700 | 1,192 | 35 | 1.70 |
| | Ki | Own | 647564 | 4205230 | - | 700 | 380 | 35 | 0.54 |
| | Ki | Own | 638068 | 4207654 | - | 700 | 893 | 35 | 1.28 |
| | Mv | Own | 624537 | 4212086 | - | 1000 | 1,751 | 35 | 1.75 |
| | Mv | Own | 625408 | 4209556 | - | 1000 | 1,604 | 35 | 1.60 |
| | Mv | Own | 619703 | 4211123 | - | 1000 | 1,285 | 35 | 1.29 |
| | Ev | Own | 620247 | 4214600 | - | 700 | 1,253 | 35 | 1.79 |
| | Ev | Own | 622593 | 4216435 | - | 700 | 1,032 | 35 | 1.47 |
| | Ev | Own | 619275 | 4216912 | - | 700 | 1,058 | 35 | 1.51 |
| | Pl | Own | 610754 | 4224444 | - | 700 | 394 | 35 | 0.56 |
| | Pl | Own | 611651 | 4223930 | - | 700 | 416 | 35 | 0.59 |
| | Pl | Own | 609534 | 4224008 | - | 700 | 659 | 35 | 0.94 |
| | Pl | Own | 610171 | 4223192 | - | 700 | 716 | 35 | 1.02 |
| | VoE | Own | 606786 | 4223762 | - | 700 | 739 | 35 | 1.06 |
| | VoE | Own | 605490 | 4223472 | - | 700 | 839 | 35 | 1.20 |
| | VoE | Own | 605032 | 4225862 | - | 700 | 557 | 35 | 0.80 |
| | VoE | Own | 604127 | 4224097 | - | 700 | 605 | 35 | 0.86 |
| | VoW | Own | 603985 | 4226231 | - | 700 | 403 | 35 | 0.58 |
| | VoW | Own | 601081 | 4226465 | - | 700 | 632 | 35 | 0.90 |
| | VoW | Own | 601539 | 4225371 | - | 700 | 839 | 35 | 1.20 |
| | Ko | Own | 597942 | 4225616 | - | 700 | 803 | 35 | 1.15 |
| | Ko | Own | 596556 | 4227337 | - | 700 | 1,005 | 35 | 1.44 |
| | Ko | Own | 593328 | 4225181 | - | 700 | 673 | 35 | 0.96 |
| Mg | Own | 592568 | 4229459 | - | 700 | 510 | 35 | 0.73 | |
| Mg | Own | 590827 | 4227958 | - | 700 | 778 | 35 | 1.11 | |
| Mg | Own | 587353 | 4228953 | - | 700 | 580 | 35 | 0.83 | |

Table 2. Data associated with the paleoshoreline angles and the Gilbert delta topsets, including assumed age and derived uplift rates. All names for the “Site” column are explained in Fig. 3. Sources of the data are marked as McNe (McNeill and Collier, 2004), DeMa (De Martini et al., 2004), Houg (Houghton et al., 2003) and Own (this contribution).

For the reconstructions in Figs. 17A & 18A, we represent the position of the Gilbert deltas topset-foreset contact as a single point calculated as the average, both in the vertical and the horizontal, of the points in Fig. 16A. We calculated the relative uplift rate of paleo-shoreline angles of flights of marine terraces at our six chosen locations (Fig. 17B & Table 2). We aid comparison among fault vertical motions reducing to one third the height difference calculated for markers uplifting from ~ 700 ka to 326 ka, and ~ 1 Ma to ~ 700 ka, i.e. maintaining rough time-steps of ~ 110 ka. We also put forward a rough estimation of paleo-relief prior to fault formation (blue lines in Fig. 17A), subtracting the envelopes of maximum relief within the drainage and within ~ 21 km from the bounding fault (Figs. 5B & 11), after simplifying both surfaces. The envelopes of maximum and minimum paleo-relief connect local highs and lows respectively, purposely neglecting local details of the relict relief. We note that the different distances to the fault of these envelopes of relief, as well as the effects of erosion and denudation, neglected in the comparison, might introduce an additional few hundred meters of uncertainty. Accounting for any of these corrections would lead to larger paleo-reliefs. We thus consider the paleo-relief estimation with care and as a minimum.

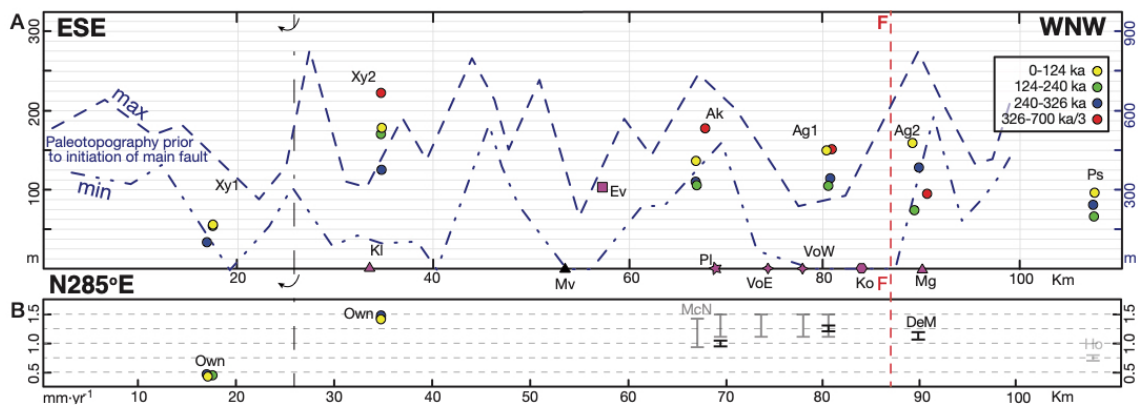


Fig. 16. Flexure geometry and evolution in time of the rift-forming fault of the Corinth Rift along strike, marked by relative elevation and age constraints of footwall morphotectonic elements, and pre-fault paleotopography. **(A)** Reconstruction in time-frames of main fault relative vertical motions. Symbols represent the relative elevations between two consecutive sets of morphotectonic markers formed at sea level. We applied specific corrections to consecutive markers that represent longer time-steps to plot roughly equivalent time-steps (~ 110 ka). Yellow circles: Present to 124 ka (124 ka). Green: 240 ka to 124 ka (115 ka). Blue: 326 ka to 240 ka (91 ka). Red: ~ 700 ka to 326 ka / 3 (~ 123 ka). Purple symbols: ~ 1 Ma to ~ 700 ka / 3 (~ 100 ka). Envelopes of estimated maximum and minimum paleotopography prior to the formation of the main fault are shown as a blue line with triple vertical scale. **(B)** Uplift rates of the marine terraces during aforementioned time frames and equivalent colors to those in panel (A) for own analysed terraces, and proposed ranges of uplift rates from Houghton et al., 2003 (Ho), McNeill and Collier, 2004 (McN) and DeMartini et al., 2003 (DeM).

Potential errors and uncertainties that exist in the time reconstruction are relatively minor in comparison with the main tectonic signal at full-rift scale. Reconstruction based on the marine terraces may be complicated by the interplay between depositional and erosional terraces, and the lack of accurate dating, given that most ages are inferred. Similarly, reconstruction based on the foreset-topsets Gilbert delta contacts have reduced levels of accuracy. Errors may exist in relation to Gilbert delta assigned age, cartography and vertical variations in the position of their foreset-topset boundary. We estimate that the associated uncertainty ranges between 5% and 20%, but no specific accountancy was performed. We also note that marine terraces are located significantly closer to the bounding faults than delta fans, and thus inferred rates of vertical motions for the latter will be comparatively lower when affected by the same fault slip rates. Despite aforementioned potential errors and uncertainties, we expect an accurate relative timing of events and satisfactory levels of precision in overall trends at the scale considered.

Overall, we infer at least ~100 m of onland uplift every ~110 ka all along the master fault footwall since its onset, except at the fault ends (Figs. 17A & 18A). We infer similar rates for the central rift between ~1 Ma and ~700 ka, while other areas along-strike lack footwall uplift during this period (Figs. 17A & 18A). Contrarily, footwall uplift seems to take place along the entire margin from ~700 ka to Present (Table 2; D-right in Fig. 5). Between ~700 ka and ~326 ka, a reconstructed onland uplift of ~60 m and ~90 m occurred every ~123 ka along most of the margin. The inferred vertical motion signal for this time frame lays almost flat, with larger heights at both ends. This is an unexpected signal in normal faults and may be an artefact resulting from the impossibility to track motion farther along-strike. Our data has two maxima at ~150 m and ~135 m (Klimenti and Meganitis; Figs. 15 & 16A) between 326 ka and 240 ka. This suggests a larger onland uplift for this period, an inference that we consider with care given the change in location with respect to the bounding fault from Gilbert deltas to marine terraces. We infer overall larger vertical motions for the period between 240 ka and 124 ka. An all time maximum in onland uplift at Xylokastro 2 lays at

~255 m and decays abruptly to the east and more gently to the west (Figs. 15 & 16A). Finally, between 124 ka and Present, onland uplift has two maximum (Figs. 15 & 16A), at ~180 m and ~155 m (Xylokastro 2 and Vouraikos West, respectively), and a minimum in Psathopyrgos at ~100 m. The overall profile is asymmetrical with the higher positions at the present rift center and lower elevations to the west.

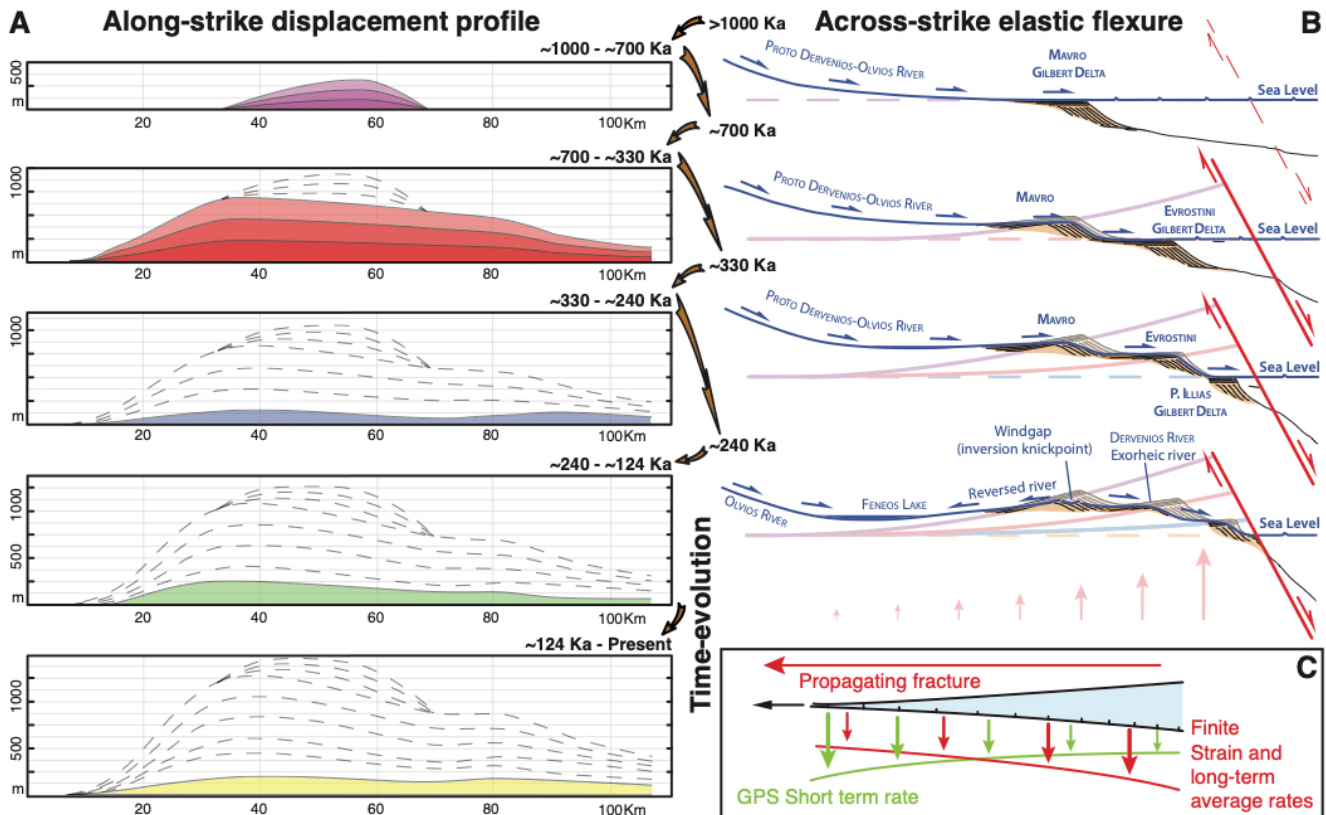


Fig. 17. Conceptual time-evolution of the master fault footwall evolution in time, shown along (A) and across (B) strike, and its propagation in map view (C). **(A)** Time-evolution of displacement profiles assuming continuity among the data points shown in Fig. 15. Each line represents a displacement profile of the master fault above a sea level each ~110 ka. Each displacement profile was drawn manually joining the data points and assuming a smooth profile. For the top two panels, we derived the rest of the profiles by simple vertical addition of the first displacement profile by 2 and 3 times, respectively. Panels (B) and (C) are not to scale. **(B)** Conceptual time-evolution of the footwall elastic flexure of the master fault in the centre of the rift and the associated evolution of Gilbert delta(s) and river profile(s) (roughly at the location shown in Fig. 4; slightly modified from Fernández-Blanco et al., 2019b). Flexural uplift of the footwall is shown in similar colours to those in panel A. The upper profile correspond to the Early-Mid Pleistocene, and the bottom profile represent Modern times. In-between times steps were not specifically constrained, but can be roughly assigned to >1 Ma, ~700 ka, ~326 ka and <240. Drainage reversal could have taken place anytime after ~700 ka (see details in Fernández-Blanco et al., 2018). **(C)** Conceptual map-view representation of the Corinth Rift opening along its axis as a propagating fracture, and a simple representation of the implied associated finite strain and long-term average and modern GPS “short-term” rates.

6 Discussion: Opening of the modern Corinth Rift in the Aegean domain

We examine the implications of our results for the Corinth Rift, and extrapolate our findings into the Aegean. We address discrepancies on the rift bounding fault(s) in the southern shoulder (section 6.1), derived rift mechanical models, unlying lithosphere (section 6.2) and evolution (section 6.3), and Aegean tectonic models (section 6.4).

6.1 Recap: Landscape response to a new rift forming fault

The present rift-bounding fault is a single composite master fault >80 km-length. Footwall relief of the active fault is roughly symmetrical with a single maximum in fault throw at its center that correlates with the Central Rift FA, and decays along rift strike (Fig. 14A). This signal is also reflected in the decay in topographic and relief heights (Figs. 8, 10 & 11), the morphology of footwall catchments (Fig. 13A), and the heights of coeval marine terraces and perched Gilbert deltas (Figs. 9A,-B, 14 & 15), among other things. Using fault footwall relief as a proxy for fault displacement profile (see section 2.2.4, Figs. 4 & 5), this trend suggest that discrete en-échelon surficial fault segments (Fig. 7) are hard-linked into a kinematically coherent fault at depth. These evidences corroborate that the rift-bounding is a single, composite master fault, ad minimum, from the eastern end of Offshore Xylokastro F to the Westernmost Eliki F (Fig. 14A).

The composite master fault grew along its strike from the rift center. The correlation between triangular geometries in relief and their respective faults (cf. Fig. 14A and Fig. 14B), indicates that the master fault grew by successive linkage of individual fault strands linking into larger fault segments in time (see section 2.1 & 2.3). For example, the ~12 km-wavelength up-pointing triangle that sets the maximum footwall relief is formed by three individual triangles and correlates with the Derveni and (partially with) the West Onshore Xylokastro fault traces (Fig. 14A,-B). This is indicative that either of these faults or both together have the largest slip and are the

oldest fault segment(s) of the composite master fault, and suggest its onset of activity took place in relation to three individual fault segments before linking into the Derveni F and/or the West Onshore Xylokaastro F. Coherent with the above, displacement-length relationships (Dawers et al., 1993 and section 2.1) suggest that the Central Rift FA is the oldest of the rift master fault, as it has the largest along-strike lengths at surface (Figs. 7 & 8), maximum relief offset (Fig. 10) and footwall relief (Fig. 14A), as well as the maximum fault displacement (Fig. 3 in de Gelder et al., 2018).

Individual fault strands linking into larger faults propagated westwards in time. Footwall relief in the western sector of the rift (Fig. 13) can be attributed to individual growth of fault segments that eventually linked with the composite fault as it propagated westwards (Figs. 5 & 6), including the Eliki FA, and more recently, the Aigio FA. Fault segment linkage and westward propagation of the composite fault is well supported by the footwall relief maximum in elevation of the Eliki FA decaying west (Fig. 13) and its overall correlation of up-pointing triangles with individual fault segments. The high elevations of the Aigio F footwall relief with regards to the overall west-rising trend of the Aigio FA footwall relief (Fig. 13) are probably the result of the mechanical interaction between the Aigio FA and Eliki FA. This is similarly supported by the gentle westwards increase of the footwall relief associated with the Fassouleika and Selianitika faults (in the overlapping area between Eliki and Aigio FAs) (Fig. 13) and suggests a very recent fault linkage that has not yet entirely recovered in its displacement profile (Figs. 6, 13 & 14).

The diachronic along-strike onset of master fault of the Corinth Rift controls the modern rift along- and across-axis asymmetry (Figs. 8 to 12). Fault hierarchy is better expressed in the rift center (Fig. 8), where the rift asymmetry is marked along a northward transect by up-flexed topography with a master fault footwall width of ~15 km (Fig. 10) nearby its maximum footwall relief of ~2.5 km (Fig. 14A) followed by pronounced syntectonic sedimentary wedges opening southwards (e.g., Taylor et al., 2011) and a northern coast dominated by subsidence (Bell et al.,

2009; Elias et al., 2009). Contrarily, symmetric rift sectors at the tips the Corinth Rift are set by conjugate faults dipping south (Fig. 8), in areas where faults are seismically active at present (Jackson et al., 1982; Ambraseys and Jackson, 1990; Hubert et al., 1996; Bernard et al., 2006; Godano et al., 2014; Duverger et al., 2015).

Coupling footwall relief and tectonic knickpoints (Fig. 14) with fault displacement profiles in time (Fig. 16A) within the context of our theoretical framework (Fig. 6) allow us to propose a sequence of events with (i) fault initiation of fault segments in the central rift sector, (ii) growth and simple linkage of fault systems in the central area of the southern shoulder of the rift, and initiation of fault systems in the west, followed by (iii) connection by simple linkage of the Central Rift FA as a whole, and that of the Elike FA, (iv) growth and connection of both fault systems by west propagation, and (v) younger inclusion of the Aigio FA by further west propagation.

We produce a schematic reconstruction of the fault footwall flexure and cumulative displacement profile in time (Fig. 17). This reconstruction allocates the development of the main morphotectonic features of the present rift south margin in the frame of growth of the master fault and the concomitant elastic uplift rates, and illustrates the growth of the structural relief in relation to the modern master fault along and across strike. The reconstruction shows the progressive growth of the system laterally along-strike as in this contribution (Fig. 17C) and the concomitant step-by-step abandonment of Gilbert delta fans and the large-scale drainage reversal as in Fernández-Blanco et al., 2019b (Fig. 17B). A similar geometry of propagation is expected for the opening of a tensile crack (Fig. 17C).

Previous extension in the area plays only a subsidiary role in the formation of the modern Corinth Rift. The relationship between the envelope of maximum relief in drainage and at ~21 km from the bounding fault (Figs. 11 & 16) suggests ~50-to-75% of the main shoulder topography is related to its present active fault, i.e. that ~1/2-to-3/4 of the present topography developed since

the onset its current rift bounding fault, and thus in $\sim 1/5$ of the time since extension initiated in the area (~ 4 -5 Ma). Consequently, the morphology of the current rift shoulder and the most relevant features seen along the rift shoulder are not related with the antecedent distributed extension for the preceding ~ 4 My.

Most other features in the modern rift are also controlled by the master fault; from rift basin extent and geometry to the size and distribution of synsedimentary wedges, from the morphology of river catchments to the location and extent of coeval marine terraces and perched Gilbert deltas with respect to the main fault system and their relation with other morphotectonic features along the rift margin (Figs. 7 to 15). These features allow us to confidently track the activity along the Holocene-active surficial fault segments (e.g., Hubert et al., 1996; Rigo et al., 1996; Stewart and Vita-Finzi, 1996) in the Corinth Rift southern shoulder (e.g., Armijo et al., 1996; De Gelder et al., 2018) back to master fault onset, ~ 700 ka (Figs. 14 to 17A). On this basis, we understand the unconformity at basin-wide scale and the abrupt shift in sedimentation (e.g., Ori, 1989; Sachpazi et al., 2003) as the result of the onset of activity along the master fault and the associated increased slip rates (Fig. 17; Fernández-Blanco et al., 2019a). In sum, the geology, relief, and morphotectonic markers of the Corinth Rift master flank favour that a new fault growing rapidly from its center along strike controls the modern rift evolution.

6.2 Mechanical models of the modern Corinth Rift and its lithosphere

The above evidence discards listric detachment fault geometries and fail to support detachment models (Rietbrock et al., 1996; Rigo et al., 1996; Briole et al., 2000; Jolivet et al., 2010) that might apply further to the SE and in SW Turkey (Jolivet et al., 2010, 2013). Instead, the wavelength and amplitude of the master fault elastic flexure and footwall uplift (Figs. 10 to 11, 15 & 16) can only be produced by steep planar faults (e.g., McNeill et al., 2005; Bell et al., 2011), reaching at least the brittle-ductile transition (Bell et al., 2017) and developing in a strong lithosphere (King and Ellis,

1990; Buck, 1991, 1993; Resor and Pollard, 2012; De Gelder et al., 2018). High uplift-subsidence ratios along the rift margin (McNeill and Collier, 2004; De Gelder et al., 2018) as well as a localized Moho rise (Zelt et al., 2005; Pearce, 2015) further support this conclusion.

Normal fault aspect ratios (Walsh and Watterson, 1988; Cowie and Scholz, 1992a, 1992b; Dawers et al., 1993; Scholz, 2002) dictate that a single fault of rift-scale length may reach the Moho. We use fault aspect ratios (see sections 2.1) to derive master fault down-dip lengths and assign dip angles to estimate its extent at depth. We use very high (1), average (3) and very conservative (5) fault aspect ratios (e.g., Cartwright et al., 1995; Nicol et al., 1996), of a master fault with a surface length of >80 km (minimum derived from the footwall relief, Fig. 14A) and ~130 km (mapped cumulative length, Fig. 7) and dips of 45° and 60° (as in Rohais et al., 2007; Bell et al., 2008; Taylor et al., 2011; Ford et al., 2012). Fault depth extent ranges from values of >16 km for extremely conservative assumptions to upper end values of ~110 km. Importantly, both the depth of the detachment faults proposed to control the mechanical evolution of the Corinth Rift (e.g., Rigo et al., 1996; Sorel, 2000) and the thickness of the seismogenic layer (~10-15 km) are surpassed even by our most conservative estimates of fault depth extent. In our educated guess, we use an average fault aspect ratio (3), fault length (100 km) and dip (55°) that yields fault tip depths of ~27 km, i.e. a fault that affects virtually the whole crust, albeit through more diffuse ductile shear in the lower crust. Taking into account that surface length is a minimum estimate of total fault length, we conclude that the master fault of the Corinth Rift reaches the lower crust.

Similarly, we show evidence on master fault extent, elastic flexure, along-strike propagation and fast associated uplift rates (Figs. 13 to 17) that put into question rift models of uninterrupted progressive strain localisation. Our evidence is at variance with a continued migration of normal faults basinward in which strain localisation and block tilting is progressive since extension onset in the area (e.g., Goldsworthy and Jackson, 2001; Goldsworthy et al., 2002; Ford et al., 2012, 2016).

While basinward fault migration is probably the main extension mechanism (e.g., Gawthorpe et al., 1994; Goldsworthy and Jackson, 2001) before the onset of the presently active master fault, the along-strike dimensions and estimated vertical offsets of antecedent faults are small (e.g., Ori, 1989; Ford et al., 2012) when compared to the ~80-to-130 km along-strike length (Figs. 7 & 8) and ~5 km vertical offset along the active fault system (De Gelder et al., 2018). Our data suggests paleo-relief minimum estimates with means of ~300 m and maxima of ~700 m (Fig. 16), which suggest elevations of <1 km for the antecedent paleotopography. Moreover, the distributed extension rates $<1 \text{ mm} \times \text{yr}^{-1}$ accommodated by antecedent parallel faults for $>3 \text{ Myr}$ since the onset of extension (Ford et al., 2012) are now more than one order of magnitude larger ($>11 \text{ mm} \times \text{yr}^{-1}$; Avallone et al., 2004) and highly localised in the current rift-bounding fault system (Figs. 8, 9E, 10, 11). We take our data and interpretation, and the aforementioned evidence, together with the observation that antecedent faults in the east of the rift are transected by the younger fault system (Figs. 7 & 8) to infer disruptive fault growth and a two-phase rift growth model (see below).

Our data supports that the modern Corinth Rift is a short-lived flexural cantilever rift sustained by active seismicity during many earthquakes cycles (King et al., 1988; Kuszniir et al., 1991). Upper-crust and whole-crust extension estimates (Bell et al., 2011) suggest antecedent pure-shear extension (McKenzie, 1978b) in the area. Both these rift growth mechanisms imply a strong lithosphere rheology (e.g., Ziegler, 1988; Buck, 1991; Brun, 1999) under the Corinth Rift. A Corinth Rift lithosphere that holds significant long-term strength (Fig. 3, upper row) is compatible with constraints on the rheology of the lithosphere under the rift derived from quantification of elastic flexure and a detailed 2D record of rift master fault growth in time that is to our knowledge unique worldwide (De Gelder et al., 2018). This set of coeval time-strain markers detailedly tracking the growth of a rift-bounding fault may typify continental lithosphere on 10^3 - 10^4 yr timescales in relation with fast, localized tensional strain (De Gelder et al., 2018). Similar flexural uplift and U:S

ratios at the Eliki FA location (McNeill et al., 2005), the rift topographic geometry and wavelength and its coherency with the geology and geomorphology along rift strike (Figs. 9 to 11, 15) suggest that a equivalent lithospheric rheology occurs at the scale of the rift since its onset.

6.3 Two-phase opening of the Corinth Rift

We reconstruct the opening of the Corinth Rift since its onset. We integrate the rift first-order geological observations and spatiotemporal variations shown here with constraints by previous contributions. The antecedent extension in relation to the northwest tip of a slab rollback extensional trough (section 6.3.1) is differentiated by a switch in rift mechanics (section 6.3.2) from the disruptive along-strike growth of a new crustal fault (section 6.3.3) leading to the opening of the modern Corinth Rift (section 6.3.4).

6.3.1 Antecedent distributed extension

Constraints prior to modern master fault onset shown in this section come largely from other contributions and the reader is referred there for further details. Absolute age constraints are scarce during the early phase of antecedent distributed extension (see Gawthorpe et al., 2017b) and are still a matter of debate (Rohais et al., 2007 a, b; Ford et al., 2016; Rohais and Moretti, 2017).

Distributed extension tipping out to the west over Hellenic paleo-topography initiated at ~5 Ma (e.g., Keraudren and Sorel, 1987; Doutsos and Piper, 1990; Rohais et al., 2007; Ford et al., 2016; Gawthorpe et al., 2017b). Distributed normal faulting may have started between 5 and 4 Ma south of the present rift (e.g., Doutsos and Piper, 1990; Ford et al., 2016). Extension rates decreased westwards from estimates of 1.5-2.3 mm×yr⁻¹ in the center to 0.6-1 mm×yr⁻¹ in the west rift (e.g., Ford et al., 2016), suggesting a diachronic extension onset that tipped out to the west (Ford et al., 2012; Gawthorpe et al., 2017b). Well-established catchments drained N-to-NE inherited Hellenic paleotopography regionally plunging east, while local hanging-walls controlled along-strike

sedimentary flow paths (Ford et al., 2012; Hemelsdaël and Ford, 2016; Gawthorpe et al., 2017b). The aforementioned evidence agrees well with the growth of a new graben structure at the northwest tip of a south-arched extensional trough developing due to the Hellenic slab rollback.

A symmetrical graben that narrowed westward established after fault migration northward at ~2 Ma (e.g., Rohais et al., 2007; Leeder et al., 2008; Bell et al., 2009; Ford et al., 2009, 2012, 2016; Gawthorpe et al., 2017b). New N- and S-dipping faults formed a less-distributed symmetric graben (Bell et al., 2009; Taylor et al., 2011; Nixon et al., 2016) after a ~10-30 km northward shift in extension locus (e.g., Ford et al., 2016; Gawthorpe et al., 2017b). Fault migration poorly dated between ~2.2 and ~1.8 Ma (Malartre et al., 2004; Rohais et al., 2007 a, b; Leeder et al., 2008) suggest potential diachronic onset of fault activity initiating earlier in the central rift (Gawthorpe et al., 2017a). Fault systems in the central rift (Central Rift FA) initiated at modern margin positions (Bell et al., 2009; Nixon et al., 2016) and have accumulated slip since then (Figs. 15 to 17; Ford et al., 2016). The Central Rift FA accumulated ~1/4 of its throw during this time (Nixon et al., 2016). The border fault system propagated west in a graben that narrowed from ~20-25 km in the center to ~10-15 km in the west (Ford et al., 2016). The fluvial network changed to N-flowing rivers that started reworking footwall uplifted sediments and Gilbert deltas formed in new hanging-walls (e.g., Ford et al., 2016; Gawthorpe et al., 2017b). For example, the Ilias and Evrostini deltas developed foresets of hundreds of meters after its feeding river cannibalised previously-depositing Killini and Mavro deltas (Ford et al., 2016). Evolution during this time frame is compatible with further entrenchment, westward propagation and southward arching of the back-arc trough.

6.3.2 Change in extension mechanics

A basin-wide unconformity and sedimentation switch (e.g., Ori, 1989; Sachpazi et al., 2003) at ~800-600 ka (e.g., Ford et al., 2016; Nixon et al., 2016; Gawthorpe et al., 2017b) resulted from an abrupt tectonic event at the rift scale (e.g., Armijo et al., 1996; Fernández-Blanco et al., 2019a). Over

a time span of ~300 ka, the antecedent complex and distributed rift structure shifted to the modern markedly asymmetrical rift growing in relation with N-dipping faults in the southern flank (Fig. 9D,-E; Figs. 8c and 11c in Nixon et al., 2016). During this tectonic event, fault activity focused on the Central Rift FA (Figs. 14 to 17), increased in the eastern Perachora and East Alkyonides faults (Nixon et al., 2016) and initiated in the western Eliki FA (e.g., Ford et al., 2016; Gawthorpe et al., 2017b) as well as in both Eratini faults (e.g., McNeill et al., 2005; Bell et al., 2008, 2009). Concomitantly, all antecedent faults of the southern margin died (Gawthorpe et al., 2017b) while S-dipping faults in the northern margin, like the Galaxidi Fault, significantly decreased activity and eventually deceased (Bell et al., 2008, 2009; Nixon et al., 2016). During this tectonic event, the dynamics of rift growth radically changed from slow-growing distributed faults to fast-growing elongated features that linked along strike to set the modern rift margin (Figs. 15-17).

6.3.3 The advent of the modern Corinth Rift

The change in extension mechanics (section 6.3.2) occurred as a new rift-forming fault grew by linkage of individual faults along-strike, leading to an abrupt increase in tectonic rates. We suggest that the Derveni, Lykoporia and Offshore Xylokastro faults linked into the Central Rift FA that became the principal focus of extension (Fig. 14; section 5.1.2). Here, fast fault lengthening and concomitant footwall flexure leads to the development of new footwall relief (Figs. 14 to 17), the eventual abandonment and perching of Gilbert deltas, and disruption and reversal of large drainages (Fig 17; Fernández-Blanco, 2019b). In the central rift, the abandonment of the Evrostini delta and the defeat of its feeding river is estimated to have occurred some time after ~700 ka (Rohais et al., 2007; Ford et al., 2016). Lesser footwall relief existed in the west rift (Figs. 15-17) where homologous syn-rift deltas remained at hanging-wall positions of the bounding fault (Gawthorpe et al., 2017a). Here, rivers cannibalized their Gilbert deltas and the pre-rift units, and continue to flow north (Ford et al., 2016; Gawthorpe et al., 2017b), probably due to a relatively younger uplift rate change (Fig. 12; Fernández-Blanco et al., 2019a). This is, time-transgressive fault

propagation evolved along rift strike (Fig. 17C) from the present rift centre, leading to differential rift flank response and the associated asymmetric fault footwall flexure that is readable in the heights of terraces and delta topsets as well as the extent of the uplifted basin (Fig. 9A,-B,-C), the rift variable topography (Figs. 10 & 11), and the longitudinal profiles of gulf-draining rivers (Fig. 12).

Rift across-axis asymmetry since ~400-300 ka (Nixon et al., 2016; Gawthorpe et al., 2017b) is sustained by high uplift rates in rift-forming faults propagating along-strike (Fig. 16). Subsidence and deposition of linked depocenters in the hanging-wall (Nixon et al., 2016) and the growth of footwall relief (Figs. 14 to 17) is controlled by north-dipping faults bounding the rift to the south. High uplift/subsidence ratios of 1:1.2-2.4 for the central rift (De Gelder et al., 2018) and 1:2-3.2 for the west rift (McNeill and Collier, 2004) result from highly localised strain and elastic flexure in the master fault (Fig. 8 & 17B). Flexural uplift lead to rates that surpass $1 \text{ mm}\times\text{yr}^{-1}$ along most of the rift, with the exception of its tips (Fig. 16B). These uplift rates correlate with a change in extension rates from $\sim 1\text{-}2 \text{ mm}\times\text{yr}^{-1}$ to $\sim 10\text{-}15 \text{ mm}\times\text{yr}^{-1}$ (Avallone et al., 2004; Ford et al., 2016). Overall relative low tectonic rates before $\sim 700 \text{ ka}$ might be related with growth of slow depocenters and regional uplift, while remarkably high tectonic rates at present along most of the margin relate with fast growth of an asymmetric rift basin and flexure due to the new rift-forming fault.

Further master fault westward propagation along strike initiated the Aigio FA and the Psathopyrgos F. Here, fault activity started as well in the Marathias and Nafpakos faults of the northern margin (Beckers et al., 2015). This resulted in a second unconformity in the area (Bell et al., 2008) and the opening of the Rion Strait at equivalent times (Ford et al., 2016). Flattening of the footwall relief profile in the west and the reduced number of tectonic knickpoints (Figs. 14 & 15) suggest that fault activity in the area results from westward propagation of the master fault (Fig. 6). Changes in elevation of the longitudinal river profile major inflexions and the reduced magnitude of related river channel steepening are also consistent with this inference (Fernández-Blanco et al.,

2019a). Further supporting evidence are the recent hanging-wall uplift in the footwall of the Aigio F (Palyvos et al., 2005) and its age (50-60 ka; Cornet et al., 2004), as well as the large seismicity in the Aigio, Fassouleika and Psathopyrgos faults (Bernard et al., 2006; Boiselet et al., 2014; Duverger et al., 2018). Eastwards propagation at the scale of the rift is also likely to have occurred at younger times than those suggested by Leeder et al. (2012). Activity of the easternmost faults is clearly evidenced by Holocene and historic fault ruptures in the Alephori and Pisia faults (Jackson et al., 1982; Hubert et al., 1996; Mechernich et al., 2018) as well as in antithetic Kapareli Fault (Benedetti et al., 2003), and is probably limited in extent by mechanical restrictions further east, imposed by the near-orthogonal orientation of faults belonging to the antecedent back-arc trough.

6.3.4 The modern Corinth Rift at present

Continued self-similar growth of the master fault sets the modern Corinth Rift asymmetry, localising strain during its along strike propagation. Individual fault segments grew from the modern central rift along strike, and linked to form larger faults that eventually coalesced into the current master fault. Nixon et al., 2016 suggest that full fault linkage occurred at ~130 ka. The master fault kinematic link at depth results in subsidence distributions (Nixon et al., 2016) and footwall relief (Fig. 14) that shows rift-scale parabolic shapes flattened to the west. As the master fault grew in a self-similar fashion, footwall-uplifted coeval morphotectonic features distributed self-consistently along the margin (Figs. 15), leading to a highly-localised asymmetric rift (Fig. 17B) (De Gelder et al., 2018). Contrarily to the above, symmetric cross-sectional geometries are maintained at both rift ends, where south-dipping faults in the northern rift margin develop along strike prior to strain localisation and kinematic control along the north-dipping fault plane of the active master fault system.

In the west rift, strain is distributed among a few steep opposite-dipping faults (Nixon et al., 2016) where the youngest, ongoing propagation of the master fault takes place (Fig. 13, 14 & 17).

The west rift has its highest geodetic extension rates (e.g., Avallone et al., 2004) and a north-dipping microseismicity layer (Lambotte et al., 2014) holds the highest seismicity in Europe. Both features contrast with the relatively minor antecedent extensional strain for the area (e.g., Bell et al., 2011). The Aigio and Fassouleika faults show normal focal mechanisms dipping $\sim 45^\circ$ and 60° north at the interphase with the microseismicity layer (Duverger et al., 2015). On this basis, we speculate that this layer is the low-dipping detachment of the antecedent extensional system (Rietbrock et al., 1996; Rigo et al., 1996), and that the new high-angle rift-forming fault reported here has not yet successfully transected this layer. This would imply that the westernmost rift holds at depth the interphase between the antecedent, distributed extension and the localised, modern Corinth Rift. Being this the case, both the high seismicity and the anomalously high geodetic extension rates in the area would result from the mechanical interaction between both features. This hypothesis, in turn, agrees with the quick decrease in Moho depth (Zelt et al., 2005; Sachpazi et al., 2007), as the modern rift-forming fault affecting the entire crust at its centre (section 5.1.2) tapers out towards its tips.

6.4 Two-phase evolution of the Anatolian-Aegean plate

Many observations in the Corinth Rift support the ‘two-phase linear-elastic’ Aegean model (e.g., Armijo et al., 1996; Flerit et al., 2004). Strain localisation by elastic failure rather than viscous deformation (e.g., Houseman and England, 1986; Kuszniir and Park, 1986; Burov and Diament, 1995; Watts and Burov, 2003; Burov et al., 2006; Bürgmann and Dresen, 2008) is suggested by the strong lithospheric rheology of the Corinth Rift (section 6.2; De Gelder et al., 2018). Our comprehensive model is compatible with early extension at the northwestern tip of an back-arc extensional through, followed by the disrupting growth of a new fault system in relation to the external tectonic forcing imposed by the North Anatolian Fault. In other words, the early phase has an evolutionary structural style that can be explained by self organisation of the fault network

(Cowie, 1998; Cowie et al., 2000, 2006; Gawthorpe et al., 2003, 2017b; Nixon et al., 2016). Contrarily, the second phase involves drastic and fast changes in normal fault dynamics in relation with the Corinth Rift unique tectonic setting (Armijo et al., 1996; Flerit et al., 2004; this contribution).

The southward propagating tip of the NAF modified the preexisting Aegean back-arc extension since ~5 Ma (Armijo et al., 1999), as the northern boundary of the Aegean-Anatolian plate, and thus the plate itself, formed. Stress interaction between the the latter features and those of the process zone (Hubert-Ferrari et al., 2003) resulted in the development of the North Aegean Trough, Evvia and Corinth extensional fault systems (Armijo et al., 2004; Flerit et al., 2004), while reducing extensional processes in the Cyclades. Transtensional stresses lead by the southwestward propagating tip of the North Anatolian lithospheric transform fault (Armijo et al., 2004; Flerit et al., 2004) superimposed onto pre-existing tension in the Corinth Rift. The modern Corinth Rift opened as pre-existing structures of precedent extension guided the growth of the new master fault, much like a crack in fracture mechanics.

The disruptive growth of a new fault resulted in elevated tectonic rates that occur all along such master fault for at least ~320 ka that can be extrapolated, with less well-constrained strain markers, for a period covering the entire growth of master fault relief (Figs. 16 & 17). These rates have increased by one order of magnitude since its onset of extension (Ford et al., 2012), and are up to one order of magnitude larger than rates in most normal faults, and often notably larger than those in Aegean (Armijo et al., 1996). Associated extension rates are similarly unrepresentative of common intracontinental interiors (Charalampakis et al., 2014) and agree well with rates in plate tectonic boundaries (cf. Müller et al., 2008). The above suggests long-term elastic behaviour (Hubert-Ferrari et al., 2003) of the Aegean lithosphere and rift growth at the tip of a propagating tectonic plate boundary, and in turn explains well the unique characteristics of the Corinth Rift.

7 Conclusions

We use the rich record of strain markers along the Corinth Rift main shoulder to characterise the kinematics of its rift-forming fault system and propose a model for the formation and evolution of the modern rift, and discuss its mechanic and tectonic implications. To constrain our model, we compile and reassess morphotectonic and stratigraphic features in the rift and examine its relief.

Footwall relief in the master fault portrays the displacement profile of a single fault, with a clear maximum in its center (Mavro area). Such displacement profile characterizes at present a single rift-scale fault >80 km along strike that reaches depths of the basal crust or lithospheric mantle. Present rift topography reaches similar elevations within 10 km of the modern master fault for most of the rift, clearly surpassing former topography. The clear link between modern topography and geologic/morphologic features all around the rift further suggests that the previous extension is superfluous to explain the modern Corinth Rift evolution. Multiple evidence support onset of the modern master fault at the rift center by simple fault linkage of individual faults that grew into larger systems. This is expressed as a correlation among individual fault segments and their footwall relief up-pointing triangular geometries, which collectively compound triangles of larger wavelengths. Similar deductions for the lower footwall relief observed in the west rift suggest similar yet younger fault growth and lateral linkage into a larger fault.

We put forward a conceptual framework to characterise the lateral and vertical evolution of the Corinth Rift master fault, using fluvial geomorphology and normal fault mechanics. We deduce the lateral propagation of fault activity westwards, where the master fault is presently most active. This is primarily manifested by the asymmetry of its fault displacement profile in couple with the absence of tectonic knickpoints in the west catchments. More specifically, the master fault displacement profile is almost entirely recovered to a single fault aspect ratio, but is flat and thus “unrecovered” in its westernmost end, where the along-strike correlation among tectonic

knickpoints valid for the rest of the rift is absent. The evolution of active normal fault systems at other sites may also be constrained using similar conceptual frameworks.

We infer an evolution sequence for the Corinth Rift master fault and the concomitant opening of the rift. Such evolution is supported by our aforementioned conceptual framework, as well as by the location and extent of tectono-morphologic, stratigraphic and seismo-tectonic evidence, onshore and offshore, and consists of five events: (i) initiation of individual fault segments in the central sector; (ii) growth and simple linkage of fault segments in the central rift, and initiation of individual fault segments in the west; (iii) connection by simple linkage of the main faults at the rift center into a composite fault system, and that of the Eliki Fault Array; followed by (iv) growth by west propagation and connection of both fault systems, and (v) propagation farther west, with the inclusion of the Aigio Fault Array in recent times.

We propose a comprehensive two-phase rift growth model. Distributed extension occurred symmetrically and at low rate atop the Hellenic basement since the Early Pliocene. During ~4 My, this extended area progressively migrated northwards and further entrenched westward. At ~800-600 ka, an abrupt tectonic event (spanning for ~300 ky) radically changed extension mechanics, and the resulting rift geometry and tectono-sedimentary dynamics. Since Middle Pleistocene, the synchronous onset of asymmetric rifting occurs at fast rates as the new fault system grows along strike from the present rift centre. Master fault growth by propagation result in new symmetrical rift sectors along-strike that are later overwritten by further propagation and strain localisation of the primary fault system.

All the above suggests that the evolution of the Corinth Rift results from localized fault propagation at plate boundary rates in a strong lithosphere. This rift-forming fault controls the active tectonics, morphology and geology of the rift as well as the rift rates, scale and opening in time. Together, this supports that the evolution of the Corinth Rift results from the stress and

deformation fields associated with the westward propagating tip of the North Anatolian Fault during the birth of the Aegean-Anatolian microplate.

Acknowledgements

Bathymetric data was kindly provided by Dr. Dimitris Sakellariou. The research leading to these results received funding from the People Programme (Marie Curie Actions) of the European Union's Seventh Framework Programme under the ITN project ALerT (Grant FP7-PEOPLE-2013-ITN number 607996) and by the ISIS program of CNES.

References

- Ambraseys, N.N., Jackson, J.A., 1990. Seismicity and associated strain of central Greece between 1890 and 1988. *Geophys. J. Int.* 101, 663–708.
- Anders, M.H., Schlische, R.W., 1994. Overlapping Faults, Intrabasin Highs, and the Growth of Normal Faults. *J. Geol.* 102, 165–179. doi:10.1086/629661
- Anderson, R.S., Densmore, A.L., Ellis, M.A., 1999. The generation and degradation of marine terraces. *Basin Res.* 11, 7–19.
- Armijo, R., Flerit, F., King, G., Meyer, B., 2004. Linear elastic fracture mechanics explains the past and present evolution of the Aegean. *Earth Planet. Sci. Lett.* 217, 85–95. doi:10.1016/S0012-821X(03)00590-9
- Armijo, R., Lacassin, R., Coudurier-Curveur, A., Carrizo, D., 2015. Coupled tectonic evolution of Andean orogeny and global climate. *Earth-Sci. Rev.* 143, 1–35.
- Armijo, R., Lyon-Caen, H., Papanastassiou, D., 1991. A possible normal-fault rupture for the 464 BC Sparta earthquake. *Nature* 351, 137–139. doi:10.1038/351137a0
- Armijo, R., Meyer, B., Hubert, A., Barka, A., 1999. Westward propagation of the North Anatolian fault into the northern Aegean: Timing and kinematics. *Geology* 27, 267. doi:10.1130/0091-7613(1999)027<0267:wpotna>2.3.co;2
- Armijo, R., Meyer, B., King, G.C.P., Rigo, A., Papanastassiou, D., 1996. Quaternary evolution of the Corinth Rift and its implications for the Late Cenozoic evolution of the Aegean. *Geophysical Journal International* 126, 11–53. doi:10.1111/j.1365-246x.1996.tb05264.x
- Armijo, R., Tapponnier, P., Mercier, J.L., Han, T.-L., 1986. Quaternary extension in southern Tibet: Field observations and tectonic implications. *J. Geophys. Res.* 91, 13803–13872. doi:10.1029/JB091iB14p13803
- Attal, M., Tucker, G.E., Whittaker, A.C., Cowie, P.A., Roberts, G.P., 2008. Modeling fluvial incision and transient landscape evolution: Influence of dynamic channel adjustment. *J. Geophys. Res.* 113, F02010. doi:10.1029/2007JF000893
- Avallone, A., Briole, P., Agatza-Balodimou, A.M., Billiris, H., Charade, O., Mitsakaki, C., Necessian, A., Papazissi, K., Paradissis, D., Veis, G., 2004. Analysis of eleven years of deformation measured by GPS in the Corinth Rift Laboratory area. *C. R. Geosci.* 336, 301–311. doi:10.1016/j.crte.2003.12.007
- Barbier, F., Duvergé, J., Le Pichon, X., 1986. Structure profonde de la marge Nord-Gascogne. Implications sur le mécanisme de rifting et de formation de la marge continentale. *Bull. Cent. Rech. Explor. Prod. Elf Aquitaine* 10, 105–121.

- Beckers, A., Hubert-Ferrari, A., Beck, C., Bodeux, S., Tripsanas, E., Sakellariou, D., De Batist, M., 2015. Active faulting at the western tip of the Gulf of Corinth, Greece, from high-resolution seismic data. *Mar. Geol.* 360, 55–69. doi:10.1016/j.margeo.2014.12.003
- Bell, R.E., Duclaux, G., Nixon, C.W., Gawthorpe, R.L., McNeill, L.C., 2017. High-angle, not low-angle, normal faults dominate early rift extension in the Corinth Rift, central Greece. *Geology*. doi:10.1130/g39560.1
- Bell, R.E., McNeill, L.C., Bull, J.M., Henstock, T.J., 2008. Evolution of the offshore western Gulf of Corinth. *Geol. Soc. Am. Bull.* 120, 156–178. doi:10.1130/B26212.1
- Bell, R.E., McNeill, L.C., Bull, J.M., Henstock, T.J., Collier, R.E.L., Leederz, M.R., 2009. Fault architecture, basin structure and evolution of the Gulf of Corinth Rift, central Greece. *Basin Res.* 21, 824–855. doi:10.1111/j.1365-2117.2009.00401.x
- Bell, R.E., McNeill, L.C., Henstock, T.J., Bull, J.M., 2011. Comparing extension on multiple time and depth scales in the Corinth Rift, Central Greece: Extension across the Corinth Rift. *Geophys. J. Int.* 186, 463–470. doi:10.1111/j.1365-246X.2011.05077.x
- Benedetti, L., Finkel, R., King, G., Armijo, R., Papanastassiou, D., Ryerson, F.J., Flerit, F., Farber, D., Stavrakakis, G., 2003. Motion on the Kaparelli fault (Greece) prior to the 1981 earthquake sequence determined from ³⁶Cl cosmogenic dating. *Terra Nova* 15, 118–124. doi:10.1046/j.1365-3121.2003.00474.x
- Berlin, M.M., Anderson, R.S., 2007. Modeling of knickpoint retreat on the Roan Plateau, western Colorado. *J. Geophys. Res.* 112, F03S06. doi:10.1029/2006JF000553
- Bernard, P., Lyon-Caen, H., Briole, P., Deschamps, A., Boudin, F., Makropoulos, K., Papadimitriou, P., Lemeille, F., Patau, G., Billiris, H., Paradissis, D., Papazissi, K., Castarède, H., Charade, O., Necessian, A., Avallone, A., Pacchiani, F., Zahradnik, J., Sacks, S., Linde, A., 2006. Seismicity, deformation and seismic hazard in the western rift of Corinth: New insights from the Corinth Rift Laboratory (CRL). *Tectonophysics* 426, 7–30. doi:10.1016/j.tecto.2006.02.012
- Boiselet, A., Scotti, O., Lyon-Caen, H., 2014. Estimating the probability of occurrence of earthquakes ($M > 6$) in the Western part of the Corinth rift using fault-based and classical seismotectonic approaches, EGU General Assembly Conference Abstracts.
- Boulton, S.J., Whittaker, A.C., 2009. Quantifying the slip rates, spatial distribution and evolution of active normal faults from geomorphic analysis: Field examples from an oblique-extensional graben, southern Turkey. *Geomorphology* 104, 299–316. doi:10.1016/j.geomorph.2008.09.007
- Briole, P., Rigo, A., Lyon-Caen, H., Ruegg, J.C., Papazissi, K., Mitsakaki, C., Balodimou, A., Veis, G., Hatzfeld, D., Deschamps, A., 2000. Active deformation of the Corinth rift, Greece- Results from repeated Global Positioning System surveys between 1990 and 1995. *Journal of Geophysical Research: Solid Earth* 105, 25605–25625. doi:10.1029/2000jb900148
- Brooks, M., Ferentinos, G., 1984. Tectonics and sedimentation in the Gulf of Corinth and the Zakynthos and Kefallinia channels, Western Greece. *Tectonophysics* 101, 25–54. doi:10.1016/0040-1951(84)90040-4
- Brun, J.P., 1999. Narrow rifts versus wide rifts: inferences for the mechanics of rifting from laboratory experiments. *Philosophical Transactions of the Royal Society of London A: Mathematical, Physical and Engineering Sciences* 357, 695–709. doi:10.1098/rsta.1999.0349
- Brun, J.-P., Faccenna, C., Gueydan, F., Sokoutis, D., Philippon, M., Kydonakis, K., Gorini, C., 2016. The two-stage Aegean extension, from localized to distributed, a result of slab rollback acceleration. *Can. J. Earth Sci.* 53, 1142–1157. doi:10.1139/cjes-2015-0203
- Brun, J.-P., Sokoutis, D., 2010. 45 m.y. of Aegean crust and mantle flow driven by trench retreat. *Geology* 38, 815–818. doi:10.1130/G30950.1
- Buck, W.R., 1991. Modes of continental lithospheric extension. *J. Geophys. Res.* 96, 20161–20178.
- Buck, W.R., 1993. Effect of lithospheric thickness on the formation of high- and low-angle normal faults. *Geology* 21, 933–936. doi:10.1130/0091-7613(1993)021<0933:EOLTOT>2.3.CO;2
- Bürgmann, R., Dresen, G., 2008. Rheology of the Lower Crust and Upper Mantle: Evidence from Rock Mechanics, Geodesy, and Field Observations. *Annu. Rev. Earth Planet. Sci.* 36, 531–567. doi:10.1146/annurev.earth.36.031207.124326
- Burov, E.B., Diament, M., 1995. The effective elastic thickness (T_e) of continental lithosphere: What does it really mean? *J. Geophys. Res. [Solid Earth]* 100, 3905–3927.
- Burov, E.B., Watts, A.B., Others, 2006. The long-term strength of continental lithosphere: “jelly sandwich” or “crème brûlée”? *GSA Today* 16, 4.
- Cailleux, A., 1958. Etude quantitative de failles. *Rev. Géomorphologie Dynamique* 9, 129–145.
- Cartwright, J.A., Trudgill, B.D., Mansfield, C.S., 1995. Fault growth by segment linkage: an explanation for

- scatter in maximum displacement and trace length data from the Canyonlands Grabens of SE Utah. *J. Struct. Geol.* 17, 1319–1326. doi:10.1016/0191-8141(95)00033-A
- Charalampakis, M., Lykousis, V., Sakellariou, D., Papatheodorou, G., Ferentinos, G., 2014. The tectono-sedimentary evolution of the Lechaion Gulf, the south eastern branch of the Corinth graben, Greece. *Mar. Geol.* 351, 58–75. doi:10.1016/j.margeo.2014.03.014
- Clendenon, C., 2009. Karst hydrology in ancient myths from Arcadia and Argolis, Greece. *Acta Carsologica* 38.
- Collier, R., Dart, C., 1991. Neogene to Quaternary rifting, sedimentation and uplift in the Corinth Basin, Greece. *J. Geol. Soc. London* 148, 1049–1065. doi:10.1144/gsjgs.148.6.1049
- Collier, R.E.L., 1990. Eustatic and tectonic controls upon Quaternary coastal sedimentation in the Corinth Basin, Greece. *J. Geol. Soc. London* 147, 301–314. doi:10.1144/gsjgs.147.2.0301
- Collier, R.E.L., Leeder, M.R., Rowe, P.J., Atkinson, T.C., 1992. Rates of tectonic uplift in the Corinth and Megara Basins, central Greece. *Tectonics* 11, 1159–1167. doi:10.1029/92TC01565
- Cornet, F.H., Doan, M.L., Moretti, I., Borm, G., 2004. Drilling through the active Aigion Fault: the AIG10 well observatory. *C. R. Geosci.* 336, 395–406. doi:10.1016/j.crte.2004.02.002
- Cowie, P.A., 1998. A healing–reloading feedback control on the growth rate of seismogenic faults. *J. Struct. Geol.* 20, 1075–1087. doi:10.1016/S0191-8141(98)00034-0
- Cowie, P.A., Attal, M., Tucker, G.E., Whittaker, A.C., Naylor, M., Ganas, A., Roberts, G.P., 2006. Investigating the surface process response to fault interaction and linkage using a numerical modelling approach. *Basin Res.* 18, 231–266. doi:10.1111/j.1365-2117.2006.00298.x
- Cowie, P.A., Gupta, S., Dawers, N.H., 2000. Implications of fault array evolution for synrift depocentre development: insights from a numerical fault growth model. *Basin Res.* 12, 241–261.
- Cowie, P.A., Roberts, G.P., 2001. Constraining slip rates and spacings for active normal faults. *J. Struct. Geol.* 23, 1901–1915. doi:10.1016/S0191-8141(01)00036-0
- Cowie, P.A., Scholz, C.H., 1992a. Physical explanation for the displacement-length relationship of faults using a post-yield fracture mechanics model. *J. Struct. Geol.* 14, 1133–1148. doi:10.1016/0191-8141(92)90065-5
- Cowie, P.A., Scholz, C.H., 1992b. Displacement-length scaling relationship for faults: data synthesis and discussion. *J. Struct. Geol.* 14, 1149–1156. doi:10.1016/0191-8141(92)90066-6
- Dawers, N.H., Anders, M.H., 1995. Displacement-length scaling and fault linkage. *J. Struct. Geol.* 17, 607–614. doi:10.1016/0191-8141(94)00091-d
- Dawers, N.H., Anders, M.H., Scholz, C.H., 1993. Growth of normal faults: Displacement-length scaling. *Geology* 21, 1107–1110. doi:10.1130/0091-7613(1993)021<1107:GONFDL>2.3.CO;2
- De Gelder, G., Fernández-Blanco, D., Melnick, D., Duclaux, G., Bell, R., Jara-Muñoz, J., Armijo, R., Lacassin, R., 2018. Lithospheric flexure and rheology determined by climate cycle markers in the Corinth Rift. *Earth ArXiv*. doi:10.31223/osf.io/4sh8e
- De Martini, P.M., Pantosti, D., Palyvos, N., Lemeille, F., McNeill, L., Collier, R., 2004. Slip rates of the Aigion and Eliki Faults from uplifted marine terraces, Corinth Gulf, Greece. *C. R. Geosci.* 336, 325–334. doi:10.1016/j.crte.2003.12.006
- Densmore, A.L., Dawers, N.H., Gupta, S., Guidon, R., 2005. What sets topographic relief in extensional footwalls? *Geology* 33, 453–456. doi:10.1130/G21440.1
- Densmore, A.L., Dawers, N.H., Gupta, S., Guidon, R., Goldin, T., 2004. Footwall topographic development during continental extension. *J. Geophys. Res.* 109, F03001. doi:10.1029/2003JF000115
- Densmore, A.L., Gupta, S., Allen, P.A., Dawers, N.H., 2007. Transient landscapes at fault tips. *J. Geophys. Res.* 112, F03S08. doi:10.1029/2006JF000560
- DiBiase, R.A., Whipple, K.X., Heimsath, A.M., Ouimet, W.B., 2010. Landscape form and millennial erosion rates in the San Gabriel Mountains, CA. *Earth Planet. Sci. Lett.* 289, 134–144. doi:10.1016/j.epsl.2009.10.036
- Doutsos, T., Piper, D.J.W., 1990. Listric faulting, sedimentation, and morphological evolution of the Quaternary eastern Corinth rift, Greece: First stages of continental rifting. *Geol. Soc. Am. Bull.* 102, 812–829. doi:10.1130/0016-7606(1990)102<0812:LFSAME>2.3.CO;2
- Duverger, C., Godano, M., Bernard, P., Lyon-Caen, H., Lambotte, S., 2015. The 2003–2004 seismic swarm in the western Corinth rift: Evidence for a multiscale pore pressure diffusion process along a permeable fault system. *Geophys. Res. Lett.* 42, 2015GL065298. doi:10.1002/2015GL065298
- Duverger, C., Lambotte, S., Bernard, P., Lyon-Caen, H., Deschamps, A., Necessian, A., 2018. Dynamics of microseismicity and its relationship with the active structures in the western Corinth Rift (Greece). *Geophys. J. Int.* 215, 196–221. doi:10.1093/gji/ggy264

- Elias, P., Kontoes, C., Papoutsis, I., Kotsis, I., Marinou, A., Paradissis, D., Sakellariou, D., 2009. Permanent Scatterer InSAR Analysis and Validation in the Gulf of Corinth. *Sensors* 9, 46–55. doi:10.3390/s90100046
- Ferentinos, G., Georgiou, N., Christodoulou, D., Geraga, M., Papatheodorou, G., 2018. Propagation and termination of a strike slip fault in an extensional domain: The westward growth of the North Anatolian Fault into the Aegean Sea. *Tectonophysics* 745, 183–195. doi:10.1016/j.tecto.2018.08.003
- Fernández-Blanco, D., de Gelder, G., Gallen, S., Lacassin, R., Armijo, R., 2019a. Evolving Flexure Recorded in Continental Rift Uplifting Landscapes - Corinth Rift, Greece. Retrieved from EarthArXiv, January 10, 2019. doi:10.31223/osf.io/e6dp5
- Fernández-Blanco, D., de Gelder, G., Gallen, S., Lacassin, R., Armijo, R., 2019b. Transient rivers characterize evolving crustal-scale flexure in the Corinth Rift. Retrieved from EarthArXiv, January 10, 2019. doi:10.31223/osf.io/8w7kf
- Flerit, F., Armijo, R., King, G., Meyer, B., 2004. The mechanical interaction between the propagating North Anatolian Fault and the back-arc extension in the Aegean. *Earth Planet. Sci. Lett.* 224, 347–362. doi:10.1016/j.epsl.2004.05.028
- Ford, M., Hemelsdaël, R., Mancini, M., Palyvos, N., 2016. Rift migration and lateral propagation: evolution of normal faults and sediment-routing systems of the western Corinth rift (Greece). *Geological Society, London, Special Publications* 439. doi:10.1144/SP439.15
- Ford, M., Rohais, S., Williams, E.A., Bourlange, S., Joussetin, D., Backert, N., Malartre, F., 2012. Tectono-sedimentary evolution of the western Corinth rift (Central Greece). *Basin Res.* 0, 1–23. doi:10.1111/j.1365-2117.2012.00550.x
- Ford, M., Williams, E.A., Malartre, F., Popescu, S.-M., 2009. Stratigraphic architecture, sedimentology and structure of the Vouraikos Gilbert-type fan delta, Gulf of Corinth, Greece. *Sedimentary processes, environments and basins: A tribute to Peter Friend: Oxford, Blackwell Publishing Ltd* 49–90.
- Gallen, S.F., Wegmann, K.W., 2017. River profile response to normal fault growth and linkage: An example from the Hellenic forearc of south-central Crete, Greece. *Earth Surface Dynamics* 5, 161. doi:10.5194/esurf-5-161-2017
- Gawthorpe, R.L., Andrews, J.E., Collier, R.E.L., Ford, M., Henstra, G.A., Kranis, H., Leeder, M.R., Muravchik, M., Skourtsos, E., 2017a. Building up or out? Disparate sequence architectures along an active rift margin—Corinth rift, Greece. *Geology* 45, 1111–1114. doi:10.1130/G39660.1
- Gawthorpe, R.L., Fraser, A.J., Collier, R., 1994. Sequence stratigraphy in active extensional basins: implications for the interpretation of ancient basin-fills. *Mar. Pet. Geol.*
- Gawthorpe, R.L., Fraser, A.J., Collier, R.E.L., 1994. Sequence stratigraphy in active extensional basins: implications for the interpretation of ancient basin-fills. *Mar. Pet. Geol.* 11, 642–658. doi:10.1016/0264-8172(94)90021-3
- Gawthorpe, R.L., Jackson, C.A.-L., Young, M.J., Sharp, I.R., Moustafa, A.R., Leppard, C.W., 2003. Normal fault growth, displacement localisation and the evolution of normal fault populations: the Hammam Faraun fault block, Suez rift, Egypt. *J. Struct. Geol.* 25, 883–895. doi:10.1016/S0191-8141(02)00088-3
- Gawthorpe, R.L., Leeder, M., Kranis, H., Skourtsos, E., Andrews, J., Henstra, G., Mack, G., Muravchik, M., Turner, J., Stamatakis, M., 2017b. Tectono-sedimentary evolution of the Plio-Pleistocene Corinth rift, Greece. *Basin Res.*
- Gilbert, G.K., 1890. *Lake Bonneville*. US Government Printing Office.
- Godano, M., Deschamps, A., Lambotte, S., Lyon-Caen, H., Bernard, P., Pacchiani, F., 2014. Focal mechanisms of earthquake multiplets in the western part of the Corinth Rift (Greece): influence of the velocity model and constraints on the geometry of the active faults. *Geophys. J. Int.* 197, 1660–1680. doi:10.1093/gji/ggu059
- Goldsworthy, M., Jackson, J., 2001. Migration of activity within normal fault systems: examples from the Quaternary of mainland Greece. *J. Struct. Geol.* 23, 489–506.
- Goldsworthy, M., Jackson, J., Haines, J., 2002. The continuity of active fault systems in Greece. *Geophys. J. Int.* 148, 596–618. doi:10.1046/j.1365-246x.2002.01609.x
- Gupta, A., Scholz, C.H., 2000. A model of normal fault interaction based on observations and theory. *J. Struct. Geol.* 22, 865–879. doi:10.1016/s0191-8141(00)00011-0
- Hatzfeld, D., Karakostas, V., Ziazia, M., Kassaras, I., Papadimitriou, E., Makropoulos, K., Voulgaris, N., Papaioannou, C., 2000. Microseismicity and faulting geometry in the Gulf of Corinth (Greece). *Geophys. J. Int.* 141, 438–456. doi:10.1046/j.1365-246x.2000.00092.x
- Heezen, B.C., Ewing, M., Johnson, G.L., 1966. The Gulf of Corinth floor. *Deep Sea Research and Oceanographic*

- Abstracts 13, 381–411. doi:10.1016/0011-7471(66)91076-X
- Hemelsdaël, R., Ford, M., 2016. Relay zone evolution: a history of repeated fault propagation and linkage, central Corinth rift, Greece. *Basin Res.* 28, 34–56. doi:10.1111/bre.12101
- Houghton, S.L., Roberts, G.P., Papanikolaou, I.D., McArthur, J.M., Gilmour, M.A., 2003. New 234U-230Th coral dates from the western Gulf of Corinth: Implications for extensional tectonics. *Geophys. Res. Lett.* 30, 2013. doi:10.1029/2003GL018112
- Houseman, G., England, P., 1986. A dynamical model of lithosphere extension and sedimentary basin formation. *J. Geophys. Res.*
- Howard, A.D., 1994. A detachment-limited model of drainage basin evolution. *Water Resour. Res.* 30, 2261–2285.
- Hubert, A., 1996. Fault re-activation, stress interaction and rupture propagation of the 1981 Corinth earthquake sequence. *Earth Planet. Sci. Lett.* 142, 573–585. doi:10.1016/0012-821x(96)00108-2
- Hubert, A., King, G., Armijo, R., Meyer, B., Papanastasiou, D., 1996. Fault re-activation, stress interaction and rupture propagation of the 1981 Corinth earthquake sequence. *Earth Planet. Sci. Lett.* 142, 573–585. doi:10.1016/0012-821X(96)00108-2
- Hubert-Ferrari, A., King, G., Manighetti, I., Armijo, R., Meyer, B., Tapponnier, P., 2003. Long-term elasticity in the continental lithosphere; modelling the Aden Ridge propagation and the Anatolian extrusion process. *Geophys. J. Int.* 153, 111–132. doi:10.1046/j.1365-246x.2003.01872.x
- Huguen, C., Mascle, J., Chaumillon, E., Kopf, A., Woodside, J., Zitter, T., 2004. Structural setting and tectonic control of mud volcanoes from the Central Mediterranean Ridge (Eastern Mediterranean). *Marine Geology* 209, 245–263. doi:10.1016/j.margeo.2004.05.002
- Jackson, J.A., Gagnepain, J., Houseman, G., King, G.C.P., Papadimitriou, P., Soufleris, C., Virieux, J., 1982. Seismicity, normal faulting, and the geomorphological development of the Gulf of Corinth (Greece): the Corinth earthquakes of February and March 1981. *Earth Planet. Sci. Lett.* 57, 377–397. doi:10.1016/0012-821X(82)90158-3
- Jolivet, L., Brun, J.-P., 2010. Cenozoic geodynamic evolution of the Aegean. *Int. J. Earth Sci.* 99, 109–138. doi:10.1007/s00531-008-0366-4
- Jolivet, L., Faccenna, C., Huet, B., Labrousse, L., Le Pourhiet, L., Lacombe, O., Lecomte, E., Burov, E., Denèle, Y., Brun, J.-P., Philippon, M., Paul, A., Salaün, G., Karabulut, H., Piromallo, C., Monié, P., Gueydan, F., Okay, A.I., Oberhänsli, R., Pourteau, A., Augier, R., Gadenne, L., Driussi, O., 2013. Aegean tectonics: Strain localisation, slab tearing and trench retreat. *Tectonophysics* 597–598, 1–33. doi:10.1016/j.tecto.2012.06.011
- Jolivet, L., Labrousse, L., Agard, P., Lacombe, O., Bailly, V., Lecomte, E., Mouthereau, F., Mehl, C., 2010. Rifting and shallow-dipping detachments, clues from the Corinth Rift and the Aegean. *Tectonophysics* 483, 287–304. doi:10.1016/j.tecto.2009.11.001
- Karymbalis, E., Ferentinou, M., Giles, P.T., 2016a. Use of morphometric variables and self-organizing maps to identify clusters of alluvial fans and catchments in the north Peloponnese, Greece. *Geological Society, London, Special Publications* 440. doi:10.1144/SP440.7
- Karymbalis, E., Papanastassiou, D., Gaki-Papanastassiou, K., Ferentinou, M., Chalkias, C., 2016b. Late Quaternary rates of stream incision in Northeast Peloponnese, Greece. *Front. Earth Sci.* 10, 455–478. doi:10.1007/s11707-016-0577-0
- Kent, E., Boulton, S.J., Whittaker, A.C., Stewart, I.S., Cihat Alçiçek, M., 2016. Normal fault growth and linkage in the Gediz (Alaşehir) Graben, Western Turkey, revealed by transient river long-profiles and slope-break knickpoints. *Earth Surf. Processes Landforms*. doi:10.1002/esp.4049
- Keraudren, B., Sorel, D., 1987. The terraces of Corinth (Greece) — A detailed record of eustatic sea-level variations during the last 500,000 years. *Mar. Geol.* 77, 99–107. doi:10.1016/0025-3227(87)90085-5
- Kilias, A., Falalakis, G., Sfeikos, A., Papadimitriou, E., Vamvaka, A., Gkarlaoui, C., 2013. The Thrace basin in the Rhodope province of NE Greece—A tertiary supradetachment basin and its geodynamic implications. *Tectonophysics* 595, 90–105.
- King, G., Ellis, M., 1990. The origin of large local uplift in extensional regions. *Nature* 348, 689–693.
- King, G., Stein, R., Rundle, J., 1988. The Growth of Geological Structures by Repeated Earthquakes 1. Conceptual Framework. *Journal of Geophysical Research: Solid Earth* 93, 13307–13318. doi:10.1029/jb093ib11p13307
- Klinger, Y., Avouac, J.P., Abou Karaki, N., Dorbath, L., Bourles, D., Reyss, J.L., 2000. Slip rate on the Dead Sea transform fault in northern Araba valley (Jordan). *Geophys. J. Int.* 142, 755–768. doi:10.1046/j.1365-

- 246x.2000.00165.x
- Koukouvelas, I.K., Aydin, A., 2002. Fault structure and related basins of the North Aegean Sea and its surroundings. *Tectonics* 21, 1046. doi:10.1029/2001TC901037
- Koukouvelas, I.K., Stamatopoulos, L., Katsonopoulou, D., Pavlides, S., 2001. A palaeoseismological and geoarchaeological investigation of the Eliki fault, Gulf of Corinth, Greece. *J. Struct. Geol.* 23, 531–543. doi:10.1016/S0191-8141(00)00124-3
- Kreemer, C., Chamot-Rooke, N., 2004. Contemporary kinematics of the southern Aegean and the Mediterranean Ridge. *Geophysical Journal International* 157, 1377–1392. doi:10.1111/j.1365-246X.2004.02270.x
- Kusznir, N.J., Marsden, G., Egan, S.S., 1991. A flexural-cantilever simple-shear/pure-shear model of continental lithosphere extension: applications to the Jeanne d'Arc Basin, Grand Banks and Viking Graben, North Sea. *Geological Society, London, Special Publications* 56, 41–60.
- Kusznir, N.J., Park, R.G., 1986. Continental lithosphere strength: the critical role of lower crustal deformation. *Geological Society, London, Special Publications* 24, 79–93. doi:10.1144/GSL.SP.1986.024.01.09
- Lacassin, R., Arnaud, N., Leloup, P.H., Armijo, R., Meyer, B., 2007. Syn- and post-orogenic exhumation of metamorphic rocks in North Aegean. *eEarth* 2, 51–63. doi:10.5194/ee-2-51-2007
- Lajoie, K.R., 1986. Coastal tectonics. *Active tectonics* 95–124.
- Lambotte, S., Lyon-Caen, H., Bernard, P., Deschamps, A., Patau, G., Nercessian, A., Pacchiani, F., Bourouis, S., Drilleau, M., Adamova, P., 2014. Reassessment of the rifting process in the Western Corinth Rift from relocated seismicity. *Geophys. J. Int.* 197, 1822–1844. doi:10.1093/gji/ggu096
- Leeder, M.R., Mack, G.H., Brasier, A.T., Parrish, R.R., McIntosh, W.C., Andrews, J.E., Duermeijer, C.E., 2008. Late-Pliocene timing of Corinth (Greece) rift-margin fault migration. *Earth Planet. Sci. Lett.* 274, 132–141. doi:10.1016/j.epsl.2008.07.006
- Leeder, M.R., Mark, D.F., Gawthorpe, R.L., Kranis, H., Loveless, S., Pedentchouk, N., Skourtsos, E., Turner, J., Andrews, J.E., Stamatakis, M., 2012. A “Great Deepening”: Chronology of rift climax, Corinth rift, Greece. *Geology* 40, 999–1002. doi:10.1130/G33360.1
- Leeder, M.R., McNeill, L.C., Ll Collier, R.E., Portman, C., Rowe, P.J., Andrews, J.E., Gawthorpe, R.L., 2003. Corinth rift margin uplift: New evidence from Late Quaternary marine shorelines. *Geophysical Research Letters* 30, 1611. doi:10.1029/2003GL017382
- Leeder, M.R., Seger, M.J., Stark, C.P., 1991. Sedimentation and tectonic geomorphology adjacent to major active and inactive normal faults, southern Greece. *J. Geol. Soc. London* 148, 331–343. doi:10.1144/gsjgs.148.2.0331
- Le Pichon, X., Angelier, J., 1981. The Aegean Sea. *Philosophical Transactions of the Royal Society of London A: Mathematical, Physical and Engineering Sciences* 300, 357–372.
- Le Pichon, X., Kreemer, C., 2010. The Miocene-to-Present Kinematic Evolution of the Eastern Mediterranean and Middle East and Its Implications for Dynamics. *Annu. Rev. Earth Planet. Sci.* 38, 323–351. doi:10.1146/annurev-earth-040809-152419
- Lykousis, V., Sakellariou, D., Moretti, I., Kaberi, H., 2007. Late Quaternary basin evolution of the Gulf of Corinth: Sequence stratigraphy, sedimentation, fault-slip and subsidence rates. *Tectonophysics* 440, 29–51. doi:10.1016/j.tecto.2006.11.007
- Malartre, F., Ford, M., Williams, E.A., 2004. Preliminary biostratigraphy and 3D geometry of the Vouraikos Gilbert-type fan delta, Gulf of Corinth, Greece. *C. R. Geosci.* 336, 269–280. doi:10.1016/j.crte.2003.11.016
- Manighetti, I., Campillo, M., Sammis, C., Mai, P.M., King, G., 2005. Evidence for self-similar, triangular slip distributions on earthquakes: Implications for earthquake and fault mechanics. *J. Geophys. Res.* 110, B05302. doi:10.1029/2004JB003174
- Manighetti, I., King, G.C.P., Gaudemer, Y., Scholz, C.H., Doubre, C., 2001. Slip accumulation and lateral propagation of active normal faults in Afar. *J. Geophys. Res.* 106, 13667–13696. doi:10.1029/2000JB900471
- Masson-Delmotte, V., Stenni, B., Pol, K., Braconnot, P., Cattani, O., Falourd, S., Kageyama, M., Jouzel, J., Landais, A., Minster, B., Barnola, J.M., Chappellaz, J., Krinner, G., Johnsen, S., Röthlisberger, R., Hansen, J., Mikolajewicz, U., Otto-Bliesner, B., 2010. EPICA Dome C record of glacial and interglacial intensities. *Quat. Sci. Rev.* 29, 113–128. doi:10.1016/j.quascirev.2009.09.030
- McKenzie, D., 1978. Active tectonics of the Alpine—Himalayan belt: the Aegean Sea and surrounding regions. *Geophys. J. Int.*
- McKenzie, D., 1978a. Some remarks on the development of sedimentary basins. *Earth and Planetary Science*

- Letters 40, 25–32. doi:10.1016/0012-821X(78)90071-7
- McKenzie, D., 1978b. Active tectonics of the Alpine-Himalayan belt: the Aegean Sea and surrounding regions. *Geophysical Journal* 55, 217–254. doi:10.1111/j.1365-246X.1978.tb04759.x
- McNeill, L.C., Collier, R.E.L., 2004. Uplift and slip rates of the eastern Eliki fault segment, Gulf of Corinth, Greece, inferred from Holocene and Pleistocene terraces. *J. Geol. Soc. London* 161, 81–92. doi:10.1144/0016-764903-029
- McNeill, L.C., Cotterill, C.J., Henstock, T.J., Bull, J.M., Stefatos, A., Collier, R.E.L., Papatheoderou, G., Ferentinos, G., Hicks, S.E., 2005. Active faulting within the offshore western Gulf of Corinth, Greece: Implications for models of continental rift deformation. *Geology* 33, 241–244. doi:10.1130/G21127.1
- McNeill, L., Shillington, D., Carter, G., Everest, J., Green, S., 381 Scientists, E., 2018. Preliminary results from IODP Expedition 381: Development of the active Corinth Rift, Greece, EGU General Assembly Conference Abstracts. adsabs.harvard.edu.
- Mechernich, S., Schneiderwind, S., Mason, J., Papanikolaou, I.D., Deligiannakis, G., Pallikarakis, A., Binnie, S.A., Dunai, T.J., Reicherter, K., 2018. The Seismic History of the Pisia Fault (Eastern Corinth Rift, Greece) From Fault Plane Weathering Features and Cosmogenic ³⁶Cl Dating. *J. Geophys. Res. [Solid Earth]* 123, 4266–4284. doi:10.1029/2017JB014600
- Moretti, I., Lykousis, V., Sakellariou, D., Reynaud, J.-Y., Benziane, B., Prinzhofer, A., 2004. Sedimentation and subsidence rate in the Gulf of Corinth: what we learn from the Marion Dufresne’s long-piston coring. *C. R. Geosci.* 336, 291–299. doi:10.1016/j.crte.2003.11.011
- Müller, R.D., Sdrolias, M., Gaina, C., Roest, W.R., 2008. Age, spreading rates, and spreading asymmetry of the world’s ocean crust. *Geochem. Geophys. Geosyst.* 9, Q04006. doi:10.1029/2007GC001743
- Nicol, A., Watterson, J., Walsh, J.J., Childs, C., 1996. The shapes, major axis orientations and displacement patterns of fault surfaces. *J. Struct. Geol.* 18, 235–248. doi:10.1016/S0191-8141(96)80047-2
- Nixon, C.W., McNeill, L.C., Bull, J.M., Bell, R.E., Gawthorpe, R.L., Henstock, T.J., Christodoulou, D., Ford, M., Taylor, B., Sakellariou, D., Ferentinos, G., Papatheodorou, G., Leeder, M.R., Collier, R.E.L., Goodliffe, A.M., Sachpazi, M., Kranis, H., 2016. Rapid spatiotemporal variations in rift structure during development of the Corinth Rift, central Greece. *Tectonics* 35, 2015TC004026. doi:10.1002/2015TC004026
- Ori, G.G., 1989. Geologic history of the extensional basin of the Gulf of Corinth (?Miocene-Pleistocene), Greece. *Geology* 17, 918–921. doi:10.1130/0091-7613(1989)017<0918:GHOTEB>2.3.CO;2
- Palyvos, N., Lemeille, F., Sorel, D., Pantosti, D., Pavlopoulos, K., 2008. Geomorphic and biological indicators of paleoseismicity and Holocene uplift rate at a coastal normal fault footwall (western Corinth Gulf, Greece). *Geomorphology* 96, 16–38. doi:10.1016/j.geomorph.2007.07.010
- Palyvos, N., Pantosti, D., De Martini, P.M., Lemeille, F., Sorel, D., Pavlopoulos, K., 2005. The Aigion–Neos Erineos coastal normal fault system (western Corinth Gulf Rift, Greece): Geomorphological signature, recent earthquake history, and evolution. *J. Geophys. Res.* 110, B09302. doi:10.1029/2004JB003165
- Palyvos, N., Pantosti, D., Zabczi, C., D’Addezio, G., 2007. Paleoseismological Evidence of Recent Earthquakes on the 1967 Mudurnu Valley Earthquake Segment of the North Anatolian Fault Zone. *Bull. Seismol. Soc. Am.* 97, 1646–1661. doi:10.1785/0120060049
- Pantosti, D., De Martini, P.M., Koukouvelas, I., Stamatopoulos, L., Palyvos, N., Pucci, S., Lemeille, F., Pavlides, S., 2004. Palaeoseismological investigations of the Aigion Fault (Gulf of Corinth, Greece). *C. R. Geosci.* 336, 335–342. doi:10.1016/j.crte.2003.12.005
- Papazachos, C., Kiratzi, A., Papazachos, B., 1992. Rates of active crustal deformation in the Aegean and the surrounding area. *Journal of Geodynamics* 16, 147–179. doi:10.1016/0264-3707(92)90024-M
- Pavlides, S.B., Koukouvelas, I.K., Kokkalas, S., Stamatopoulos, L., Keramydas, D., Tsodoulos, I., 2004. Late Holocene evolution of the East Eliki fault, Gulf of Corinth (Central Greece). *Quaternary International* 115–116, 139–154. doi:10.1016/S1040-6182(03)00103-4
- Pearce, F.D. (Frederick D.), 2015. Seismic imaging of the western Hellenic subduction zone : the relationship between slab composition, retreat rate, and overriding lithosphere genesis. Massachusetts Institute of Technology.
- Reilinger, R., McClusky, S., Paradissis, D., Ergintav, S., Vernant, P., 2009. Geodetic constraints on the tectonic evolution of the Aegean region and strain accumulation along the Hellenic subduction zone. *Tectonophysics* 488, 22–30. doi:10.1016/j.tecto.2009.05.027
- Resor, P.G., Pollard, D.D., 2012. Reverse drag revisited: Why footwall deformation may be the key to inferring listric fault geometry. *J. Struct. Geol.* 41, 98–109. doi:10.1016/j.jsg.2011.10.012
- Rietbrock, A., Tiberi, C., Scherbaum, F., Lyon-Caen, H., 1996. Seismic slip on a low angle normal fault in the

- Gulf of Corinth: Evidence from high-resolution cluster analysis of microearthquakes. *Geophysical Research Letters* 23, 1817–1820. doi:10.1029/96gl01257
- Rigo, A., Lyon-Caen, H., Armijo, R., Deschamps, A., Hatzfeld, D., Makropoulos, K., Papadimitriou, P., Kassaras, I., 1996. A microseismic study in the western part of the Gulf of Corinth (Greece): Implications for large-scale normal faulting mechanisms. *Geophys. J. Int.* 126, 663–688.
- Roberts, G.P., Houghton, S.L., Underwood, C., Papanikolaou, I., Cowie, P.A., van Calsteren, P., Wigley, T., Cooper, F.J., McArthur, J.M., 2009. Localization of Quaternary slip rates in an active rift in 10 5 years: An example from central Greece constrained by 234 U- 230 Th coral dates from uplifted paleoshorelines. *J. Geophys. Res.* 114, 393. doi:10.1029/2008JB005818
- Rohais, Joannin, Sébastien, Colin, J.-P., Suc, J.-P., Guillocheau, F., Eschard, R., 2007. Age and environmental evolution of the syn-rift fill of the southern coast of the gulf of Corinth (Akrata-Derveni region, Greece). *Bulletin de la Société Géologique de France* 178, 231–243. doi:10.2113/gssgfbull.178.3.231
- Rohais, S., Eschard, R., Ford, M., Guillocheau, F., Moretti, I., 2007. Stratigraphic architecture of the Plio-Pleistocene infill of the Corinth Rift: Implications for its structural evolution. *Tectonophysics* 440, 5–28. doi:10.1016/j.tecto.2006.11.006
- Rohais, S., Moretti, I., 2017. Structural and Stratigraphic Architecture of the Corinth Rift (Greece): An Integrated Onshore to Offshore Basin-Scale Synthesis, in: Roure, F., Amin, A.A., Khomsi, S., Al Garni, M.A.M. (Eds.), *Lithosphere Dynamics and Sedimentary Basins of the Arabian Plate and Surrounding Areas*, *Frontiers in Earth Sciences*. Springer International Publishing, pp. 89–120. doi:10.1007/978-3-319-44726-1_5
- Rosenbloom, N.A., Anderson, R.S., 1994. Hillslope and channel evolution in a marine terraced landscape, Santa Cruz, California. *J. Geophys. Res.* 99, 14013–14029. doi:10.1029/94JB00048
- Royden, L.H., Papanikolaou, D.J., 2011. Slab segmentation and late Cenozoic disruption of the Hellenic arc. *Geochem. Geophys. Geosyst.* 12, Q03010. doi:10.1029/2010GC003280
- Sachpazi, M., Clément, C., Laigle, M., Hirn, A., Roussos, N., 2003. Rift structure, evolution, and earthquakes in the Gulf of Corinth, from reflection seismic images. *Earth Planet. Sci. Lett.* 216, 243–257. doi:10.1016/S0012-821X(03)00503-X
- Sachpazi, M., Galvé, A., Laigle, M., Hirn, A., Sokos, E., Serpetsidaki, A., Marthelot, J.-M., Pi Alperin, J.M., Zelt, B., Taylor, B., 2007. Moho topography under central Greece and its compensation by Pn time-terms for the accurate location of hypocenters: The example of the Gulf of Corinth 1995 Aigion earthquake. *Tectonophysics* 440, 53–65. doi:10.1016/j.tecto.2007.01.009
- Sakellariou, D., Lykousis, V., Alexandri, S., Kaberi, H., Rousakis, G., Nomikou, P., Georgiou, P., Ballas, D., 2007. Faulting, seismic-stratigraphic architecture and Late Quaternary evolution of the Gulf of Alkyonides Basin–East Gulf of Corinth, Central Greece. *Basin Res.* 19, 273–295. doi:10.1111/j.1365-2117.2007.00322.x
- Sakellariou, D., Lykousis, V., Papanikolaou, D., 1998. Neotectonic structure and evolution of the gulf of Alkyonides, central Greece. *Bulletin of the Geologic Society of Greece* 32, 241–250.
- Schlische, R.W., Young, S.S., Ackermann, R.V., Gupta, A., 1996. Geometry and scaling relations of a population of very small rift-related normal faults. *Geology* 24, 683–686. doi:10.1130/0091-7613(1996)024<0683:GASROA>2.3.CO;2
- Scholz, C.H., 2002. *The Mechanics of Earthquakes and Faulting*, 2ed. Cambridge University Press.
- Schwanghart, W., Scherler, D., 2014. TopoToolbox 2 – MATLAB-based software for topographic analysis and modeling in Earth surface sciences. *Earth Surf. Dynam.* 2, 1–7. doi:10.5194/esurf-2-1-2014
- Scott, A.T., Pinter, N., 2003. Extraction of Coastal Terraces and Shoreline-Angle Elevations from Digital Terrain Models, Santa Cruz and Anacapa Islands, California. *Phys. Geogr.* 24, 271–294. doi:10.2747/0272-3646.24.4.271
- Seger, M., Alexander, J., 2009. Distribution of Plio-Pleistocene and Modern Coarse-Grained Deltas South of the Gulf of Corinth, Greece, in: Frostick, L.E. (Ed.), *Tectonic Controls and Signatures in Sedimentary Successions* (Special Publication 20 of the IAS). John Wiley & Sons, p. 37.
- Snyder, N.P., Whipple, K.X., Tucker, G.E., Merritts, D.J., 2000. Landscape response to tectonic forcing: Digital elevation model analysis of stream profiles in the Mendocino triple junction region, northern California. *Geol. Soc. Am. Bull.* 112, 1250–1263. doi:10.1130/0016-7606(2000)112<1250:LRTTFD>2.0.CO;2
- Sorel, D., 2000. A Pleistocene and still-active detachment fault and the origin of the Corinth-Patras rift, Greece. *Geology* 28, 83–86. doi:10.1130/0091-7613(2000)28<83:APASDF>2.0.CO;2

- Stefatos, A., Papatheodorou, G., Ferentinos, G., Leeder, M., Collier, R., 2002. Seismic reflection imaging of active offshore faults in the Gulf of Corinth: their seismotectonic significance. *Basin Research* 14, 487–502.
- Stewart, I., 1996. Holocene uplift and palaeoseismicity on the Eliki fault, Western Gulf of Corinth, Greece. *Annals of Geophysics* 39.
- Stewart, I., Vita-Finzi, C., 1996. Coastal uplift on active normal faults: the Eliki Fault, Greece. *Geophys. Res. Lett.*
- Taylor, B., Weiss, J.R., Goodliffe, A.M., Sachpazi, M., Laigle, M., Hirn, A., 2011. The structures, stratigraphy and evolution of the Gulf of Corinth rift, Greece: Structures, stratigraphy and evolution of GoC. *Geophys. J. Int.* 185, 1189–1219. doi:10.1111/j.1365-246X.2011.05014.x
- Tetreault, J.L., Buiter, S.J.H., 2018. The influence of extension rate and crustal rheology on the evolution of passive margins from rifting to break-up. *Tectonophysics* 746, 155–172. doi:10.1016/j.tecto.2017.08.029
- Tucker, G.E., Whipple, K.X., 2002. Topographic outcomes predicted by stream erosion models: Sensitivity analysis and intermodel comparison. *J. Geophys. Res.* 107, 2179. doi:10.1029/2001JB000162
- Turner, J.A., Leeder, M.R., Andrews, J.E., Rowe, P.J., Van Calsteren, P., Thomas, L., 2010. Testing rival tectonic uplift models for the Lechaion Gulf in the Gulf of Corinth rift. *J. Geol. Soc. London* 167, 1237–1250. doi:10.1144/0016-76492010-035
- Verrios, S., Zygouri, V., Kokkalas, S., 2004. Morphotectonic Analysis in the Eliki Fault Zone (Gulf of Corinth, Greece). *Bulletin of the Geological Society of Greece* 36, 1706–1715. doi:10.12681/bgsg.16578
- Vita-Finzi, C., King, G.C.P., 1985. The Seismicity, Geomorphology and Structural Evolution of the Corinth Area of Greece. *Philosophical Transactions of the Royal Society of London A: Mathematical, Physical and Engineering Sciences* 314, 379–407. doi:10.1098/rsta.1985.0024
- Wallace, R.E., 1978. Geometry and rates of change of fault-generated range fronts, north-central Nevada. *J. Res. US Geol. Surv* 6, 637–650.
- Walsh, J.J., Watterson, J., 1988. Analysis of the relationship between displacements and dimensions of faults. *J. Struct. Geol.* 10, 239–247. doi:10.1016/0191-8141(88)90057-0
- Watts, A.B., Burov, E.B., 2003. Lithospheric strength and its relationship to the elastic and seismogenic layer thickness. *Earth Planet. Sci. Lett.* 213, 113–131. doi:10.1016/S0012-821X(03)00289-9
- Wernicke, B., 1981. Low-angle normal faults in the Basin and Range Province: nappe tectonics in an extending orogen. *Nature* 291, 645–648.
- Whipple, K.X., 2004. Bedrock rivers and the geomorphology of active orogens. *Annu. Rev. Earth Planet. Sci.* 32, 151–185. doi:10.1146/annurev.earth.32.101802.120356
- Whipple, K.X., Tucker, G.E., 1999. Dynamics of the stream-power river incision model: Implications for height limits of mountain ranges, landscape response timescales, and research needs. *J. Geophys. Res: Solid Earth* 104, 17661–17674.
- Whittaker, A.C., Attal, M., Cowie, P.A., Tucker, G.E., Roberts, G., 2008. Decoding temporal and spatial patterns of fault uplift using transient river long profiles. *Geomorphology* 100, 506–526. doi:10.1016/j.geomorph.2008.01.018
- Whittaker, A.C., Boulton, S.J., 2012. Tectonic and climatic controls on knickpoint retreat rates and landscape response times. *J. Geophys. Res.* 117, F02024. doi:10.1029/2011JF002157
- Whittaker, A.C., Walker, A.S., 2015. Geomorphic constraints on fault throw rates and linkage times: Examples from the Northern Gulf of Evia, Greece. *J. Geophys. Res. Earth Surf.* 120, 2014JF003318. doi:10.1002/2014JF003318
- Willemse, E.J.M., 1997. Segmented normal faults: Correspondence between three-dimensional mechanical models and field data. *J. Geophys. Res.* 102, 675–692. doi:10.1029/96JB01651
- Wobus, C., Whipple, K.X., Kirby, E., Snyder, N., Johnson, J., Spyropolou, K., Crosby, B., Sheehan, D., 2006. Tectonics from topography: Procedures, promise, and pitfalls. *Geological Society of America Special Papers* 398, 55–74. doi:10.1130/2006.2398(04)
- Zelt, B.C., Taylor, B., Sachpazi, M., Hirn, A., 2005. Crustal velocity and Moho structure beneath the Gulf of Corinth, Greece. *Geophys. J. Int.* 162, 257–268. doi:10.1111/j.1365-246X.2005.02640.x
- Ziegler, P.A., 1988. Evolution of the Arctic-North Atlantic and the Western Tethys: A visual presentation of a series of Paleogeographic-Paleotectonic maps. *AAPG Mem.* 43, 164–196.

Supplementary Material

Supplementary Material A. Data integration into a new map

We used a composite Digital Elevation Model (DEM) with 20 m horizontal resolution onland and 50 m offshore to produce the topobathymetry. The onland DEM results from correcting the voids and gaps of a 30m-resolution AW3D30 DSM ([ALOS](#)) with 30m-resolution ASTER GDEM V2 ([ASTER](#)). We merged the result with commercial 20m-resolution SPOT5 DEM covering the southern and east sectors of the rift (inset in Fig. 7), and use a 50 m horizontally-resolved bathymetric data (Sakellariou et al., 2011) in the offshore. We manipulated the resulting composite DEM for several purposes. Firstly, we derive hypsometric contours, which are highlighted with darker colours every 500 m onland and 250 m offshore (Fig. 7). We also use the DEM to produce the stack swath profiles, analyse footwall topography and relief, and perform fluvial geomorphologic analyses (section 4).

Focal mechanisms of earthquakes with $M_w > 5$ since 1965 are shown and, whenever possible, scaled by their magnitude (Taymaz et al., 1991, and the references therein; Rigo et al., 1996; Taylor et al., 2011; Lambotte et al., 2014). The geologic map of Pliocene and younger rocks contains modifications from that of Armijo et al. (1996), which in turn is modified from Dufaure and Zamanis (1979) and Bornovas et al. (1983). We have improved the mapping of the basin in the west rift using the map of Bussolotto et al. (2015). The Hellenic units, regarded as basement for the purposes of this contribution, were also mapped (as in Taylor et al., 2011). To map active faults, we used a selection of onland faults mapped by other contributions (Dart et al., 1994; Armijo et al., 1996; De Martini et al., 2004; McNeill and Collier, 2004; Palyvos et al., 2005; Sakellariou et al., 2007; Maroukian et al., 2008; Roberts et al., 2009; Jolivet et al., 2010; Lambotte et al., 2014; Beckers et al., 2015; Ford et al., 2016; Karymbalis et al., 2016b), and own mapping, using our composite DEM, SPOT images and fieldwork.

We used available reflection seismic lines (McNeill et al., 2005; Sakellariou et al., 2007; Bell et al., 2008, 2009; Taylor et al., 2011; Charalampakis et al., 2014; Lambotte et al., 2014; Beckers et al., 2015; Bussolotto et al., 2015) to create the offshore fault map. Fault selection, remapping and hierarchy are based on fault activity during the Holocene. We identify fault activity in the onshore faults on the basis of the presence of a topographic offset and for the offshore faults, we used seafloor offset or presence of a fault tip close to the seafloor. With the aforementioned means, we produce a 5-level fault hierarchy at the scale of the whole rift, based on relief difference on both sides of the fault and expressed as distinctive stroke thickness in the fault traces (Figs. 7 & 8). We also mapped numerous known faults without topographic expression, i.e. no Holocene activity, that are commonly mapped in studies of the area. We classified them as 4th or 5th level depending on the cross-consistency (both in the presence and position) of their mapping by those contributions. Comparison with the detailed offshore fault mapping based on the reinterpretation of seismic data presented in Nixon et al. (2016) leads to overall satisfactory levels of agreement. The most apparent departures come from our different consideration of what constitutes an “active” fault (Suppl. A).

We also mapped the topsets of the perched Gilbert-type deltas using available stratigraphic maps (Dart et al., 1994; Rohais et al., 2007; Backert et al., 2010; Ford et al., 2016), satellite imagery and Google Earth (Fig. 7). In the case of Akrata and Aigio, where the topsets of the Gilbert deltas are not clearly distinguished from marine terrace levels, we mapped the topsets as the upper marine terrace level. Some known deltaic bodies that have not mappable topsets, or topsets that are difficult to discern from levels of marine terraces were not mapped. Mapping of the alluvial fans and present deltas is based on Karymbalis et al. (2016a) and Ford et al. (2016) (Fig. 7).

We use the marine terraces of De Gelder et al. (2018) mapped from a 2m-resolution DEM derived from Pleiades tri-stereo satellite imagery (De Gelder et al., 2015) using MicMac software (Rosu et al., 2015). This map of marine terraces covers a relevant coastal area in the southeast rift

margin (De Gelder et al, 2018) and marine terraces mapped outside of this area were redrawn to adapt the objects for better fits with the slope and hillshade maps (Armijo et al., 1996; Houghton et al., 2003; De Martini et al., 2004; McNeill and Collier, 2004; Andrews et al., 2007; Maroukian et al., 2008; Roberts et al., 2009).

River drainages of each catchment were manually mapped tracing ridges by means of 5 m equal-height contour lines derived from our 20-m resolution DEM. Windgaps and traces of the paleo-river network were also mapped by these means at some locations, but are not systematically mapped throughout the rift. The river networks were obtained with TopoToolbox 2.0 (Schwanghart and Scherler, 2014), and the result was modified manually for larger accuracy and aesthetic reasons in the flat regions of the internally drained basins of Feneos, Stymfalia and Skotini.

Supplementary Material B. Comparison of offshore fault maps in the Corinth Rift

In a recent effort, Nixon et al. (2016) compiled and reinterpreted a large data set of reflection seismic data into an offshore fault map of the rift. We find three areas with a relevant mismatch when comparing their effort with our map of offshore active faults. Probably the most important mismatch is that in Nixon et al. (2016)'s contribution considers the Derveni fault and Lykoporia fault as the "switching point" between the pure N-S western part and the ENE-WSW eastern part of the rift. Such a change in fault orientation is not questionable, but we are dubitative about its location, at least for Holocene times, given that the Derveni Fault, as Nixon et al. (2016) mapped it, would cut several isopachs in a Holocene depocenter map (pers. comm. Bell, 2016) without appreciable depocenter localization. Our map suggests that this fault dies several kilometres westwards. Similarly, Nixon et al. (2016) mapped significant faults in the northern sector of the gulf, behind the main antithetic faults, in the sectors that they named Central West and Central East. These faults show some displacements in their Nixon et al. (2016)'s Fig. 5, but have no expression

in the seafloor. These faults have no associated depocenter in Holocene times (pers. comm. Bell, 2016), and thus are not mapped in our contribution. Finally, we found discrepancies in the trends of the faults around the islands in the Alkyonides Gulf, striking roughly either E-W (Nixon et al., 2016) or ENE-WSW (this contribution). We keep our original interpretation for faults with Holocene activity, since their orientation is in agreement with the elongation of the islands in the Alkyonides Gulf, the bathymetry, and with a Holocene depocenter map of the gulf (pers. comm. Bell, 2016).

Supplementary Material C to G. Shapefiles and KML files.

We provide shapefiles and KML files of our topobathymetric DEM (Suppl. Mat. C), 5-level hierarchy active fault map (Suppl. Mat. D), marine terraces (Suppl. Mat. E), Gilbert-delta topsets (Suppl. Mat. F), and river streams and their catchments (Suppl. Mat. G).

Supplementary Material References

- Andrews, J.E., Portman, C., Rowe, P.J., Leeder, M.R., Kramers, J.D., 2007. Sub-orbital sea-level change in early MIS 5e: New evidence from the Gulf of Corinth, Greece. *Earth Planet. Sci. Lett.* 259, 457–468.
- Armijo, R., Meyer, B., King, G.C.P., Rigo, A., Papanastassiou, D., 1996. Quaternary evolution of the Corinth Rift and its implications for the Late Cenozoic evolution of the Aegean. *Geophysical Journal International* 126, 11–53.
- Backert, N., Ford, M., Malartre, F., 2010. Architecture and sedimentology of the Kerinitis Gilbert-type fan delta, Corinth Rift, Greece. *Sedimentology* 57, 543–586.
- Beckers, A., Hubert-Ferrari, A., Beck, C., Bodeux, S., Tripsanas, E., Sakellariou, D., De Batist, M., 2015. Active faulting at the western tip of the Gulf of Corinth, Greece, from high-resolution seismic data. *Mar. Geol.* 360, 55–69.
- Bell, R.E., McNeill, L.C., Bull, J.M., Henstock, T.J., 2008. Evolution of the offshore western Gulf of Corinth. *Geol. Soc. Am. Bull.* 120, 156–178.
- Bell, R.E., McNeill, L.C., Bull, J.M., Henstock, T.J., Collier, R.E.L., Leederz, M.R., 2009. Fault architecture, basin structure and evolution of the Gulf of Corinth Rift, central Greece. *Basin Res.* 21, 824–855.
- Bornovas, J., Rondogianni-Tsiambaou, T., kai Metalleutikōn Ereunōn, A.I.G., 1983. [Geological map of Greece 1: 500000]; *Geōlogikos chartēs tēs Ellados*. IGME.
- Bussolotto, M., Benedicto, A., Moen-Maurel, L., Invernizzi, C., 2015. Fault deformation mechanisms and fault

- rocks in micritic limestones: Examples from Corinth rift normal faults. *J. Struct. Geol.* 77, 191–212.
- Charalampakis, M., Lykousis, V., Sakellariou, D., Papatheodorou, G., Ferentinos, G., 2014. The tectono-sedimentary evolution of the Lechaion Gulf, the south eastern branch of the Corinth graben, Greece. *Mar. Geol.* 351, 58–75.
- Dart, C.J., Collier, R.E.L., Gawthorpe, R.L., Keller, J.V.A., Nichols, G., 1994. Sequence stratigraphy of (?)Pliocene-Quaternary synrift, Gilbert-type fan deltas, northern Peloponnesos, Greece. *Mar. Pet. Geol.* 11, 545–560.
- De Gelder, G., Fernández-Blanco, D., Lacassin, R., Armijo, R., Delorme, A., Jara-Muñoz, J., Melnick, D., 2015. Corinth terraces re-visited: Improved paleoshoreline determination using Pleiades-DEMs. *Geotectonic Research* 97, 12–14.
- De Martini, P.M., Pantosti, D., Palyvos, N., Lemeille, F., McNeill, L., Collier, R., 2004. Slip rates of the Aigion and Eliki Faults from uplifted marine terraces, Corinth Gulf, Greece. *C. R. Geosci.* 336, 325–334.
- Dufaure, J.-J., Zamanis, A., 1979. Un vieux problème géomorphologique: les niveaux bordiers au sud du Golfe de Corinthe (An old geomorphological problem: the levels developed on the southern border of the gulf of Corinth). *Bulletin de l'Association de géographes français* 56, 341–350.
- Ford, M., Hemelsdaël, R., Mancini, M., Palyvos, N., 2016. Rift migration and lateral propagation: evolution of normal faults and sediment-routing systems of the western Corinth rift (Greece). Geological Society, London, Special Publications 439. doi:10.1144/SP439.15
- Houghton, S.L., Roberts, G.P., Papanikolaou, I.D., McArthur, J.M., Gilmour, M.A., 2003. New 234U-230Th coral dates from the western Gulf of Corinth: Implications for extensional tectonics. *Geophys. Res. Lett.* 30, 2013.
- Jolivet, L., Labrousse, L., Agard, P., Lacombe, O., Bailly, V., Lecomte, E., Mouthereau, F., Mehl, C., 2010. Rifting and shallow-dipping detachments, clues from the Corinth Rift and the Aegean. *Tectonophysics* 483, 287–304.
- Karymbalis, E., Ferentinou, M., Giles, P.T., 2016a. Use of morphometric variables and self-organizing maps to identify clusters of alluvial fans and catchments in the north Peloponnese, Greece. Geological Society, London, Special Publications 440. doi:10.1144/SP440.7
- Karymbalis, E., Papanastassiou, D., Gaki-Papanastassiou, K., Ferentinou, M., Chalkias, C., 2016b. Late Quaternary rates of stream incision in Northeast Peloponnese, Greece. *Front. Earth Sci.* 10, 455–478.
- Lambotte, S., Lyon-Caen, H., Bernard, P., Deschamps, A., Patau, G., Nercessian, A., Pacchiani, F., Bourouis, S., Drilleau, M., Adamova, P., 2014. Reassessment of the rifting process in the Western Corinth Rift from relocated seismicity. *Geophys. J. Int.* 197, 1822–1844.
- Maroukian, H., Gaki-Papanastassiou, K., Karymbalis, E., Vouvalidis, K., Pavlopoulos, K., Papanastassiou, D., Albanakis, K., 2008. Morphotectonic control on drainage network evolution in the Perachora Peninsula, Greece. *Geomorphology* 102, 81–92.
- McNeill, L.C., Collier, R.E.L., 2004. Uplift and slip rates of the eastern Eliki fault segment, Gulf of Corinth, Greece, inferred from Holocene and Pleistocene terraces. *J. Geol. Soc. London* 161, 81–92.
- McNeill, L.C., Cotterill, C.J., Henstock, T.J., Bull, J.M., Stefatos, A., Collier, R.E.L., Papatheoderou, G., Ferentinos, G., Hicks, S.E., 2005. Active faulting within the offshore western Gulf of Corinth, Greece: Implications for models of continental rift deformation. *Geology* 33, 241–244.
- Nixon, C.W., McNeill, L.C., Bull, J.M., Bell, R.E., Gawthorpe, R.L., Henstock, T.J., Christodoulou, D., Ford, M., Taylor, B., Sakellariou, D., Ferentinos, G., Papatheodorou, G., Leeder, M.R., Collier, R.E.L.I., Goodliffe, A.M., Sachpazi, M., Kranis, H., 2016. Rapid spatiotemporal variations in rift structure during development of the Corinth Rift, central Greece. *Tectonics* 35, 2015TC004026.

- Palyvos, N., Pantosti, D., De Martini, P.M., Lemeille, F., Sorel, D., Pavlopoulos, K., 2005. The Aigion–Neos Erineos coastal normal fault system (western Corinth Gulf Rift, Greece): Geomorphological signature, recent earthquake history, and evolution. *J. Geophys. Res.* 110, B09302.
- Rigo, A., Lyon-Caen, H., Armijo, R., Deschamps, A., Hatzfeld, D., Makropoulos, K., Papadimitriou, P., Kassaras, I., 1996. A microseismic study in the western part of the Gulf of Corinth (Greece): Implications for large-scale normal faulting mechanisms. *Geophys. J. Int.* 126, 663–688.
- Roberts, G.P., Houghton, S.L., Underwood, C., Papanikolaou, I., Cowie, P.A., van Calsteren, P., Wigley, T., Cooper, F.J., McArthur, J.M., 2009. Localization of Quaternary slip rates in an active rift in 10 5 years: An example from central Greece constrained by 234 U- 230 Th coral dates from uplifted paleoshorelines. *J. Geophys. Res.* 114, 393.
- Rohais, S., Eschard, R., Ford, M., Guillocheau, F., Moretti, I., 2007. Stratigraphic architecture of the Plio-Pleistocene infill of the Corinth Rift: Implications for its structural evolution. *Tectonophysics* 440, 5–28.
- Rosu, A.-M., Pierrot-Deseilligny, M., Delorme, A., Binet, R., Klinger, Y., 2015. Measurement of ground displacement from optical satellite image correlation using the free open-source software MicMac. *ISPRS J. Photogramm. Remote Sens.* 100, 48–59.
- Sakellariou, D., Lykousis, V., Alexandri, S., Kaberi, H., Rousakis, G., Nomikou, P., Georgiou, P., Ballas, D., 2007. Faulting, seismic-stratigraphic architecture and Late Quaternary evolution of the Gulf of Alkyonides Basin–East Gulf of Corinth, Central Greece. *Basin Res.* 19, 273–295.
- Sakellariou, D., Lykousis, V., Rousakis, G., 2011. Holocene seafloor faulting in the Gulf of Corinth: The potential for underwater paleoseismology. 2nd INQUA-IGCP-567 International Workshop on Active Tectonics, Earthquake Geology, Archaeology and Engineering. Corinth, Greece.
- Schwanghart, W., Scherler, D., 2014. TopoToolbox 2 – MATLAB-based software for topographic analysis and modeling in Earth surface sciences. *Earth Surf. Dynam.* 2, 1–7.
- Taylor, B., Weiss, J.R., Goodliffe, A.M., Sachpazi, M., Laigle, M., Hirn, A., 2011. The structures, stratigraphy and evolution of the Gulf of Corinth rift, Greece: Structures, stratigraphy and evolution of GoC. *Geophys. J. Int.* 185, 1189–1219.
- Taymaz, T., Jackson, J., McKenzie, D., 1991. Active tectonics of the north and central Aegean Sea. *Geophysical Journal International* 106, 433–490.